Empirical Models for CubeSat Stability Indices based on the Gravity-Gradient Stabilization

YASMIN DA COSTA FERREIRA AVELINO

DISSERTAÇÃO DE MESTRADO
EM ENGENHARIA ELÉTRICA

DEPARTAMENTO DE ENGENHARIA ELÉTRICA

FACULDADE DE TECNOLOGIA

UNIVERSIDADE DE BRASÍLIA

Universidade de Brasília
Faculdade de Tecnologia
Departamento de Engenharia Elétrica

Empirical Models for CubeSat Stability Indices based on the Gravity-Gradient Stabilization

Yasmin da Costa Ferreira Avelino

DISSERTAÇÃO DE MESTRADO SUBMETIDA AO PROGRAMA DE PÓS-GRADUAÇÃO EM ENGENHARIA ELÉTRICA DA UNIVERSIDADE DE BRASÍLIA COMO PARTE DOS REQUISITOS NECESSÁRIOS PARA A OBTENÇÃO DO GRAU DE MESTRE.

APROVADA POR:

Renato Alves Borges, Doutor (Universidade de Brasília)

(Orientador)

William Reis Silva, Doutor (Universidade de Brasília)

(Co-orientador)

Simone Battistini, Doutor (MBDA Italy)

(Examinador Externo)

Geovany Araújo Borges, Doutor (Universidade de Brasília)

(Examinador Interno)

Brasília/DF, dezembro de 2024.

FICHA CATALOGRÁFICA

AVELINO, YASMIN DA COSTA FERREIRA

Empirical Models for CubeSat Stability Indices based on the Gravity-Gradient Stabilization. [Brasília/DF] 2024.

xxx, nnnp., 210 x 297 mm (ENE/FT/UnB, Mestre, Dissertação de Mestrado, 2024).

Universidade de Brasília, Faculdade de Tecnologia, Departamento de Engenharia Elétrica.

Departamento de Engenharia Elétrica

1. CubeSat	2. Gravity-Gradient Stabilization
3. CubeSat Design Specifications	4. Rotational Kinetic Energy
5. Empirical Models	6. Stability Indices
7. ADCS	8. Semi-Passive Attitude Control
9. Design Optimization	10. Python
I. ENE/FT/UnB	II. Título (série)

REFERÊNCIA BIBLIOGRÁFICA

AVELINO, Y. C. F. (2024). Empirical Models for CubeSat Stability Indices based on the Gravity-Gradient Stabilization. Dissertação de Mestrado, Publicação PPGEE 825/25, Departamento de Engenharia Elétrica, Universidade de Brasília, Brasília, DF, Brasil.

CESSÃO DE DIREITOS

AUTOR: Yasmin da Costa Ferreira Avelino

TÍTULO: Empirical Models for CubeSat Stability Indices based on the Gravity-Gradient Stabilization.

GRAU: Mestre ANO: 2024

Yasmin da Costa Ferreira Avelino

Universidade de Brasília (UnB)

Campus Darcy Ribeiro

Faculdade de Tecnologia - FT

Departamento de Engenharia Elétrica(ENE)

Brasília - DF CEP 70919-970

To the most important people for me in this entire world: Jesus, my Lord and Savior, the loved of my soul; Tiago, my beloved husband and love of my life; Letícia, my dearest sister and best friend; Edilene, my precious mother and hero; Ubiratan, my loving father and intercessor.

AGRADECIMENTOS

This thesis, though bearing my name, is the product of countless acts of support, encouragement, and love from many extraordinary individuals. This section is my humble attempt to express my deepest gratitude to all who have helped me reach this milestone.

To God, who rescued me from the darkest places of my soul, showing me infinite mercy and grace over and over again. You have held my hand, loved me beyond human comprehension, and in manners no one could ever do. You are my hope, my joy, and my life. No words could ever fully express my gratitude for your sublime redemption and compelling love. No words can describe the holiness and kindness of your being.

To Tiago, my beloved husband, you are much more that I could ask for. Your love teaches me kindness, generosity, and selflessness every day. You stood by me when I felt unworthy of love, and I will never forget that. Thank you for believing in me even when I doubted myself, what happens frequently, for refusing to let me give up when challenges got hard, and for sharing my dreams and supporting each one of them. You are my love and my home, and I could never wish for a better partner for this journey than you.

To Letícia, my sister, you are, and always will be, the greatest gift our parents ever gave me. I have never, not even for a moment, regretted wishing for and waiting for you. You are my best friend, my confidant. You make life lighter, when things get heavy, and you fill it with joy and laughter. Thank you for standing by my side every step of the way—celebrating my wins, lifting me up during setbacks, and sharing my tears. I am beyond grateful to share this journey with you.

To Edilene, my mom, you are my hero. Your life is a testimony that, even in moments of loneliness and helplessness, God never forsaken us. Thank you for teaching me countless lessons, but above all of them, thank you for your love, that for many many times meant sacrifice, that will always be your greatest lesson. I love you more than words can express.

To Ubiratan, my dad, thank you for leading me to Jesus. Your kindness and love have left

an indelible mark on my heart. In many ways, you've shown me that love can endure distance, trusting God to care for our loved ones. Thank you for your gentle love and constant prayers, that are both priceless and powerful. I love you deeply.

To my mentors, Renato and William, this work would not be what it is without your guidance and support. I am immensely grateful for far more than mentorship—you've given me encouragement, opened doors, and shown genuine care. You are role models and sources of inspiration, and I cannot thank you enough for believing in me, recognizing my potential, and helping me refine it.

To my family and friends, life is infinitely better when shared with you. Thank you for cheering me on, loving me, laughing with me, crying with me, and walking alongside me on this journey. Your support has helped me grow and brought Christ's love and cross into my life in countless ways. I love you all.

RESUMO

MODELOS EMPÍRICOS DE ÍNDICES DE ESTABILIDADE PARA CUBESATS BASEADOS NA ESTABILIZAÇÃO POR GRADIENTE-GRAVITACIONAL

Otimizar tamanho, peso, consumo de energia e desempenho dos subsistemas de um CubeSat é essencial, quando consideramos as restrições inerentes às missões do padrão CubeSat. As Especificações de Projeto de CubeSats (CubeSat Design Specifications - CDS) permitem projetos mecânicos com valores de inércia distribuídos nas cinco regiões de estabilidade no Mapa de Estabilidade por Gradiente Gravitacional (Gravity-Gradient Stability Map - GGSM): Lagrange, Debra-Delp, Pitch, Roll-Yaw e Instável. Este trabalho investiga a aplicação da Estabilização por Gradiente Gravitacional (Gravity-Gradient Stabilization - GGS), que utiliza o torque gravitacional para estabilização passiva, analisando padrões de energia cinética rotacional e introduzindo modelos empíricos para índices de estabilidade baseados no GGSM, nos momentos principais de inércia e nas raízes da equação característica para padrões CubeSat. Simulações numéricas em Python e ajuste de curvas polinomiais validam a eficácia desses modelos, fornecendo uma estrutura robusta para avaliar projetos mecânicos e identificar configurações que melhoram a estabilidade de atitude de CubeSats. Uma aplicação desses índices baseados em modelos empíricos compara a GGS com os sistemas ativos de Determinação e Controle de Atitude (Attitude Determination and Control Systems - ADCS) mais comumente usados — especificamente magnetorquers e rodas de reação — no padrão CubeSat. A análise foca no desempenho de controle, implicações na geração de potência de energia e methodologia para a otimização do projeto, sendo esta última útil para modelagem estrutural. Os resultados indicam que configurações com menor energia cinética rotacional melhoram a resposta do controle e a eficiência geral, demonstrando as potenciais vantagens de integrar controle ativo de atitude e GGS utilizando os índices propostos baseados em modelos empíricos. Cenários de estudo de caso foram simulados considerando uma órbita circular de 500 km de altitude, utilizando o método de dois corpos. O impacto da GGS na geração de potência dos CubeSats

também foi considerado nas simulações numéricas. Os resultados comparam o desempenho das regiões do GGSM em termos de geração de potência para diferentes tamanhos de CubeSats. Os resultados demonstraram que a GGS proporciona geração uniforme de energia para todas as regiões do GGSM. As simulações numéricas foram realizadas utilizando Python e também o software Systems Tool Kit (STK).

Palavras-chave: CubeSat, Estabilização por Gradiente Gravitacional (GGS), Estabilização Passiva de Atitude, Especificações de Projeto de CubeSats (CDS), Energia Cinética Rotacional, Modelos empíricos, Índices de Estabilidade, Órbita Baixa Terrestre (LEO), Sistema de Determinação e Controle de Atitude (ADCS), Magnetorquers, Rodas de Reação, Desempenho de Controle, Otimização de Projeto, Sistema de Energia Elétrica (EPS), Python, Systems Tool Kit (STK).

ABSTRACT

Optimizing CubeSat subsystems for size, weight, power consumption, and performance is essential given the inherent constraints of CubeSat missions. The CubeSat Design Specifications (CDS) allow for mechanical designs with inertia values across five stability regions on the Gravity-Gradient Stability Map (GGSM): Lagrange, Debra-Delp, Pitch, Roll-Yaw, and Unsteady. This work investigates the application of Gravity-Gradient Stabilization (GGS), which utilizes external gravitational torque for passive stabilization, by analyzing rotational kinetic energy patterns and introducing empirical models for stability indices based on the GGSM, principal moments of inertia, and characteristic equation roots for CubeSat standards. Python-based numerical simulations and polynomial curve fitting validate the effectiveness of these models, providing a robust framework for evaluating mechanical designs and identifying configurations that enhance CubeSat attitude stability. One application of these empirical model-based indices compares GGS with commonly used active Attitude Determination and Control Systems (ADCS) - specifically magnetorquers and reaction wheels - within the CubeSat standard. The analysis focuses on control performance, power generation implications, and design optimization methodology, the latter useful for structural modeling. The results indicate that configurations with lower rotational kinetic energy improve control response and overall efficiency, demonstrating the potential advantages of integrating active attitude control and GGS using the proposed empirical model-based indices. Case study scenarios were simulated considering a 500 km altitude circular orbit and were performed using the two-body method. The impact of GGS on the power generation of CubeSats was also considered in the numerical simulations. The results compare the performance of the GGSM regions in terms of power generation for different CubeSat sizes. The results demonstrated that GGS provides uniform power generation for all GGSM regions. Numerical simulations were performed using Python and also the Systems Tool Kit (STK) software.

Keywords: CubeSat, Gravity-Gradient Stabilization (GGS), Passive Attitude Stabilization,

CubeSat Design Specifications (CDS), Rotational Kinetic Energy, Empirical Models, Stability Indices, Low Earth Orbit (LEO), Attitude Determination and Control System (ADCS), Magnetorquers, Reaction Wheels, Control Performance, Design Optimization, Electrical Power Subsystem (EPS), Python, Systems Tool Kit (STK).

CONTENTS

LIST OF FIGURES

LIST OF TABLES

LIST OF SYMBOLS

ϕ	Roll angle
θ	Pitch angle
ψ	Yaw angle
ϕ	Roll angle
$\mathbf{I}_n$	Idendity matrix n
$_I$	Inertial Frame
$_O$	LVLH Frame
$_B$	Body Frame
$\mathbf{A}_{IO}$	Rotation matrix from Inertial frame to LVLH frame
$\mathbf{A}_{321}(\phi, \theta, \psi)$	Attitude matrix of the 3-2-1 sequence
$\mathbf{J}_B^c$	Moment of Inertia Tensor on the principal axis frame
$\boldsymbol{\omega}_B^{BI}$	Rigid body angular velocity on the body frame
$\mathbf{L}_B^{\text{gg}}$	GG torque on the body frame
$\mathbf{L}_B^{\text{mag}}$	Magnetic Torque on the body frame
$\mathbf{m}$	Magnetic moment on the body frame
$\mathbf{B}$	Geomagnetic Field on the body frame
$\mathbf{L}_B^w$	Reaction Wheel's Torque on the body frame
$\mathbf{H}_B^w$	Reaction Wheel's Angular Momentum on the body frame
h	Orbit's Angular Momentum

μ	Gravitational parameter
h^2/μ	Semi-latus rectum
e	Orbit's Eccentricity
f	True anomaly
a	Orbit's major semi-axis
η	Orbit's mean motion

GLOSSARY

ADCS	Attitude Determination and Control System
ARKE	Average Rotational Kinetic Energy
CDS	CubeSat Design Specifications
CG	Center of Gravity
CM	Center of Mass
DD	Debra-Delp
EPS	Electrical Power System
GCI	Geocentric Inertial Frame
GG	Gravity-Gradient
GGS	Gravity-Gradient Stabilization
GGSM	Gravity-Gradient Stability Map
HARKE	Higher Average Rotational Kinetic Energy
ICRF	International Celestial Reference System
LARKE	Lower Average Rotational Kinetic Energy
LHP	Left Half-Plane
LSPF	Least Squares Polynomial Fit
LVLH	Local-Vertical/Local-Horizontal
MOI	Moment of Inertia
MSE	Mean Square Error
RPY	Roll-Pitch-Yaw

RHP	Right Half-Plane
RKE	Rotational Kinetic Energy
SMM	Stability Map Margin
SNCR	Sum of the Norm of the Characteristic Roots
STK	System Tool Kit
TEA	Torque-Equilibrium Attitude
Tr(J)	Trace of the Moments of Inertia Tensor

CHAPTER 1

INTRODUCTION

Most spacecrafts missions have specific pointing requirements, some are Earth pointed, others require inertial pointing, and others Sun or specific celestial objects pointing (MARKLEY; CRASSIDIS, 2014; HUGHES, 2004). Sometimes, different parts of a spacecraft have distinct orientation requirements; for example, a communications antenna may need to point toward Earth, while solar panels must be perpendicular to the Sun. Achieving such mission objectives highlights the importance of attitude stabilization and control systems, making attitude dynamics an essential aspect of the mission design (HUGHES, 2004).

The topic of this work is spacecraft attitude dynamics: an applied science that seeks to understand and predict the evolution of a spacecraft's orientation (HUGHES, 2004). As a critical component of spacecraft engineering, attitude dynamics combines theoretical principles and practical applications to ensure mission success.

1.1 BACKGROUND

In many modern applications, the permissible attitude errors are so small that only an active control system can meet mission requirements. Typically, an Attitude Determination and Control System (ADCS) includes sensors to measure the orientation, attitude rate, or both (WERTZ, 1973) and actuators that generate internal or external torques to control the spacecraft's attitude.

On the other hand, if the high accuracy of the attitude pointing is not a mission requirement, the mission and mechanical designers may explore stabilization techniques that rely on the intrinsic features of the vehicle dynamics. These techniques either include appropriate dynamical elements in the design, such as dampers or leverage natural environmental forces to achieve the desired stabilization torque, passive stabilization. Considering this topic, some

external torques that collaborate to the spacecraft attitude stabilization are atmospheric drag and gravity-gradient torque.

Extensive research has been conducted on the stability analysis of spacecraft with various shapes and masses subjected to external disturbances (RIANO-RIOS *et al.*, 2021; MEIROVITCH; WALLACE, 1966; FRIK, 1970; FISCHELL; MOBLEY, 1964; LIKINS; ROBERSON, 1966; MIYAMOTO *et al.*, 2023; BECK, 1997; DESOUKY; ABDELKHALIK, 2022; MASLOVA; PIROZHENKO, 2010; MODI; SHRIVASTAVA, 1971). Gravity-Gradient Stabilization (GGS), a passive technique leveraging Earth's gravitational forces, was first implemented in the 1963-22A satellite (FISCHELL; MOBLEY, 1964) and later applied in numerous missions, from ensuring navigation accuracy in the Navy Navigation Satellite System (NAVSAT or NNSS) (DANCHIK, 1998) to stabilizing the International Space Station and other torque-equilibrium attitude (TEA) spacecraft (VADALI; OH, 1992). Early meteorological satellites, such as the GOES series (FINLEY, 2025) relied on GGS for consistent nadir-pointing orientations.

In addition to large-scale missions, GGS has been adapted for CubeSats, showcasing its practicality for small, resource-constrained platforms. For example, the Japanese STARS (Space Tethered Autonomous Robotic Satellite) mission employed a tether tas a GGS mechanism (NOHMI, 2007), while UniCubeSat from the University of Rome used two deployable booms to test gravity-gradient stabilization (CAPPELLETTI *et al.*, 2011). Similarly, Estonia's ESTCube-1 mission deployed a tether to passively stabilize its attitude and test electric solar wind sail technology(LäTT *et al.*, 2014). These CubeSat applications demonstrate how GGS, through simple deployable mechanisms, offers a cost-efficient, power-saving solution for attitude control, aligning with the compact design and operational constraints of small satellites.

While significant research has focused on stabilization using aerodynamic forces or TEA spacecraft (MIYAMOTO *et al.*, 2023), GGS remains a proven and versatile method for both large-scale and CubeSat missions. However, mostly with the usage of deployable devices, which sometimes may challenge the satellite design.

It is always possible, and sometimes necessary, to supplement passive stabilization with active control using thrusters, magnetorquers, or reaction wheels. Active control effort can be minimized by starting with inherent stable characteristics (MARKLEY; CRASSIDIS, 2014).

Is no longer news that the CubeSat standard has revolutionized the space sector, becom-

ing the main access to space for firstly educational institutions and now also for commercial, government, and private industries (YOST; WESTON, 2023). The great success of the CubeSat is due to two essential features: size and containment (CAPPELLETTI *et al.*, 2020). The compact size of CubeSats made their launches more affordable, while their containment alleviated concerns from launch providers about potential damage to the launch vehicle or the primary satellite (CAPPELLETTI *et al.*, 2020).

Given the numerous constraints inherent in CubeSat missions, optimizing the size, weight, power consumption, and performance of the subsystems is critical (YOST; WESTON, 2023; CAPPELLETTI *et al.*, 2020). Within the context of optimization for ADCS, there are some potential benefits of leveraging GGS features to enhance aspects of the attitude motion, or even use those features for semi-passive attitude control of CubeSats.

The CubeSat Design Specifications (CDS) (JOHNSTONE, 2022) define tolerance ranges for the Center of Gravity (CG) of the satellite, a crucial parameter for determining the inertia tensor and the Gravity-Gradient (GG) torque. Variations in CG position can lead to multiple regions within the GG stability map - Lagrange, Debra-Delp, Pitch, Roll-Yaw, and Unstable. These variations render GGS a viable, and sometimes advantageous, passive stabilization strategy for CubeSat missions.

Considering active ADCS methods, the two most used for CubeSat missions are: magnetorquers, which utilize the geomagnetic field, and reaction wheels, which rely on the conservation of angular momentum (CAPPELLETTI *et al.*, 2020). Magnetorquers are attractive for CubeSat missions due to their relatively lightweight, low power consumption, and cost-effectiveness(WIśNIEWSKI; BLANKE, 1999). Meanwhile, when the mission requires high attitude accuracy the reaction wheels are widely used (CAPPELLETTI *et al.*, 2020).

Due to its Earth-pointing capability, GGS is frequently used alongside other attitude control methods (MIYAMOTO *et al.*, 2023; ARDUINI; BAIOCCO, 1997; WIśNIEWSKI; BLANKE, 1999). Under this consideration, we aim to investigate the relationship between the natural characteristics of GG torque and the performance of the control system.

Furthermore, the attitude of a spacecraft relates to other subsystems as well. The Electrical Power Subsystem (EPS) is a fundamental and one of the most challenging subsystems in a CubeSat mission (YOST; WESTON, 2023) because of its limited size and weight. Currently,

solar panels are the main power generation source of satellite missions, especially for CubeSats (YOST; WESTON, 2023).

Solar cells, while widely used, come with several challenges, including reduced efficiency in deep-space environments, lack of power generation during eclipses, degradation over the mission lifespan, and the requirement for a large surface area, which increases the mass and cost of the project (YOST; WESTON, 2023; CAPPELLETTI *et al.*, 2020; GREY *et al.*, 2020; AMJADIFARD *et al.*, 2019; SáNCHEZ-SANJUáN *et al.*, 2016). Additionally, a critical factor affecting the use of solar panels for satellite power generation is the solar incidence angle, which is influenced by the satellite's orbital parameters and attitude (AVELINO *et al.*, 2024). In some missions, deployable solar panel mechanisms are employed to optimize the solar incidence angle and maximize the limited surface area. However, these mechanisms add complexity and risk to the mission (YOST; WESTON, 2023) and may impact the design or performance of other subsystems, including the structure, attitude control, or even the overall mission lifespan, due to the increase in atmospheric drag.

The relationship between the ADCS and the EPS is particularly intricate, with limited research available on this interaction (FISCHELL; MOBLEY, 1964; GREY *et al.*, 2020; AMJADIFARD *et al.*, 2019; SáNCHEZ-SANJUáN *et al.*, 2016; ANIGSTEIN; SáNCHEZ-PEñA, 1998; BOWDEN, 1981; ZAHRAN *et al.*, 2006; AVELINO *et al.*, 2024). One notable advantage of Gravity-Gradient Stabilization (GGS) is its ability to improve solar power system performance by facilitating optimal solar panel alignment for efficient energy capture (FISCHELL; MOBLEY, 1964).

1.2 MOTIVATION AND PROBLEM STATEMENT

The main motivation for this study stems from the specifications of CubeSat projects, particularly the tolerances for the CM location and their potential kinematic impact on the spacecraft. The initial question was whether variations in the CM, within acceptable design tolerances, could significantly affect the spacecraft's kinematic stability concerning the GGS. This intuition, though not explicitly documented in the existing literature, served as the foundation for further research.

Two critical questions emerged during this study:

1. **Is this issue significant for an operational satellite?** This question was addressed theoretically, analyzing the potential impacts of kinematic instability on mission objectives such as power generation and precise pointing. For example, an unstable kinematic condition might demand higher control effort, potentially affecting energy consumption or system performance.

2. **Can we develop a practical tool to assist designers in evaluating stability?** The study aimed to identify a recognizable signature within the gravitational gradient stability map that could serve as a quick reference for designers to assess the viability of a given configuration still on the initial phases of the mechanical design. This led to the proposal of the Dummy Mass Grid methodology, which evaluates the effect of swapping subsystems or adding a dummy mass to achieve optimal CM distribution and enhance stability.

By employing numerical simulations, key metrics such as the spacecraft's average kinetic energy were analyzed. These metrics, directly related to kinematic stability, provided insight into how CM variations indirectly influenced performance. When initial attempts to identify clear stability patterns proved challenging, a polynomial approximation approach was introduced to refine the analysis. This method replaced scattered data points with a continuous curve, making the results more accessible for application in the design of early-stage mechanical and control systems.

1.3 OBJECTIVES AND CONTRIBUTIONS

This research focused on investigating the attitude dynamics of a rigid body, particularly GGS within the CubeSat standard. The primary objective is to develop empirical stability indices models based on the average kinetic rotational energy patterns to aid designers in identifying optimal configurations during the CubeSat design process. A key aspiration was to guide designs toward achieving three-axis stable Lagrange configurations while improving attitude and control performance based on GGS principles. The key contributions of this work include:

- **Empirical Models of Stability Indices:** Three stability indices — Stability Map

Margin (SMM), the trace of the MOI tensor in the principal axis frame (Tr(J)), and the sum of the norm of the characteristic roots (SNCR) — are proposed and evaluated. These indices provide a robust framework for analyzing Average Rotational Kinetic Energy (ARKE) patterns across the Gravity-Gradient Stability Map (GGSM). The models are evaluated with the Least Squares Polynomial Fit (LSPF) and the performance metric is the Mean Square Error (MSE).

- **Dummy Mass Grid Methodology:** A novel approach is developed to enhance CubeSat design, in its early design phases, by strategically adding a dummy mass or shifting subsystems, in order to transform unstable or suboptimal configurations into more stable designs.

- **Simulation Framework:** the implementation of Python-based, object-oriented simulation framework to analyze CubeSat attitude dynamics and validate the proposed models. This framework supported simulations for ARKE patterns, dummy mass grid enhancements, regulation control, and attitude motion effects on power generation.

Those contributions extended to practical applications and insights:

- **Insights on semi-passive ADCS:** The integration of GGS with attitude actuators, such as reaction wheels and magnetorquers, exploring semi-passive attitude control and the effects of different GGS features. The transient periods, control torque reductions, and actuator performance metrics are evaluated for Lower Average Rotational Kinetic Energy (LARKE) and Higher Average Rotational Kinetic Energy (HARKE) configurations derived from the ARKE patterns simulation, as well for Initial and Improved designs derived from the dummy mass grid simulation.

- **Power Generation Analysis:** The study investigated the relationship between GGS-induced attitude motion and CubeSat power generation, using the simulation framework and the System Tool Kit (STK), evaluating the power generation and solar incidence across GGSM regions with the CubeSat models available on STK database.

1.4 DOCUMENT OUTLINE

This dissertation is organized into six chapters. The introduction lays out the background, motivation, objectives, and contributions of the research, emphasizing the advantages and versatility of GGS and its implications for CubeSat attitude dynamics.

The second chapter provides the fundamentals of attitude dynamics, discussing attitude representations, kinematics, dynamics, and the reference frames used throughout the study. It also provides fundamental equations, including Euler's rotational equation, which governs the attitude dynamics of a rigid body.

The third chapter focuses on Gravity-Gradient Stabilization, detailing the principles behind this stabilization method and presenting the governing equations for attitude motion. It also introduces the Gravity-Gradient Stability Map (GGSM), derived through stability analysis, and discusses the conditions for stability in both conservative and gyric systems.

The methodology is described in the fourth chapter, which introduces the rigid body modeling of CubeSats based on the CDS and outlines the proposed empirical models for stability indices. It also explains the Dummy Mass Grid methodology, defines the regulation control law with the performance metrics used for control evaluation, and simulation framework.

The fifth chapter presents and analyzes the results, including ARKE patterns, dummy mass enhancements, semi-passive ADCS performance, and the relationship between GGS-induced attitude motion and power generation. Lastly, the work concludes by summarizing the key findings and future works proposals.

CHAPTER 2

SPACECRAFT ATTITUDE

The attitude of a spacecraft refers to its orientation in space, while its motion in orbit is characterized by position, velocity, orientation, and angular motion (WERTZ, 1973). Position and velocity describe the translational motion of the spacecraft's Center of Mass (CM), governed by orbital dynamics. In contrast, orientation and angular motion relate to the spacecraft's rotational motion about its CM (WERTZ, 1973), known as attitude dynamics, the primary focus of this work.

Analyzing attitude dynamics involves three key processes: determination, prediction, and control (HUGHES, 2004; WERTZ, 1973). Attitude determination calculates the spacecraft's orientation relative to a reference frame, which may be inertial or non-inertial. Attitude prediction involves foreseeing the spacecraft's orientation by extrapolating its attitude using dynamic models, where environmental interactions are critical to the accuracy of these predictions. Finally, attitude control refers to orienting the spacecraft in a specific way,

Though a specialized area within the broader field of dynamics, attitude dynamics intersects with many other spacecraft disciplines. Key related fields that will be discussed to varying extents in this work are illustrated in Fig. 2.1.

Orbits

The orbital (translational) and attitude (rotational) dynamics are inherently coupled, even from a classical perspective, when considering only the gravitational field. Since gravity is a conservative force field, the system's energy, momentum, and angular momentum are conserved (HUGHES, 2004). Other than this, the spacecraft's orbit, the amount of solar wind and radiation, magnetic field influence, and aerodynamic drag, among other environmental features that directly influence the body's attitude (HUGHES, 2004; WERTZ, 1973; MARKLEY; CRASSIDIS,

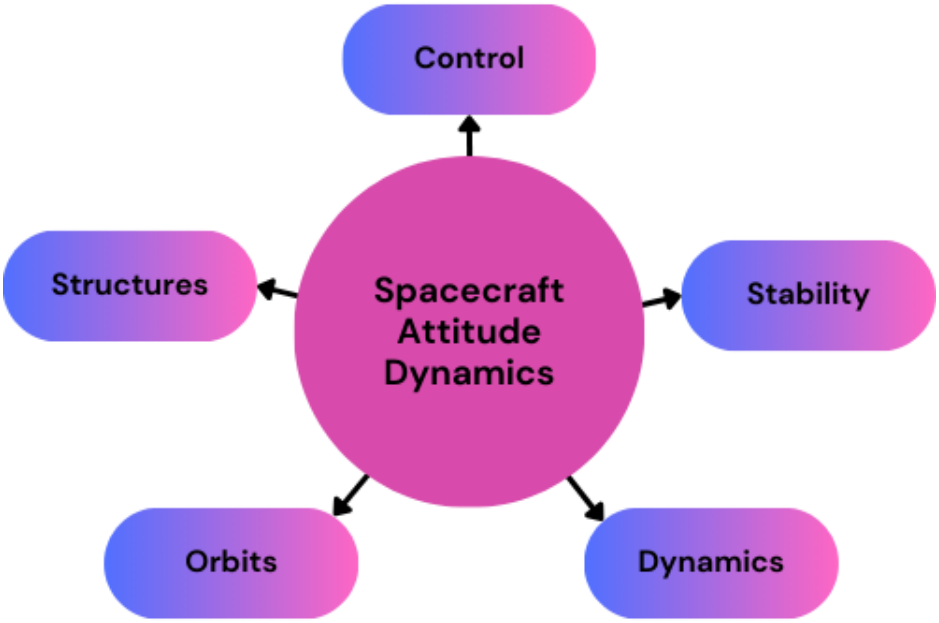

Figure 2.1. Disciplines related to the attitude dynamics of a spacecraft. Source: Adapted from (HUGHES, 2004)

2014). Some of these factors will be included in the analysis of this work.

Structures

Even though real bodies are not perfectly rigid, much of the spacecraft attitude dynamics relies on rigid body dynamics. This approach can explain many aspects of spacecraft orientation behavior (MARKLEY; CRASSIDIS, 2014; HUGHES, 2004). The advantage of using a rigid body model, which will be better developed further in this chapter, is that it simplifies the analysis by contributing at most six degrees of freedom, of which three are rotational (HUGHES, 2004).

Dynamics

There are numerous dynamical formulations available for deriving equations of motion, each with its own benefits and limitations. In this work, the derivation of the fundamental dynamic models will focus on using vector mechanics and the mathematical abstractions of mass points and rigid bodies. Given the nonlinear nature of spacecraft motion, the dynamics formulations will also include linearization processes and simplified assumptions.

Stability

Exact differential equations for spacecraft attitude motion are nonlinear, as mentioned previously, and in many cases, the closed form is not reachable. Lyapunov-based methods are a key theoretical tool in attitude studies, enabling dynamics and control analysis that ensures stability for nonlinear (MARKLEY; CRASSIDIS, 2014). In such cases, the equilibrium state analysis is helpful to identify conditions under which the system is either at rest or in uniform motion (HUGHES, 2004). Each equilibrium suggests a potential method for attitude stabilization. The investigation of equilibria, their stability properties, and their applications are the main topics of discussion in this work.

Control

Attitude control comprises two aspects: stabilization and control. Stabilization maintains a set orientation, while control actively reorients the spacecraft as needed (WERTZ, 1973). Most modern spacecraft are stabilized through a combo of passive and active control methods (HUGHES, 2004). However, this work will primarily focus on passive stabilization techniques, specifically gravitational stabilization. A brief discussion will also be provided on the interface between passive and active control, aiming to demonstrate the leverage of allying both methods.

2.1 ATTITUDE REPRESENTATION

To describe the orientation of a spacecraft or its components, we first need to establish some basic concepts: attitude representation and reference frames. The orientation vectors of the spacecraft can be defined relative to various directions, such as the Sun, Earth, a distant galaxy, or another spacecraft (WERTZ, 1973; HUGHES, 2004). The orientation of a vector is defined only in relation to a reference system (HUGHES, 2004). In this context, the orientation of any vector v can be uniquely represented by the three direction cosines, or an attitude matrix, relating v to a reference vector—i.e., a reference frame.

2.1.1 Attitude Matrix

Spacecraft attitude determination focuses on describing a proper set of direction cosines, an orthogonal and unit length matrix, that transforms vectors from a space-fixed reference frame to one fixed on the spacecraft. This involves studying 3x3 proper orthonormal - orthogonal and unit length - matrices that will be referred as rotation or attitude matrices, and denoted by the letter $\mathbf{A}$ (MARKLEY; CRASSIDIS, 2014).

Euler's Theorem states a key property of attitude matrices: any rotation can be described as a rotation around a fixed axis. Note that the transformation of a vector representation $\mathbf{x}_F$ from reference frame F to reference frame G, using the attitude matrix A_{GF} (MARKLEY; CRASSIDIS, 2014), is expressed as

$$A_{GF}\mathbf{x}_F = \mathbf{x}_G. \tag{2.1}$$

2.1.2 Euler Angles

Every orthogonal 3×3 matrix has a rotation axis described by a unit vector $\mathbf{e}$ and an angle of rotation ϑ about this axis. This axis and angle are known as the Euler axis and Euler angle of the rotation.

The Euler angle describes a rotation from one frame to another by the product of three rotations. The angles ϕ, θ and ψ are used to specify the rotation about each of their own rotation axis, represented by e_ϕ, e_θ and e_ψ. The transformations using the Euler axis and angles can be employed in with several sequences of rotation. In the classical Euler angle representation, the rotation axes are given by

$$\mathbf{e}_1 = \begin{bmatrix} 1 \\ 0 \\ 0 \end{bmatrix}, \mathbf{e}_2 = \begin{bmatrix} 0 \\ 1 \\ 0 \end{bmatrix}, \mathbf{e}_3 = \begin{bmatrix} 0 \\ 0 \\ 1 \end{bmatrix} \tag{2.2}$$

and the compact notation

$$\mathbf{A}_{ijk}(\phi, \theta, \psi) = \mathbf{A}(\mathbf{e}_k, \psi)\mathbf{A}(\mathbf{e}_j, \theta)\mathbf{A}(\mathbf{e}_i, \phi). \tag{2.3}$$

The attitude matrix can be constructed by twelve sequences of rotation: six symmetric and six asymmetric, with the requirements $i \neq j$ and $j \neq k$. When dealing with an asymmetric

sequence, the Euler angles are commonly referred to as roll, pitch, and yaw angles (MARKLEY; CRASSIDIS, 2014). Roll is the rotation about the body axis closest to the direction of motion and is conventionally assigned to the matrix $\mathbf{A}(\mathbf{e}_1, \phi)$. Yaw is the rotation about the body axis closest to the gravity direction and is commonly assigned to $\mathbf{A}(\mathbf{e}_3, \psi)$. Lastly, pitch is the rotation about the remaining body axis and describes the up and down pointing, assigned to $\mathbf{A}(\mathbf{e}_j, \theta)$. The attitude of Earth-pointing spacecraft are often described by the $3-2-1$ sequence.

$$\begin{aligned}\mathbf{A}_{321}(\phi,\theta,\psi) =& \mathbf{A}(\mathbf{e}_1,\psi)\mathbf{A}(\mathbf{e}_2,\theta)\mathbf{A}(\mathbf{e}_3,\phi)\\ =& \begin{bmatrix} 1 & 0 & 0 \\ 0 & c\psi & s\psi \\ 0 & -s\psi & c\psi \end{bmatrix}\begin{bmatrix} c\theta & 0 & -s\theta \\ 0 & 1 & 0 \\ s\theta & 0 & c\theta \end{bmatrix}\begin{bmatrix} c\phi & s\phi & 0 \\ -s\phi & c\phi & 0 \\ 0 & 0 & 1 \end{bmatrix}\\ =& \begin{bmatrix} c\theta c\phi & c\theta s\phi & -s\theta \\ -c\psi s\phi + s\psi s\theta c\phi & c\psi c\phi + s\psi s\theta s\phi & s\psi c\theta \\ s\psi s\phi + c\psi s\theta c\phi & -s\psi c\phi + c\psi s\theta s\phi & c\psi c\theta \end{bmatrix}\end{aligned} \tag{2.4}$$

2.2 ATTITUDE KINEMATICS

In this section, we will derive the equations for the time derivatives of the attitude matrix and the Euler angles parametrization, introducing the angular velocity vector.

2.2.1 Attitude Matrix Kinematics

The time derivative of the attitude matrix is, by definition:

$$\dot{\mathbf{A}}_{GF}(t) \equiv \lim_{\Delta t\to 0} \frac{\mathbf{A}_{GF}(t+\Delta t) - \mathbf{A}_{GF}(t)}{\Delta t}. \tag{2.5}$$

Knowing that $\mathbf{A}_{FG}(t)\mathbf{A}_{GF}(t)$, we apply this relation in Eq. (2.5) and we have

$$\begin{aligned}\dot{\mathbf{A}}_{GF}(t) &= \left(\lim_{\Delta t\to 0} \frac{\mathbf{A}_{GF}(t+\Delta t) - \mathbf{A}_{GF}(t)}{\Delta t}\right)\mathbf{A}_{FG}(t)\mathbf{A}_{GF}(t)\\ &= \lim_{\Delta t\to 0} \frac{\mathbf{A}_{GF}(t+\Delta t)\mathbf{A}_{FG}(t) - I_3}{\Delta t}\mathbf{A}_{GF}(t).\end{aligned} \tag{2.6}$$

As $t \to 0$ we have that:

$$\lim_{\Delta t\to 0} \frac{\mathbf{A}_{GF}(t+\Delta t)\mathbf{A}_{FG}(t)}{\Delta t} \approx \lim_{\Delta t\to 0} \frac{I_3 - [\Delta\boldsymbol{\vartheta}_G^{GF}\times]}{\Delta t}. \tag{2.7}$$

The angular velocity is defined, in (MARKLEY; CRASSIDIS, 2014), by

$$\boldsymbol{\omega}_G^{GF}(t) \equiv \lim_{\Delta t\to 0} \frac{\Delta\boldsymbol{\vartheta}_G^{GF}}{\Delta t}. \tag{2.8}$$

Substituting Eq. (2.8) in Eq. (2.7), and then in Eq. (2.6), we have

$$\dot{\mathbf{A}}_{GF}(t) = -[\boldsymbol{\omega}_G^{GF}\times]\mathbf{A}_{GF}(t). \tag{2.9}$$

The frame labels can be exchanged in ω by the following identity

$$\boldsymbol{\omega}_G^{FG} = -\boldsymbol{\omega}_G^{GF}. \tag{2.10}$$

2.2.2 Vector Kinematics

Considering two different representations of a vector $\mathbf{x}_G = \mathbf{A}_{GF}\mathbf{x}_F$, the time derivative form is given by:

$$\begin{aligned}\dot{\mathbf{x}}_G =& \mathbf{A}_{GF}\dot{\mathbf{x}}_F + \dot{\mathbf{A}}_{GF}\mathbf{x}_F,\\ =& \mathbf{A}_{GF}\dot{\mathbf{x}}_F - \boldsymbol{\omega}_G^{GF}\times\mathbf{x}_G.\end{aligned} \tag{2.11}$$

This is a fundamental equation of vector kinematics. It expresses the derivative of $\dot{\mathbf{x}}_G$ in two components: the result of mapping the derivative $\dot{\mathbf{x}}_F$ from another frame by an orthogonal transformation, and an $\boldsymbol{\omega}_G^{GF}\times$ term that accounts for the rotational motion between the two frames. It's important to note that this equation only considers the relative rotation between the frames (MARKLEY; CRASSIDIS, 2014).

The vector addition of angular velocities id given by the following (MARKLEY; CRASSIDIS, 2014)

$$\boldsymbol{\omega}_H^{HF} = \boldsymbol{\omega}_H^{HG} + \mathbf{A}_{HG}\boldsymbol{\omega}_G^{GF} = \boldsymbol{\omega}_H^{H} + \boldsymbol{\omega}_H^{GF}. \tag{2.12}$$

2.2.3 Euler Angle Kinematics

For the sake of clarity and brevity, we will omit the full derivation, which can be found in detail in (MARKLEY; CRASSIDIS, 2014) and (HUGHES, 2004). Instead, we will directly derive the Euler angle kinematics by using the generalization of the attitude kinematics described in Eq. (2.9) and apply it to the attitude matrix in the Euler angles representation. The angular velocity for the Euler angles representation is given by:

$$\boldsymbol{\omega} = \dot{\psi}\mathbf{e}_\psi + \dot{\theta}\mathbf{A}(\mathbf{e}_\psi,\psi)\mathbf{e}_\theta + \dot{\phi}\mathbf{A}(\mathbf{e}_\psi,\psi)\mathbf{A}(\mathbf{e}_\theta,\theta)\mathbf{e}_\phi. \tag{2.13}$$

For the $3-2-1$ sequence of rotation, which is the one pertinent to the applications of this work, we have that $\boldsymbol{\omega}$ is:

$$\boldsymbol{\omega}_{321}(\phi,\theta,\psi) = \mathbf{A}(\mathbf{e}_1,\psi)\begin{bmatrix}1 & 0 & -\sin\theta\\ 0 & 1 & 0\\ 0 & 0 & \cos\theta\end{bmatrix}\begin{bmatrix}\dot{\psi}\\ \dot{\theta}\\ \dot{\phi}\end{bmatrix} = \begin{bmatrix}\dot{\psi}-\dot{\phi}\sin\theta\\ \dot{\phi}\cos\theta\sin\psi+\dot{\theta}\cos\psi\\ \dot{\phi}\cos\theta\cos\psi-\dot{\theta}\sin\psi\end{bmatrix} \tag{2.14}$$

Further, the attitude kinematics for the Euler angle representation for the sequence $3-2-1$ is given by substituting Eqs. (2.4) and (2.14) into Eq. (2.9):

$$\dot{\mathbf{A}}_{321}(\phi,\theta,\psi) = [\,\boldsymbol{\omega}_{321}(\phi,\theta,\psi)\times]\,\mathbf{A}_{321}(\phi,\theta,\psi). \tag{2.15}$$

2.3 REFERENCE FRAMES

In general, a reference frame is defined by its origin location and the orientation of its coordinate axes (MARKLEY; CRASSIDIS, 2014). The main objective of this section is to define the notations and conventions to be used in this work.

2.3.1 Body Frame

The body frame is defined by the three dimensions of Cartesian space originating at a specified point of the spacecraft. The body frame is used to align several components during the spacecraft assembly. Therefore, it is common practice to operationally define the body coordinate system based on the orientation of a navigation base (MARKLEY; CRASSIDIS, 2014). This navigation base is a spacecraft's subsystem that includes the most critical attitude sensors and payload instruments.

2.3.2 Inertial Frame

(WEINBERG, 1972) defines an inertial frame as a frame with constant velocity, non-rotating, relative to frames in which the universe resembles spherically symmetric. Some examples of the best realizations of inertial frames are: International Celestial Reference System (ICRF), and the approximate inertial frame Geocentric Inertial Frame (GCI) (MARKLEY; CRASSIDIS, 2014).

2.3.3 Orbital Frame: Local-Vertical/Local-Horizontal

Considering the dynamics of earth pointing, the orbital frame Local-Vertical/Local-Horizontal (LVLH) is very convenient once it defines the reference frame on the spacecraft's orbit. The z axis is defined along the nadir vector, the negative radial vector. The y axis is pointed opposite to the specific angular momentum vector, negative normal to the orbital plane. The x axis completes the triad, and it is defined along the orbital velocity vector. The dynamic equations describe the motion relative to an inertial frame. The rotation matrix from an inertial frame, represented by I, to LVLH, represented by O, is given by the Eq. (2.16) (MARKLEY; CRASSIDIS, 2014)

$$\mathbf{A}_{IO} = \begin{bmatrix} \dfrac{\mathbf{h}\times\mathbf{r}}{hr} & -\dfrac{\mathbf{h}}{h} & -\dfrac{\mathbf{r}}{r} \end{bmatrix}. \tag{2.16}$$

For Earth-oriented spacecraft the Roll-Pitch-Yaw (RPY) system is the most commonly used (WERTZ, 1973). On the LVLH reference frame the Roll axis is translated to the LVLH x axis, the Pitch axis is defined as the y axis, and the Yaw axis is the z axis. The LVLH frame with RPY coordinate system is represented in Figure 2.2.

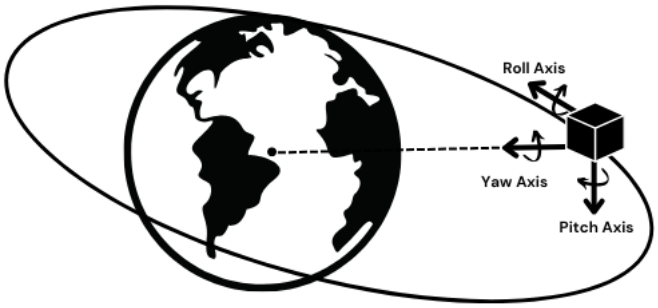

Figure 2.2. LVLH frame. Source: Adapted from (MARKLEY; CRASSIDIS, 2014) and (WERTZ, 1973).

2.4 ATTITUDE DYNAMICS

In this section, we will derive the fundamental equation of attitude dynamics, Euler's rotational equation. Along with this, the derivation of the moment of inertia tensor, angular momentum, and kinetic energy equations will also be developed. Furthermore, we will discuss some of the most used and discussed internal and external torques for passive and active ACDS

of spacecraft. This discussion is particularly pertinent as it provides the background for the results and applications presented in this work.

2.4.1 Rigid Body Dynamics

In the formulation of a rigid body's attitude dynamics, angular momentum is a key concept. Specifically, the angular momentum relative to the origin of an inertial coordinate frame is defined as:

$$\mathbf{H}^0 \equiv \sum_{i=1}^{n} \mathbf{r}^{i0} \times m_i \mathbf{v}^{i0}, \tag{2.17}$$

where m_i, $\mathbf{r}^{i0}$, $\mathbf{v}^{i0} = \dot{\mathbf{r}}^{i0}$ are, respectively, the mass, position, and velocity of the infinitesimal mass points that compound the body. Newton's second law of motion states that $m_i \dot{\mathbf{v}}^{i0} = \mathbf{F}_I^i$ in an inertial frame, and since $\mathbf{v}^0 \times \mathbf{v}^0 = 0$, the derivative of the angular momentum is

$$\dot{\mathbf{H}}_I^0 = \sum_{i=1}^{n} \mathbf{r}_I^{i0} \times \mathbf{F}_I^i \tag{2.18}$$

where $\mathbf{F}_I^i$ represents the internal and external forces acting on the body. According to Newton's third law of motion, the internal forces cancel each other out, resulting in the net torque about the origin being applied to the mass points as:

$$\dot{\mathbf{H}}_I^0 = \sum_{i=1}^{n} \mathbf{r}_I^{i0} \times \mathbf{F}_I^{\text{iext}} \equiv \mathbf{L}_I^0. \tag{2.19}$$

From the definition of center of mass, we have that

$$\mathbf{r}^{c0} \equiv \left(\sum_{i=1}^{n} m_i \mathbf{r}^{i0} \right) / M, \tag{2.20}$$

where $M \equiv \sum_{i=1}^{n} m_i$. If we rewrite the $\mathbf{r}^{ic} = (\mathbf{r}^{i0} - \mathbf{r}^0)$ and use the CM definition in Eq. (2.20), results in

$$\sum_{i=1}^{n} m_i \mathbf{r}^{ic} = \sum_{i=1}^{n} m_i (\mathbf{r}^{i0} - \mathbf{r}^{c0}) = M\mathbf{r}^{c0} - M\mathbf{r}^{c0} = 0. \tag{2.21}$$

It demonstrates that the motion of the CM and the motion of the mass points relative to the CM are not coupled. With this result, we can rewrite the angular momentum in terms of the CM motion

$$\begin{aligned} \mathbf{H}^0 &= \sum_{i=1}^{n} m_i (\mathbf{r}^{ic} + \mathbf{r}^{c0}) \times (\mathbf{v}^{ic} + \mathbf{v}^{c0}) = \sum_{i=1}^{n} m_i \mathbf{r}^{ic} \times \mathbf{v}^{ic} + \mathbf{r}^{c0} \times M\mathbf{v}^{c0} \\ &= \mathbf{H}^c + \mathbf{r}^{c0} \times M\mathbf{v}^{c0} \end{aligned} \tag{2.22}$$

The net torque can similarly be expressed as

$$\begin{aligned}\mathbf{L}^0 &= \sum_{i=1}^{n}(\mathbf{r}^{ic}+\mathbf{r}^{c0})\times\mathbf{F}_i^{\text{ext}} = \sum_{i=1}^{n}\mathbf{r}^{ic}\times\mathbf{F}_i^{\text{ext}} + \mathbf{r}^{c0}\times\sum_{i=1}^{n}\mathbf{F}_i^{\text{ext}} \\ &= \mathbf{L}^c + \mathbf{r}^{c0}\times\mathbf{F}\end{aligned} \tag{2.23}$$

where $\mathbf{F}$ is the net of external forces acting on the body. Within an inertial frame, we can substitute Eqs. (2.22) and (2.23) into Eq. (2.19)

$$\dot{\mathbf{H}}_I^c = \mathbf{L}_I^c. \tag{2.24}$$

The Eq. (2.24) is known as Euler's equation, and it is the fundamental equation of attitude dynamics. It describes the attitude motion of a rigid body's CM. It is important to note that this result holds even when the center of mass suffers acceleration, though it is derived for a non-rotation frame (MARKLEY; CRASSIDIS, 2014).

The rigid body designation comes from the reference frame, called body frame B, where the vectors $\mathbf{r}_B^{ic}$ remain constant. Any frame related to the body by an orthogonal transformation is also a body frame. Taking the time derivative of the vector $\mathbf{r}_B^{ic}$ and recalling the Eq. (2.11) we have that

$$\mathbf{v}^{i0} = \dot{\mathbf{r}}_I^{ic} = \mathbf{A}_{IB}\dot{\mathbf{r}}_B^{ic} - \boldsymbol{\omega}_I^{IB}\times\mathbf{r}_I^{ic} = \boldsymbol{\omega}_I^{BI}\times\mathbf{r}_I^{ic}. \tag{2.25}$$

Substituting Eq. (2.25) into Eq. (2.17) we have

$$\mathbf{H}_I^c = \sum_{i=1}^{n} m_i\mathbf{r}_I^{ic}\times(\boldsymbol{\omega}_I^{BI}\times\mathbf{r}_I^{ic}) = -\sum_{i=1}^{n} m_i[\mathbf{r}_I^{ic}\times]^2\boldsymbol{\omega}_I^{BI} = \mathbf{J}_I^c\boldsymbol{\omega}_I^{BI}. \tag{2.26}$$

The $\mathbf{J}_I^c$ is a real symmetric 3×3 matrix known as the Moment of Inertia (MOI) tensor, and it is by definition:

$$\mathbf{J}^c \equiv -\sum_{i=1}^{n} m_i[\mathbf{r}^{ic}\times]^2 = \sum_{i=1}^{n} m_i\left[||\mathbf{r}^{ic}||^2\mathbf{I}_3 - \mathbf{r}^{ic}(\mathbf{r}^{ic})^T\right]. \tag{2.27}$$

Eq. (2.27) is expressed in a general frame; however, the MOI is commonly expressed in the body frame where it remains constant. Therefore we will denote it as $\mathbf{J}_B$ the MOI tensor in the body frame throughout this work. The elements of the MOI tensor are given by the diagonal elements, known as the moments of inertia are given by:

$$[\mathbf{J}_B]_{11} = \sum_{i=1}^{N} m_i\left[(y_i-y_{cm})^2 + (z_i-z_{cm})^2\right], \tag{2.28}$$

$$[\mathbf{J}_B]_{22} = \sum_{i=1}^{N} m_i\left[(z_i-z_{cm})^2 + (x_i-x_{cm})^2\right], \tag{2.29}$$

$$[\mathbf{J}_B]_{33} = \sum_{i=1}^{N} m_i\left[(x_i-x_{cm})^2 + (y_i-y_{cm})^2\right], \tag{2.30}$$

and the off-diagonal elements, known as products of inertia:

$$[\mathbf{J}_B]_{12} = [\mathbf{J}_B]_{21} = -\sum_{i=1}^{N} m_i(x_i - x_{cm})(y_i - y_{cm}), \tag{2.31}$$

$$[\mathbf{J}_B]_{13} = [\mathbf{J}_B]_{31} = -\sum_{i=1}^{N} m_i(x_i - x_{cm})(z_i - z_{cm}), \tag{2.32}$$

$$[\mathbf{J}_B]_{23} = [\mathbf{J}_B]_{32} = -\sum_{i=1}^{N} m_i(y_i - y_{cm})(z_i - z_{cm}), \tag{2.33}$$

where m_i represents the mass and (x_i, y_i, z_i) are the coordinates of the i-th mass point. In addition, (x_{cm}, y_{cm}, z_{cm}) are the coordinates of the CM.

Therefore, the angular momentum in the body frame is given by

$$\mathbf{H}_B^c = \mathbf{J}_B^c \boldsymbol{\omega}_B^{BI}. \tag{2.34}$$

Another particularly useful body frame, which will be frequently employed in this work, is the frame aligned with the body's principal axes. These principal axes correspond to the eigenvectors of the MOI tensor. When the body is described in this principal axes frame, the MOI tensor simplifies, eliminating products of inertia and reducing to a diagonal form, with its eigenvalues corresponding to the principal moments of inertia, denoted as, J_1, J_2, J_3. An implicit fact in Eq. (2.34) is that a rigid body's angular velocity and angular momentum are parallel only if the body rotation is about a principal axis (MARKLEY; CRASSIDIS, 2014).

The body's rotation kinetic energy can also be expressed in terms of the MOI tensor, using the Eqs. (2.25) and the definition of the rotational kinetic energy. It is given by:

$$\begin{aligned} E_k^c =& \frac{1}{2}\sum_{i=1}^{n} m_i \|\mathbf{v}^{ic}\|^2 = \frac{1}{2}\sum_{i=1}^{n} m_i \left(\boldsymbol{\omega}_I^{BI} \times \mathbf{r}_I^{ic}\right)^T \left(\boldsymbol{\omega}_I^{BI} \times \mathbf{r}_I^{ic}\right), \\ =& \frac{1}{2}\sum_{i=1}^{n} m_i \left([\mathbf{r}_I^{ic}\times]\boldsymbol{\omega}_I^{BI}\right)^T \left([\mathbf{r}_I^{ic}\times]\boldsymbol{\omega}_I^{BI}\right) = \frac{1}{2}\left(\boldsymbol{\omega}_I^{BI}\right)^T \mathbf{J}_I^c \boldsymbol{\omega}_I^{BI}. \end{aligned} \tag{2.35}$$

Now, we can finally derive Euler's rotational equation for the body frame. To start, let us take the Eq. (2.11) and apply to the angular momentum in the inertial frame, Eq. (2.26):

$$\dot{\mathbf{H}}_B^c = \mathbf{A}_{BI}\dot{\mathbf{H}}_I^c + \dot{\mathbf{A}}_{BI}\mathbf{H}_I^c, \tag{2.36}$$

knowing that the external torques are sometimes easily calculated in the body frame, from Eq. (2.24), we have that

$$\mathbf{A}_{BI}\dot{\mathbf{H}}_I^c = \mathbf{L}_B^c. \tag{2.37}$$

From from Eqs. (2.11) and (2.34), we have that

$$\dot{\mathbf{A}}_{BI}\mathbf{H}_I^c = -\boldsymbol{\omega}_B^{BI} \times \mathbf{H}_B^c = \mathbf{J}_B^c \boldsymbol{\omega}_B^{BI}. \tag{2.38}$$

Therefore, the Euler's rotational equation is:

$$\mathbf{J}_B^c \dot{\boldsymbol{\omega}}_B^{BI} = \mathbf{L}_B^c - \boldsymbol{\omega}_B^{BI} \times \mathbf{J}_B^c \boldsymbol{\omega}_B^{BI}. \tag{2.39}$$

2.4.2 Spacecraft Torques

Torques acting on spacecraft can be classified as either internal or external. Internal torques, known as momentum exchange torques, arise from the exchange of angular momentum between the spacecraft's components without altering the total system's momentum. For internal torques, modeling the spacecraft as a single rigid body is insufficient; a more detailed model is required, as will be demonstrated when we incorporate reaction wheels into the dynamic system model.

External torques, on the other hand, result from interactions between the spacecraft and its external environment. Unlike internal torques, external torques change the overall angular momentum of the spacecraft. When considering only external torques, the single rigid body model provides an adequate description of the spacecraft's dynamics.

2.4.2.1 Gravitational Torque

The gravitational torque is an external torque and is crucial to the attitude dynamics of a spacecraft, its influence and particularities in the attitude motion in orbit are the main characters of this work. As stated by (MARKLEY; CRASSIDIS, 2014), any nonsymmetrical rigid body in a gravitational field is subjected to a gravitational torque. (HUGHES, 2004) further explains that for a rigid body in a uniform gravitational field, the center of mass would coincide with the center of gravity, resulting in zero gravity-gradient torque about the center of mass. However, in the space environment, the gravitational field is not uniform, and spacecraft are typically not perfectly symmetrical. This non-uniformity in gravitational forces across the spacecraft generates a gravitational torque about the body's center of mass, influencing its attitude dynamics (HUGHES, 2004).

As an external torque, the Gravity-Gradient torque changes the total angular moment of the vehicle. According to (MARKLEY; CRASSIDIS, 2014), the gravitational force of an ith mass point is given by:

$$\mathbf{F}^{iext} = m_i \mathbf{g}(\mathbf{r}^{i0}) = m_i \nabla_r U(\mathbf{r})|_{\mathbf{r}=\mathbf{r}^{i0}} \tag{2.40}$$

In which $U(\mathbf{r})$ is the gravity potential and the index 0 represents the origin of the systems' reference. The accuracy of the gravity potential function depends on the number of terms included in the power expansion series. For the analysis of GG torques on a spacecraft, including the J_2 term is normally enough. However, the J_2 effect becomes significant in the attitude motion of bodies with long and flexible appendages (WERTZ, 1973), which is not our study case. Therefore, disregarding the J_2 effect and assuming that only the first-order terms have significant contributions for Eq. (2.40), the expansion in power series is given by:

$$\mathbf{F}^{iext} = m_i \mathbf{g}(\mathbf{r}^{ic} + \mathbf{r}^{c0}) = m_i \sum_{n=0}^{\infty} \frac{g^{(n)}}{n!}(x - x_0)^n, \tag{2.41}$$

$$\mathbf{F}^{iext} = m_i[\mathbf{g}(\mathbf{r}^{c0}) + \nabla \mathbf{g}(r)^{c0}\mathbf{r}^{ic}]. \tag{2.42}$$

Knowing that $\mathbf{g}(r) = -\frac{\mu}{r^3}\mathbf{r}$ and that

$$\nabla \mathbf{g}(\mathbf{r}) = \nabla(\nabla U(\mathbf{r})). \tag{2.43}$$

The Eq. (2.43) turns to be:

$$\nabla \mathbf{g}(\mathbf{r}) = G(\mathbf{r}) = \begin{bmatrix} \frac{\partial}{\partial x} \\ \frac{\partial}{\partial y} \\ \frac{\partial}{\partial z} \end{bmatrix} \begin{bmatrix} \frac{-\mu x}{r^3} & \frac{-\mu y}{r^3} & \frac{-\mu z}{r^3} \end{bmatrix}. \tag{2.44}$$

Applying the partial derivatives results in the 3×3 symmetric matrix $G(\mathbf{r})$, which is the gravity-gradient tensor:

$$G(\mathbf{r}) = -\frac{\mu}{r^3}(\mathbf{I}_3 - 3\frac{\mathbf{r}\mathbf{r}^T}{r^2}). \tag{2.45}$$

The constant $\mu = m_E G$ is the gravitational parameter and r is the radial vector between the centers of mass of the central body and the vehicle. Applying Eq. (2.45) into Eq. (2.42), results in:

$$\mathbf{F}^{iext} = m_i[\mathbf{g}(\mathbf{r}) + G(\mathbf{r})\mathbf{r}^{ic}]. \tag{2.46}$$

The gravity-gradient torque can be obtained by substituting Eq. (2.46) into the definition of

torque:

$$\mathbf{L}_B^{\text{gg}} = \sum_{i=1}^{n} \mathbf{r}^{ic} \times m_i[\mathbf{g}(\mathbf{r}) - \frac{\mu}{r^3}(\mathbf{I}_3 + 3\frac{\mathbf{r}\mathbf{r}^T}{r^2})\mathbf{r}^{ic}], \tag{2.47}$$

$$\mathbf{L}_B^{\text{gg}} = \sum_{i=1}^{n} m_i\mathbf{r}^{ic} \times \mathbf{g}(\mathbf{r}) - \frac{\mu}{r^3}\sum_{i=1}^{n} m_i\mathbf{r}^{ic} \times (\mathbf{I}_3 + 3\frac{\mathbf{r}\mathbf{r}^T}{r^2})\mathbf{r}^{ic}. \tag{2.48}$$

After some vector algebra, the GG torque is given by (MARKLEY; CRASSIDIS, 2014):

$$\mathbf{L}_B^{\text{gg}} = \frac{3\mu}{r^3}\mathbf{n} \times \sum_{i=1}^{n} m_i \left[(r^{ic})^2\mathbf{I}_3 - \mathbf{r}^{ic}\mathbf{r}^{icT}\right]\mathbf{n}, \tag{2.49}$$

$$\mathbf{L}_B^{\text{gg}} = \frac{3\mu}{r^3}\mathbf{n} \times (\mathbf{J}^c\mathbf{n}), \tag{2.50}$$

in which $\mathbf{J}^c$ is the moment of inertia tensor with respect to the center of mass. Is important to notice that the Eq. (2.50) is represented in the LVLH frame respect to the vehicle's orbit. However, we want to represent the attitude respect to the LVLH frame. The 3-2-1 Euler sequence performs this transition from the LVLH frame to the body frame. This way, the unit nadir vector $\mathbf{n}$ can be written as:

$$\mathbf{n} = A_{321}(\phi, \theta, \psi)\begin{bmatrix} 0 \\ 0 \\ 1 \end{bmatrix} = \begin{bmatrix} -\sin\theta \\ \cos\theta\sin\psi \\ \cos\theta\cos\psi \end{bmatrix}. \tag{2.51}$$

Thus, when applying Eq. (2.51) into Eq. (2.50) the Gravity-Gradient Torque in the body frame is given by

$$\mathbf{L}_B^{\text{gg}} = \frac{3\mu}{r^3}\begin{bmatrix} (J_3 - J_2)\cos^2\theta\cos\psi\sin\psi \\ (J_3 - J_1)\cos\theta\sin\theta\cos\psi \\ (J_1 - J_2)\cos\theta\sin\theta\sin\psi \end{bmatrix}. \tag{2.52}$$

2.4.2.2 Magnetic Torque

The magnetic torque consists of the interaction of the magnetic dipole generated by the actuator with the geomagnetic field expressed in the body frame, that is

$$\mathbf{L}_B^{\text{mag}} = \mathbf{m} \times \mathbf{B}, \tag{2.53}$$

where $\mathbf{L}_B^{\text{mag}}$ is the magnetic control torque given in Nm, $\mathbf{m}$ is the magnetic dipole moment given by (ARDUINI; BAIOCCO, 1997)

$$\mathbf{m} = (\mathbf{B} \times \mathbf{L}_B^{\text{mag}})/B^2, \tag{2.54}$$

in Am^2, and $\mathbf{B}$ is the geomagnetic field vector on the body frame and $B = ||\mathbf{B}||$, both given in Tesla.

The strength of the geomagnetic field decreases with the inverse cube of the distance from the Earth's center, thus magnetic control is majorly used in near-Earth orbits, where the geomagnetic field magnitude is higher, ranging from 20-50 μT. Commercially available magnetorquers can provide dipoles from 1-1000 Am^2, therefore resulting in control torques of $2 \cdot 10^{-5}$ to 0.05 Nm.

Attitude control using magnetorquers was first proposed in the early 1960s (MARKLEY; CRASSIDIS, 2014). The main use in today's missions include detumbling, initial acquisition, precession control, nutation damping, and momentum control (ARDUINI; BAIOCCO, 1997; AVANZINI *et al.*, 2019; WIśNIEWSKI; BLANKE, 1999; OVCHINNIKOV; ROLDUGIN, 2019; OVCHINNIKOV *et al.*, 2018; ZHANG *et al.*, 2019). One advantage of magnetic control is that they produce no force, therefore not disturbing the body's orbit.

On the other hand, a significant disadvantage is that the magnetic torque is constrained in the orthogonal plane of the magnetic field, so they can control only two of the body axes at a given moment. Because of it, magnetic control is usually employed with other control method, such as GG stabilization (MARKLEY; CRASSIDIS, 2014; WIśNIEWSKI; BLANKE, 1999; ARDUINI; BAIOCCO, 1997) and reaction wheels (AVANZINI *et al.*, 2019; MARKLEY; CRASSIDIS, 2014).

Integrating magnetorquers and reaction wheels can be very beneficial for attitude stabilization. The reaction wheels deliver precise pointing accuracy, while the magnetorquers help manage the accumulated momentum in the wheels (HOGAN; SCHAUB, 2015). This collaboration removes the need for desaturation maneuvers and prolongs the lifespan of the reaction wheels (AVANZINI *et al.*, 2019).

2.4.2.3 Reaction Wheels

Reaction wheels are devices that produce internal torques in the spacecraft. They are governed by principles of angular momentum and Newton's third law of motion, specifically the conservation of angular momentum(MARKLEY; CRASSIDIS, 2014). As mentioned in the beginning of this section, for accounting an internal torque we cannot consider the whole system

a single rigid body. Although we can equation the total angular momentum on the body frame as

$$\mathbf{H}_B = \mathbf{J}_B^c \boldsymbol{\omega}_B^{BI} + \mathbf{H}_B^w, \tag{2.55}$$

where $\mathbf{H}_B^w$ is the angular momentum generated by the reaction wheels. Applying the time derivative to $\mathbf{H}_B^w$ we have that:

$$\dot{\mathbf{H}}_B^w = \mathbf{L}_B^w, \tag{2.56}$$

where $\mathbf{L}_B^w$ is the torque produced by the reaction wheels. Now we can include the angular momentum and torque generated by the reaction wheels into the Euler's rotational equation:

$$\mathbf{J}_B^c \dot{\boldsymbol{\omega}}_B^{BI} = \mathbf{L}_B^c - \mathbf{L}_B^w - \boldsymbol{\omega}_B^{BI} \times (\mathbf{J}\boldsymbol{\omega}_B^{BI} + \mathbf{H}_B^w). \tag{2.57}$$

Because of Newton's third law of motion, the reaction wheels' torque comes to Euler's rotational equation with a negative sign. The effective wheel torque input is calculated as (MARKLEY; CRASSIDIS, 2014):

$$\mathbf{L}_{\text{eff}}^w = -\mathbf{L}_B^w - \boldsymbol{\omega}_B^{BI} \times \mathbf{H}_B^w. \tag{2.58}$$

Reaction wheels are one of the most popular actuators for spacecraft attitude control. These devices are available with a broad range of capabilities, including maximum torque between 0.01 and 1.0 Nm, maximum angular momentum ranging from 2 to 250 Nms, and maximum rotational speeds from 1000 to 6000 rpm (MARKLEY; CRASSIDIS, 2014). While momentum-bias spacecraft may use one or two reaction wheels for underactuated control (CHAURAIS *et al.*, 2015; HORRI; PALMER, 2012; JIN *et al.*, 2008; KRISHNAN *et al.*, 1995), three-axis attitude control requires three or more wheels (MARKLEY; CRASSIDIS, 2014; AVANZINI *et al.*, 2019; HOGAN; SCHAUB, 2015; LEE *et al.*, 2016; WANG *et al.*, 2003). Since the system of spacecraft and reaction wheels conserves momentum, any perturbing torques acting on the spacecraft must be absorbed by the wheels to maintain precise pointing (HOGAN; SCHAUB, 2015). Consequently, a practical consideration when using reaction wheels is the need for momentum dumping.

2.5 POWER GENERATION

A spacecraft is composed of several subsystems, that may or not affect each other's functioning. The Electrical Power System (EPS) guarantees the correct energy generation, distribution,

and storage for all subsystems throughout the mission. Therefore, the EPS must be designed considering all stages of its life cycle to accomplish the satellite's mission without faults (LARSON, 1999).

The entire EPS is designed according to the capacity of electrical power generation (CAPPELLETTI *et al.*, 2020). The different electric power sources available for spacecrafts include solar photovoltaic cells, radioisotope thermoelectric generators, nuclear reactors, and fuel cells (LARSON, 1999). In small satellite mission, the most commonly adopted model is commercial solar panels (CAPPELLETTI *et al.*, 2020). The power generated by a cubesat's solar panels can be calculated using the following:

$$P_{sa} = P_{in}\ \eta\ A_{eff}\ \cos\theta, \tag{2.59}$$

where P_{sa} is the power generated by the solar array, P_{in} is the solar irradiance of 1358 $\mathrm{W/m^2}$, η is the solar cell efficiency, A_{eff} is the area of the solar panel, and θ is the angle of incidence which is the angle between the incoming sunlight and the normal (perpendicular) to the surface of the panel (CAPPELLETTI *et al.*, 2020; YOST; WESTON, 2023).

As seen in Eq. (2.59), the maximum power generated by the solar array occurs when the incidence angle is zero degrees. For this reason, some satellites require the use of Sun-tracking arrays or specific attitude control systems to ensure maximum power generation.

When in orbit, the body will certainly experience some rotation or tumbling. Concerning body-mounted solar array satellites, this attitude motion causes the angle of sunlight incidence to constantly change. This results in the fluctuation of the power generated by solar cells. To estimate the power generation, it is important to account for both the satellite's attitude dynamics and the temperature variations of the solar array (CAPPELLETTI *et al.*, 2020). Sometimes the variation in sunlight incidence can even serve as an opportunity to improve the satellite's thermal design (FISCHELL; MOBLEY, 1964).

A study comparing the power generation of three attitude control scenarios in a body-mounted solar array 3U CubeSat: free-orientation[1], sun-pointing, and nadir-pointing can be seen in (SÁNCHEZ-SANJUÁN *et al.*, 2016). It was shown that the power generation in the free-orientation scenario closely matched the sun-pointing scenario.

[1]Rigid body subjected only to GG torque in the study case of (SÁNCHEZ-SANJUÁN *et al.*, 2016)

Employing GGS proves particularly advantageous, as it minimizes power consumption by relying on passive attitude control, making it inherently more power-efficient. Furthermore, GGS, which we will develop in details in chapter 3, facilitates power generation for all six faces of the satellite across varying orientations, with the capability to harvest energy from up to three faces simultaneously (SáNCHEZ-SANJUáN *et al.*, 2016). A study to analyze the power generation profile for CubeSat sizes from 1-6U under GGS is part of the contributions of this work as shown in the sequel (AVELINO *et al.*, 2024).

CHAPTER 3

GRAVITY-GRADIENT STABILIZATION

In this chapter, we establish the fundamentals for understanding and predicting the attitude motion of various types of spacecraft (HUGHES, 2004). These principles serve as the foundation for designing specific attitude behaviors, helping to optimize the design process concerning stability analysis and control within the CubeSat standard.

Certain missions demand not only a stable attitude but also precise pointing. In such cases, passive stabilization can support active attitude control, enhancing accuracy and reducing the control inputs. Some stabilization techniques leverage the spacecraft's inherent dynamics, using either built-in design elements, such as discrete dampers, or natural force fields to produce stabilizing torque.

One notable passive stabilization method is Gravity-Gradient Stabilization which relies on the action of the gravitational torque, described in section 2.4.2.1. This method provides stabilization along one, two, or three axes by using the differential gravitational force acting on the spacecraft to generate torque (HUGHES, 2004). In this chapter, we will derive the equations of rotational motion with gravity-gradient torque, perform the linear approximation of the nonlinear equations, and analyze the system stability around an equilibrium point.

It is widely known that the GG Torque is a helpful passive method for stabilizing the attitude regarding earth-pointing (MARKLEY; CRASSIDIS, 2014; HUGHES, 2004). The most useful reference frame to describe an earth-pointing system is the LVLH frame (see section 2.3.3) due to the close alignment of the body axes to the LVLH frame. The Euler sequence 3-2-1 is convenient for describing the orientation of the body axes to the LVLH frame (see section 2.1.2).

3.1 ATTITUDE KINEMATICS

From the vector addition of angular velocities, Eq. (2.12), the angular velocity vector on the body frame concerning the inertial frame is defined

$$\boldsymbol{\omega}_B^{BI} = \boldsymbol{\omega}_B^{BO} + \mathbf{A}_{BO}\boldsymbol{\omega}_O^{OI}. \tag{3.1}$$

The body's angular velocity with respect to LVLH frame, $\boldsymbol{\omega}_B^{BO}$, is given by Eq. (2.14). Additionally, $\boldsymbol{\omega}_O^{OI}$ is obtained from the following equation:

$$[\boldsymbol{\omega}_O^{OI}\times] = \dot{\mathbf{A}}_{OI}\mathbf{A}_{OI}^T = \begin{bmatrix} 0 & \omega_3 & \omega_2 \\ -\omega_3 & 0 & \omega_1 \\ \omega_2 & \omega_1 & 0 \end{bmatrix}, \tag{3.2}$$

$$\omega_1 = \frac{d}{dt}\left(\frac{\mathbf{r}}{r}\right)\cdot\frac{\mathbf{h}}{h}, \tag{3.3}$$

$$\omega_2 = \frac{d}{dt}\left(-\frac{\mathbf{r}}{r}\right)\cdot\frac{\mathbf{h}\times\mathbf{r}}{hr}, \tag{3.4}$$

$$\omega_3 = \frac{d}{dt}\left(\frac{\mathbf{h}}{h}\right)\cdot\frac{\mathbf{h}\times\mathbf{r}}{hr}. \tag{3.5}$$

With some straightforward algebra, we reach the result:

$$\boldsymbol{\omega}_O^{OI} = \begin{bmatrix} 0 & \frac{-h}{r^2} & \frac{r(\ddot{\mathbf{r}}\cdot\mathbf{h})}{h^2} \end{bmatrix}^T. \tag{3.6}$$

The third component of the $\boldsymbol{\omega}_O^{OI}$ will be considered equal to zero for this analysis[1]. Introducing some orbital parameters:

$$\ddot{\mathbf{r}} = -\mu\mathbf{r}/r^3, \tag{3.7}$$

$$r = \frac{h^2/\mu}{1+e\cos f}, \tag{3.8}$$

$$h = \sqrt{\mu a(1-e^2)}, \tag{3.9}$$

$$\eta = \sqrt{\frac{\mu}{a^3}}. \tag{3.10}$$

The Eq. (3.7) is the gravitational acceleration. The Eq. (3.8) is the description of the orbit radius, where h^2/μ is the geometric parameter known as the semi-latus rectum, e is the orbit eccentricity and f is the true anomaly. The Eq. (3.9) is the value of the orbit angular momentum, where μ is the gravitational parameter and a is the major semi-axis of the orbit. The

[1]If the gravitational acceleration is not perpendicular to the angular momentum of the orbit indicates that the orbital plane precesses. This phenomenon is caused by the J_2 disturbance in the gravitational field. This disturbance generates a nonspherical gravitational field, which causes the $\ddot{\mathbf{r}}\cdot\mathbf{h}$

Eq. (3.10) is known as the orbital mean motion. Substituting Eqs. (3.8) to (3.10) into Eq. (3.6) states the following equation:

$$\boldsymbol{\omega}_O^{OI} = \begin{bmatrix} 0 & -\eta\frac{(1+e\cos f)^2}{\sqrt{(1-e^2)^3}} & 0 \end{bmatrix}^T. \tag{3.11}$$

Substituting Eqs. (2.14) and (3.11) into Eq. (3.1)

$$\boldsymbol{\omega}_B^{BI} = \begin{bmatrix} \dot{\psi} - \dot{\phi}s\theta \\ \dot{\phi}c\theta s\psi + \dot{\theta}c\psi \\ \dot{\phi}c\theta c\psi - \dot{\theta}s\psi \end{bmatrix} + A_{321}(\phi,\theta,\psi) \begin{bmatrix} 0 \\ -\eta\frac{(1+e\cos f)^2}{\sqrt{(1-e^2)^3}} \\ 0 \end{bmatrix}, \tag{3.12}$$

$$\boldsymbol{\omega}_B^{BI} = \begin{bmatrix} \dot{\psi} - \dot{\phi}s\theta \\ \dot{\phi}c\theta s\psi + \dot{\theta}c\psi \\ \dot{\phi}c\theta c\psi - \dot{\theta}s\psi \end{bmatrix} - \eta\frac{(1+e\cos f)^2}{\sqrt{(1-e^2)^3}} \begin{bmatrix} c\theta s\phi \\ c\psi c\phi + s\psi s\theta s\phi \\ -s\psi c\phi + c\psi s\theta s\phi \end{bmatrix}, \tag{3.13}$$

where s is the abbreviation for sine and c for cosine. Calling $n = \eta\frac{(1+e\cos f)^2}{\sqrt{(1-e^2)^3}}$, we have that

$$\boldsymbol{\omega}_B^{BI} = \begin{bmatrix} \dot{\psi} - \dot{\phi}s\theta - nc\theta s\phi \\ \dot{\phi}c\theta s\psi + \dot{\theta}c\psi - n(c\psi c\phi + s\psi s\theta s\phi) \\ \dot{\phi}c\theta c\psi - \dot{\theta}s\psi + n(s\psi c\phi + c\psi s\theta s\phi) \end{bmatrix}. \tag{3.14}$$

Taking the time derivative of $\boldsymbol{\omega}_B^{BI}$ as

$$\mathbf{g}(\mathbf{y}) = \begin{bmatrix} g_1(\mathbf{y}) & g_2(\mathbf{y}) & g_3(\mathbf{y}) \end{bmatrix}^T = \dot{\boldsymbol{\omega}}_B^{BI}, \tag{3.15}$$

$$\mathbf{y} = \begin{bmatrix} \ddot{\phi} & \ddot{\theta} & \ddot{\psi} & \dot{\phi} & \dot{\theta} & \dot{\psi} & \phi & \theta & \psi \end{bmatrix}^T, \tag{3.16}$$

the kinematics of the motion is completely described as:

$$g_1(\mathbf{y}) = \ddot{\psi} - \ddot{\phi}s\theta - \dot{\phi}\dot{\theta}c\theta - \dot{n}c\theta s\phi - n(\dot{\theta}s\theta s\phi + \dot{\phi}c\theta c\phi) \tag{3.17}$$

$$\begin{aligned} g_2(\mathbf{y}) = {} & \ddot{\phi}c\theta s\psi - \dot{\phi}\dot{\theta}s\theta s\psi + \dot{\phi}\dot{\psi}c\theta c\psi + \ddot{\theta}c\psi - \dot{\theta}\dot{\psi}s\psi \\ & - n(-\dot{\psi}s\psi c\phi - \dot{\phi}s\theta - \dot{\psi}c\psi s\theta s\phi + \dot{\theta}s\psi c\theta s\phi + \dot{\phi}s\psi s\theta c\phi) \\ & - \dot{n}(c\psi c\phi + s\psi s\theta s\phi) \end{aligned} \tag{3.18}$$

$$\begin{aligned} g_3(\mathbf{y}) = {} & \ddot{\phi}c\theta c\psi - \dot{\phi}\dot{\theta}s\theta c\psi - \dot{\phi}\dot{\psi}c\theta s\psi + \ddot{\theta}s\psi - \dot{\theta}\dot{\psi}c\psi \\ & - n(-\dot{\psi}c\psi c\phi - \dot{\phi}s\theta s\phi - \dot{\psi}s\psi s\theta s\phi - \dot{\theta}c\psi c\theta s\phi - \dot{\phi}c\psi s\theta c\phi) \\ & - \dot{n}(s\psi c\phi + c\psi s\theta s\phi). \end{aligned} \tag{3.19}$$

3.2 ATTITUDE DYNAMICS

Euler's rotational equations govern the attitude dynamics of a rigid body, Eq. (2.39), and finding its attitude over time requires integrating these equations. While no general closed-form solution exists for this system (HUGHES, 2004), various approximation methods have been employed to analyze the dynamic behavior within a specific neighborhood. For the stability analysis in this work, we used linearization and Lyapunov stability method.

To perform the linearization of the system we considered the following assumptions:

Assumption 3.2.1 *Circular orbit.*

Assumption 3.2.2 *Euler angles are small enough to approximate the cosines by 1 and sines by the angles themselves.*

With these assumptions, we have that $n = \eta$ and $\dot{n} = 0$, therefore

$$\boldsymbol{\omega}_B^{BI} = \begin{bmatrix} \dot{\psi} - \dot{\phi}\theta - \eta\phi \\ \dot{\phi}\psi + \dot{\theta} - \eta(1 + \psi\theta\phi) \\ \dot{\phi} - \dot{\theta}\psi + \eta(\psi + \theta\phi) \end{bmatrix}. \tag{3.20}$$

With the circular orbit assumption $r = a$ and the Eq. (3.10) turns to be:

$$\eta = \sqrt{\frac{\mu}{r^3}}. \tag{3.21}$$

Applying Eq. (3.21) and 3.2.2 into Eq. (2.50) results in

$$\mathbf{L}_{gg} = 3\eta^2 \begin{bmatrix} (J_3 - J_2)\psi \\ (J_3 - J_1)\theta \\ (J_1 - J_2)\theta\psi \end{bmatrix}, \tag{3.22}$$

where $\eta = \sqrt{\frac{\mu}{r^3}}$ is the mean orbital motion for a circular orbit. Applying the assumptions in Eqs. (3.17) to (3.19), we have that:

$$g_1(\mathbf{y}) = \ddot{\psi} - \ddot{\phi}\theta - \dot{\phi}\dot{\theta} - \eta(\dot{\theta}\theta\phi + \dot{\phi}) \tag{3.23}$$

$$g_2(\mathbf{y}) = \ddot{\phi}\psi - \dot{\phi}\dot{\theta}\theta\psi + \dot{\phi}\dot{\psi} + \ddot{\theta} - \dot{\theta}\dot{\psi}\psi - \eta(-\dot{\psi}\psi - \dot{\phi}\theta - \dot{\psi}\theta\phi + \dot{\theta}\psi\phi + \dot{\phi}\psi\theta) \tag{3.24}$$

$$g_3(\mathbf{y}) = \ddot{\phi} - \dot{\phi}\dot{\theta}\theta - \dot{\phi}\dot{\psi}\psi + \ddot{\theta}\psi - \dot{\theta}\dot{\psi} - \eta(-\dot{\psi} - \dot{\phi}\theta\phi - \dot{\psi}\psi\theta\phi - \dot{\theta}\phi - \dot{\phi}\theta). \tag{3.25}$$

Now, substituting Eqs. (3.20) and (3.22) to (3.25) in Eq. (2.39) and isolating the Euler angles acceleration, we will have a set of equations with the general form of

$$\dot{\mathbf{x}} = \mathbf{f}(\mathbf{x}, t), \tag{3.26}$$

where

$$\mathbf{x} = \begin{bmatrix} \dot{\phi} & \dot{\theta} & \dot{\psi} & \phi & \theta & \psi \end{bmatrix}^T. \tag{3.27}$$

3.3 LINEAR APPROXIMATION

We now consider a linear approximation starting with the general form Eq. (3.26) around the point $\mathbf{f}(\mathbf{0}, t) \equiv \mathbf{0}$ (typically $\mathbf{f}$ is stationary or periodic). The approximation is based on a Taylor expansion, resulting in (HUGHES, 2004):

$$\dot{\mathbf{x}} = \mathbf{A}(t)\mathbf{x} + \mathbf{n}(\mathbf{x}, t), \tag{3.28}$$

where

$$\mathbf{A}(t) \triangleq \left[\frac{\partial \mathbf{f}(\mathbf{x}, t)}{\partial \mathbf{x}^T}\right]_{\mathbf{x}=\mathbf{0}} \tag{3.29}$$

$$\mathbf{n}(\mathbf{0}, t) = \mathbf{0}. \tag{3.30}$$

Eq. (3.29) uses a compact notation for the Jacobian matrix of $\mathbf{f}$ with respect to state vector $\mathbf{x}$, denoted as:

$$\frac{\partial \mathbf{f}}{\partial \mathbf{x}^T} \triangleq \begin{bmatrix} \frac{\partial f_1}{\partial x_1} & \cdots & \frac{\partial f_1}{\partial x_n} \\ \vdots & \ddots & \vdots \\ \frac{\partial f_n}{\partial x_1} & \cdots & \frac{\partial f_n}{\partial x_n} \end{bmatrix}. \tag{3.31}$$

With the linear part of $\mathbf{f}$ extracted by Eq. (3.29), the remaining term, $\mathbf{n}(\mathbf{0}, t)$, is nonlinear and satisfies (HUGHES, 2004)

$$||\mathbf{n}(\mathbf{x}, t)|| = o(||\mathbf{x}||) \tag{3.32}$$

uniformly in t, which implies:

$$\lim_{||\mathbf{x}||\to 0} o(||\mathbf{x}||) = 0. \tag{3.33}$$

Thus, as $\mathbf{x}(t)$ approaches the origin, the term $o(||\mathbf{x}||)$ becomes increasingly negligible. The purpose of this linear approximation is to allow stability analysis of Eq. (3.28) via linear approximation:

$$x(t) \doteq \delta x(t) \tag{3.34}$$

where

$$\dot{\delta x} = A(t)\delta x. \tag{3.35}$$

The main advantage of Eq. (3.35) is that it allows for easier analytical handling. The linear approximation remains valid as $\mathbf{x}$ nears the origin, where the nonlinear term $\mathbf{n}(\mathbf{x},t)$ becomes negligible.

Calculating the Jacobian matrix of the general nonlinear system Eq. (3.26) it follows that:

$$\mathbf{A} = \begin{bmatrix} 0 & 0 & \eta - \eta\kappa_1 & -4\eta^2\kappa_1 & 0 & 0 \\ 0 & 0 & 0 & 0 & -3\eta^2\kappa_2 & 0 \\ -\eta + \eta\kappa_3 & 0 & 0 & 0 & 0 & -\eta^2\kappa_3 \\ 1 & 0 & 0 & 0 & 0 & 0 \\ 0 & 1 & 0 & 0 & 0 & 0 \\ 0 & 0 & 1 & 0 & 0 & 0 \end{bmatrix}, \tag{3.36}$$

where κ_1, κ_2, and κ_3 are the inertia ratios (HUGHES, 2004) given by:

$$\kappa_1 = \frac{J_2 - J_3}{J_1}, \tag{3.37}$$

$$\kappa_2 = \frac{J_1 - J_3}{J_2}, \tag{3.38}$$

$$\kappa_3 = \frac{J_2 - J_1}{J_3}. \tag{3.39}$$

3.3.1 Relative equilibria state

It is important to note the existence of equilibrium states where relative motion is zero. These states, known as relative equilibria, occur when the satellite rotates uniformly in the inertial frame while remaining fixed in the orbital frame (HUGHES, 2004). The relative equilibria for our case study is

$$\dot{\psi} = \dot{\theta} = \dot{\phi} = \psi = \theta = \phi = 0. \tag{3.40}$$

If we substitute this condition in Eq. (3.20), we can notice that the body rotates about the inertial frame with the orbital mean motion, i.e., the orbital velocity:

$$\boldsymbol{\omega}_B^{BI} = \begin{bmatrix} 0 & -\eta & 0 \end{bmatrix}. \tag{3.41}$$

Hence, we conclude that when one principal axis is vertical, the second principal axis is perpendicular to the orbit, and Earth-oriented equilibrium is respected (HUGHES, 2004; MARKLEY; CRASSIDIS, 2014). Additionally, there are 24 equilibria states: each of the three principal axes can point downward with two possible orientations, and each of the two transverse axes can align with the orbit normal vector in two directions, yielding 24 combinations. (LIKINS;

ROBERSON, 1966) have proved that these are the only equilibria states if the body has triaxial symmetry.

Since some of these equilibria are stable, benefiting the possibility of GGS for Earth-pointing satellites, we will analyze the stability of the linearized system using the Lyapunov method.

3.3.2 Stability of the Linearized System

A mathematical definition of stability must capture the essential qualities of stability for a specific application while being analytically manageable. For example, the Lagrange definition, which considers all bounded motions as stable, meets analytical requirements but is not sufficiently stringent for certain purposes, as it allows large, though bounded, deviations (HUGHES, 2004). On the other hand, Lyapunov's definition, widely regarded as the most successful, addresses this limitation by specifying that a motion is stable only if it remains within a predetermined, acceptable bound. This bound can be set arbitrarily low, ensuring stability for small disturbances, and is adaptable to different applications (HUGHES, 2004).

To define Lyapunov stability, consider the following differential system:

$$\dot{y} = g(y, t). \tag{3.42}$$

We focus on a specific solution $\mathbf{y}(t : \mathbf{y}_0, t_0)$ that starts from an initial condition $\mathbf{y} = \mathbf{y}_0$ at $t = t_0$. This solution represents the system's trajectory over time. Assuming that $\mathbf{g}(\mathbf{y}, t)$ meets conditions for existence and uniqueness, there is only one solution for each initial condition.

Now, consider all solutions that start near $\mathbf{y}_0$ at t_0 but differ by a small amount $\Delta\mathbf{y}$, called the perturbation. The trajectory of this perturbed solution will differ from the original by an amount:

$$\Delta\mathbf{y}(t; \mathbf{y}_0, \Delta\mathbf{y}_0, t_0) \triangleq \mathbf{y}(t; \mathbf{y}_0 + \Delta\mathbf{y}_0, t_0) - \mathbf{y}(t; \mathbf{y}_0, t_0), \tag{3.43}$$

where $\Delta\mathbf{y}$ represents the effect of the disturbance. The question of Lyapunov stability is whether this effect, $\Delta\mathbf{y}$, remains small for all times $t > t_0$, given that $\Delta\mathbf{y}_0$ is sufficiently small (but non-zero). If this condition holds, the solution $\mathbf{y}(t : \mathbf{y}_0, t_0)$ is considered stable in the sense of Lyapunov, or simply, L-stable.

Definition 3.3.1 (L-Stability) *The solution $\boldsymbol{y}(t : \boldsymbol{y}_0, t_0)$ is said to be Lyapunov stable (L-*

stable) if there exists a number $\delta > 0$ such that, for any preassigned $\epsilon > 0$, one can maintain $||\Delta \boldsymbol{y}|| < \epsilon$ for all $t \geq t_0$, by choosing any $\Delta \boldsymbol{y}_0$ subject to the constraint that $||\Delta \boldsymbol{y}_0|| < \delta$ (HUGHES, 2004).

Definition 3.3.2 (Instability) *The solution $\boldsymbol{y}(t : \boldsymbol{y}_0, t_0)$ is said to be unstable if it is not L-stable (HUGHES, 2004).*

Definition 3.3.3 (Attractive Solution) *The solution $\boldsymbol{y}(t : \boldsymbol{y}_0, t_0)$ is said to be attractive if there exists a number $\delta_A > 0$ such that $||\Delta \boldsymbol{y}|| \longrightarrow 0$ as $t \longrightarrow \infty$ for all $||\Delta \boldsymbol{y}_0|| < \delta_{\boldsymbol{A}}$ (HUGHES, 2004).*

Definition 3.3.4 (Asymptotic Stability) *The solution $\boldsymbol{y}(t : \boldsymbol{y}_0, t_0)$ is said to be asymptotically stable if it is both L-stable and attractive (HUGHES, 2004).*

Concerning engineering applications, the type of stability wanted is the asymptotically stable, which is both L-stable and attractive (HUGHES, 2004).

For linear or linearized stationary systems

$$\delta \dot{\mathbf{x}} = \mathbf{A} \delta \mathbf{x}, \tag{3.44}$$

we are interested in conditions where the origin is asymptotically stable, or Lyapunov stable. The following theorems are considered:

Theorem 3.3.1 *When the eigenvalues of λ_i of $\boldsymbol{A}$ are distinct, the solution $\delta \boldsymbol{x} \equiv \boldsymbol{0}$ of $\delta \dot{\boldsymbol{x}} = \boldsymbol{A} \delta \boldsymbol{x}$ is L-stable if $\max\{\sigma_i\} \leq 0$ (HUGHES, 2004).*

Theorem 3.3.2 *The solution $\delta \boldsymbol{x} \equiv \boldsymbol{0}$ of $\delta \dot{\boldsymbol{x}} = \boldsymbol{A} \delta \boldsymbol{x}$ is asymptotically stable if $\max\{\sigma_i\} < 0$ (HUGHES, 2004).*

Theorem 3.3.3 *The solution $\delta \boldsymbol{x} \equiv \boldsymbol{0}$ of $\delta \dot{\boldsymbol{x}} = \boldsymbol{A} \delta \boldsymbol{x}$ is unstable if $\max\{\sigma_i\} > 0$ (HUGHES, 2004).*

These theorems do not cover all cases (HUGHES, 2004). Based on these theorems the stability properties can be examined with the eigenvalues of the state matrix $\mathbf{A}$. This process is analytical for low-order systems ($n = 2,3,4$). However for intermediate-order systems ($n = 5, \ldots, 8$) - the stability criteria is addressed to the Routh-Hurwitz problem (HUGHES, 2004).

The Routh–Hurwitz problem seeks to determine if the eigenvalues of matrix $\mathbf{A}$ lie within the open left half-plane (LHP) by examining the coefficients of the characteristic polynomial

$$p_n(\lambda) \triangleq \det(\lambda\mathbf{I} - \mathbf{A}), \tag{3.45}$$

that gives

$$p_n(\lambda) \triangleq \lambda^n + a_1\lambda^{n-1} + \cdots + a_{n-1}\lambda + a_n. \tag{3.46}$$

The characteristic equation becomes:

$$p_n(\lambda) = 0. \tag{3.47}$$

While the exact locations of these roots λ_i might not be derived directly from the coefficients $\{a_1, \ldots, a_n\}$, a simplified question — whether all λ_i are in the LHP — can be answered by performing a finite set of arithmetic operations on the coefficients a_i (HUGHES, 2004).

The following result is considered in this work,

Theorem 3.3.4 *If any of the coefficients a_i is negative, then the solution $\delta x \equiv \boldsymbol{0}$ of $\delta\dot{\mathbf{x}} = \boldsymbol{A}\delta\boldsymbol{x}$ is unstable.*

This theorem provides necessary conditions for stability, allowing for a quick unstable detection.

3.3.3 Stability of Linear Stationary Mechanical Systems

Consider a linear mechanical system given by

$$\mathbf{M}\ddot{\mathbf{x}} + (\mathbf{D} + \mathbf{G})\dot{\mathbf{x}} + (\mathbf{K} + \mathbf{A})\mathbf{x} = \mathbf{f}(t), \tag{3.48}$$

which satisfies the following properties:

- $\mathbf{M}$ is symmetric and positive-definite.
- $\mathbf{D}$ is symmetric and negative-definite.
- $\mathbf{G}$ and $\mathbf{A}$ are skew-symmetric.
- $\mathbf{K}$ is symmetric.

The coefficient matrices $\mathbf{M}$, $\mathbf{D}$, $\mathbf{G}$, $\mathbf{K}$, and $\mathbf{A}$ correspond respectively to inertia, damping, gyric, stiffness, and constraint damping forces, while $\mathbf{f}(t)$ denotes any external forces acting on the system. Each element in $\mathbf{x}$ represents a physical displacement.

3.3.3.1 Conservative Systems

A conservative system is modeled by :

$$\mathbf{M}\ddot{\mathbf{x}} + \mathbf{K}\mathbf{x} = \mathbf{0}. \tag{3.49}$$

It is one of the most significant and well-understood systems in dynamics and asymptotic stability is not achievable (HUGHES, 2004).

Definition 3.3.5 (Static Stability) *A linear mechanical system that includes a term* $\boldsymbol{K}\mathbf{x}, \boldsymbol{K}^T = \boldsymbol{K}$*, is said to be statically stable if* $\boldsymbol{K} > 0$ *(HUGHES, 2004).*

Some authors prefer to define static stability with the simpler requirement $\det(\mathbf{K}) > 0$, as $\det(\mathbf{K}) = 0$ can be interpreted as a static stability boundary (HUGHES, 2004). In any case, the stability conditions for Eq. (3.49) are well established:

Theorem 3.3.5 *The system* $\boldsymbol{M}\ddot{\mathbf{x}} + \boldsymbol{K}\mathbf{x} = 0$*,* $\boldsymbol{M} = \boldsymbol{M}^T > 0$*,* $\boldsymbol{K}^T = \boldsymbol{K}$*, is stable if and only if it is statically stable (HUGHES, 2004).*

3.3.3.2 Conservative Gyric Systems

A system of the form

$$\mathbf{M}\ddot{\mathbf{x}} + \mathbf{G}\dot{\mathbf{x}} + \mathbf{K}\mathbf{x} = 0, \tag{3.50}$$

with $\mathbf{M}^T = \mathbf{M} > 0$, $\mathbf{G}^T = -\mathbf{G}$, and $\mathbf{K}^T = \mathbf{K}$ is known as a conservative gyric system. Because it is conservative, we obtain the following theorem:

Theorem 3.3.6 *The system of Eq.* (3.50)*, with* $\boldsymbol{M}^T = \boldsymbol{M} > 0$*,* $\boldsymbol{G}^T = -\boldsymbol{G}$*,* $\boldsymbol{K}^T = \boldsymbol{K}$*, is stable if it is statically stable (HUGHES, 2004).*

It is worth noting that, in comparison with Theorem 3.3.5, when the gyric term $\mathbf{G}\dot{\mathbf{x}}$ is added, static stability remains a sufficient condition for stability but is no longer a necessary one. It is also evident that asymptotic stability for Eq. (3.50) is impossible due to the nature of the characteristic equation:

$$p_{2N}(s) \triangleq \det(\mathbf{M}s^2 + \mathbf{G}s + \mathbf{K}) = 0. \tag{3.51}$$

The characteristic equation, Eq. (3.51), is a polynomial in s^2:

$$p_{2N}(-s) = \det(\mathbf{M}s^2 - \mathbf{G}s + \mathbf{K})^T = \det(\mathbf{M}s^2 + \mathbf{G}s + \mathbf{K}) = p_{2N}(s). \tag{3.52}$$

This implies that if s is a root, then $-s$ is also a root, ruling out asymptotic stability since if one root is in the LHP, another must be in the right half-plane (RHP). Consequently, all roots must lie on the imaginary axis in the form $s = j\omega$ for stability. An example of a simple system is:

$$\dot{x}_1 - gx_2 + k_1x_1 = 0 \tag{3.53}$$

$$\dot{x}_2 + gx_1 + k_2x_2 = 0 \tag{3.54}$$

The characteristic equation is given by:

$$s^4 + (k_1 + k_2 + g^2)s^2 + k_1k_2 = 0. \tag{3.55}$$

The roots of Eq. (3.55) can be easily obtained by transforming the characteristic equation into:

$$s^4 + b_1s^2 + b_2 = 0. \tag{3.56}$$

The necessary and sufficient conditions for the s^2-roots to lie on the LHP are:

$$b_1 > 0, \tag{3.57}$$

$$b_2 > 0, \tag{3.58}$$

$$b_1^2 - 4b_2 > 0. \tag{3.59}$$

Writing for the Eq. (3.55) system it follows

$$k_1 + k_2 + g^2 > 0, \tag{3.60}$$

$$k_1k_2 > 0, \tag{3.61}$$

$$\Xi \triangleq (k_1 - k_2)^2 + 2g^2(k_1 + k_2) + g^4 > 0. \tag{3.62}$$

Notice that all conditions where k_1 and k_2 have opposite signs will lead to instability. Also, cases where $k_1 + k_2 < -g^2$ the system is unstable. The most interesting condition is Eq. (3.62), which translates into a parabolic function with boundary values at $(-g^2, 0)$ and $(0, -g^2)$ defined by Eq. (3.60). Any case where function $\Xi = 0$ is unstable. However, cases where the system attends Eq. (3.62) condition, although statically unstable, are stabilized by the gyric forces. Thus, even some statically unstable conservative systems can be gyrically stabilized with a sufficiently large g.

3.3.3.3 Effect of Damping Conservative Gyric Systems

The previous discussion has demonstrated that, while a gyric term cannot destabilize a stable conservative system, it can often stabilize an unstable one. Adding energy dissipation, however, can have mixed effects — sometimes beneficial, sometimes detrimental. Specifically, damping generally transforms statically stable systems into asymptotically stable ones, but it can also render gyrically stabilized, statically unstable systems unstable (HUGHES, 2004). A more profound discussion is made in (HUGHES, 2004), however in this work we will stay only with the stated consideration.

3.4 GRAVITY-GRADIENT STABILITY MAP

With the linearized system's state matrix, Eq. (3.36), we start to analyze the stability of the motion and characterize the GGSM. As we can see in Eq. (3.36) the pitch motion is decoupled from the roll/yaw motion. Therefore, the pitch model becomes:

$$\begin{bmatrix} d\ddot{\theta} \\ d\dot{\theta} \end{bmatrix} = \begin{bmatrix} 0 & -3\eta^2\kappa_2 \\ 1 & 0 \end{bmatrix} \begin{bmatrix} d\dot{\theta} \\ d\theta \end{bmatrix}. \tag{3.63}$$

The characteristic equation is:

$$s^2 + 3\eta^2\kappa_2 = 0, \tag{3.64}$$

characterized as a conservative system. Given Theorem 3.3.4 and Theorem 3.3.5, the stable solution of Eq. (3.64) is attended under the following condition:

$$\kappa_2 > 0 \longrightarrow J_1 > J_3. \tag{3.65}$$

Notice that, from Theorem 3.3.1, the pitch motion is only L-stable since Eq. (3.64) gives us a pure imaginary solution, $\max\{\sigma_i\} = 0$. The pitch motion of a rigid body under only GG torque is purely oscillatory and within a limited bound. Eq. (3.65) can also be translated in terms of the inertia ratios κ_1 and κ_3 as follows

$$\kappa_1 > \kappa_3. \tag{3.66}$$

The condition in Eq. (3.66) characterizes the Pitch stable region on the GGSM, represented in Figure 3.1.

Now, analyzing the stability of roll/yaw motion, the coupled motion is rewritten as:

$$\begin{bmatrix} d\ddot{\psi} \\ d\ddot{\phi} \\ d\dot{\psi} \\ d\dot{\phi} \end{bmatrix} = \begin{bmatrix} 0 & \eta - \eta\kappa_1 & -4\eta^2\kappa_1 & 0 \\ -\eta + \eta\kappa_3 & 0 & 0 & -\eta^2\kappa_3 \\ 1 & 0 & 0 & 0 \\ 0 & 1 & 0 & 0 \end{bmatrix} \begin{bmatrix} d\dot{\psi} \\ d\dot{\phi} \\ d\psi \\ d\phi \end{bmatrix}. \tag{3.67}$$

The characteristic equation of Eq. (3.67) is:

$$s^4 + (1 + 3\kappa_1 + \kappa_1\kappa_3)\eta^2 s^2 + 4\kappa_1\kappa_3\eta^4 = 0. \tag{3.68}$$

Analyzing Eq. (3.68), the system is characterized as a conservative gyric system. Therefore, the roots have symmetry about the imaginary axis, as explained in Subsection 3.3.3.2. This demonstrates that the Theorem 3.3.2 will not be attended. Therefore, for L-stability in the roll/yaw motion, the roots must also be purely imaginary, according to Theorem 3.3.1. This is equivalent to requiring that the s^2-roots be located in the LHP.

In addition, using the Theorem 3.3.4, necessary conditions for the system to be L-stable is:

$$(1 + 3\kappa_1 + \kappa_1\kappa_3) > 0, \tag{3.69}$$

$$\kappa_1\kappa_3 > 0. \tag{3.70}$$

A sufficient condition (HUGHES, 2004; MARKLEY; CRASSIDIS, 2014) for the L-stable motion in roll/yaw is:

$$\kappa_1 > 0 \longrightarrow J_2 > J_3, \tag{3.71}$$

$$\kappa_3 > 0 \longrightarrow J_2 > J_1. \tag{3.72}$$

The Eqs. (3.71) and (3.72) represent the Roll-Yaw stable region on the GGSM. Combined with the pitch L-stable condition we have that:

$$\kappa_1 > \kappa_3 > 0 \longrightarrow J_2 > J_1 > J_3, \tag{3.73}$$

This condition is sufficient for defining the L-stability, known as the Lagrange region on the GGSM. In this region, we have the L-stability of the three axes - Roll, Pitch, and Yaw. The necessary and sufficient conditions for Lyapunov stability in the roll/yaw motion are:

$$\kappa_1\kappa_3 > 0, \tag{3.74}$$

$$1 + 3\kappa_1 + \kappa_1\kappa_3 > 4\sqrt{\kappa_1\kappa_3}. \tag{3.75}$$

For the case where κ_1 and κ_3 are both negative and condition in Eq. (3.75) is attended, the body configuration respects the relation $J_2 < J_3 < J_1$, and is located in the Debra-Delp (DD) region (HUGHES, 2004; MARKLEY; CRASSIDIS, 2014). This region is defined for $-1 < \kappa_3 < 0$ and the maximum valeu of κ_1 can be obtained rewritten Eq. (3.75) as shown in the equation below:

$$f_{\mathrm{DD}}(\kappa_3) = \kappa_1 = \frac{7\kappa_3 - 3 + 4\sqrt{3\kappa_3(\kappa_3 - 1)}}{(3 + \kappa_3)^2}, \quad -1 < \kappa_3 < 0. \tag{3.76}$$

The DD region is also a three-axis stable region, however, the system is statically unstable and gyrically stabilized. Thus, as cited previously, the minimum damping in either roll or yaw will generate instability. However, the pitch motion will remain stable.

Figure 3.1 is the Gravity-Gradient Stability Map and represents all the stability regions discussed in the present section.

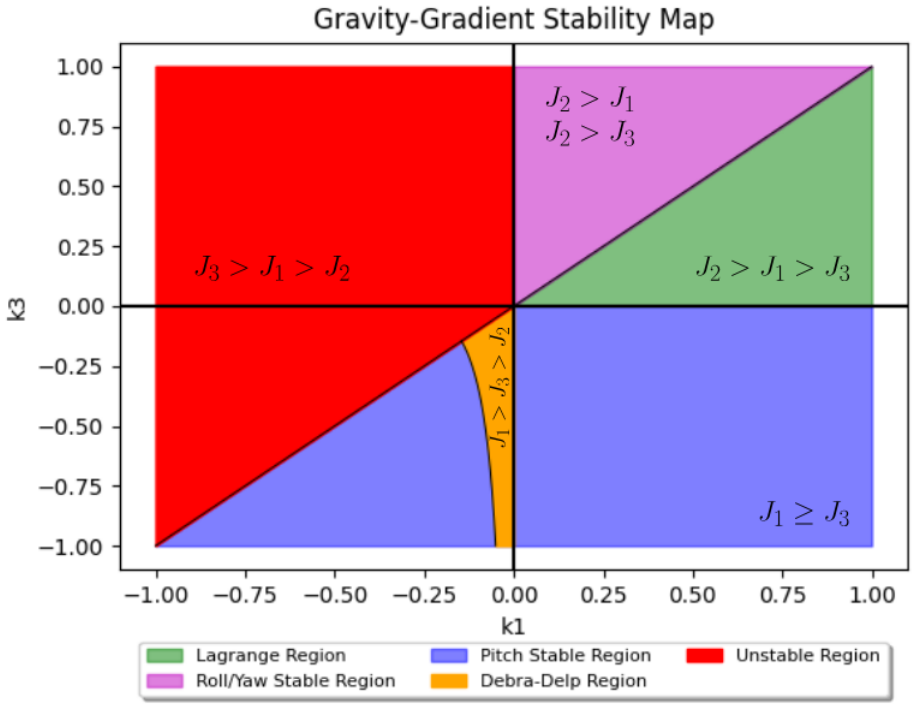

Figure 3.1. Gravity-Gradient Stability Map with the Principal moments of inertia relations for each region.

When the body configuration is located in the Lagrange region, it is a Lyapunov attitude stable satellite. Its minor axis is vertical and its major axis is normal to the orbital in a LVLH frame. When it is located in the Debra-Delp region, its minor axis is normal to the orbit and its major axis is tangential to the orbit, and this is a stable equilibrium only in the absence of dissipation (HUGHES, 2004). Moreover, we notice that when considering only GG torque, the

principal moments of inertia are the variables that define the motion stability. At the same time, η plays the role of the motion's time characteristic.

CHAPTER 4

METHODOLOGY

This chapter consists of the work's methodology, describing the rigid body model and dynamic equations implemented, the rotational kinetic energy patterns analysis, the proposed empirical models for stability indices, and how to use them to improve the mechanical design using a dummy mass. It also contains a description of the control system, alongside performance metrics that will be presented and compared in Chapter 5. The implementation of this work is entirely Python-based, object-oriented, and utilizes Git as a version control tool.

4.1 IMPLEMENTATION OF THE RIGID BODY MODEL

The scope of this case study is defined according to the CubeSat standard, making it the rigid body model to be analyzed. The 14.1 Revision of the CubeSat Design Specifications (CDS) (JOHNSTONE, 2022) defines tolerances for the location of the design's CG in the mechanical project. The Table 4.1 presents the deviations from the geometric center in each mechanical design axis the standard allows.

Table 4.1. CDS for mass and tolerances for the CG position from the geometric center. Source: (JOHNSTONE, 2022)

Sizes	**Mass** [kg]	**Dimensions** [mm]			**Tolerances** [mm]		
		x-axis	**y-axis**	**z-axis**	**x-axis**	**y-axis**	**z-axis**
1U	2	100	100	113	±20	±20	±20
1.5U	3	100	100	170.2	±20	±20	±30
2U	4	100	100	227	±20	±20	±45
3U	6	100	100	340.5	±20	±20	±70
6U	12	226.3	100	366	±45	±20	±70
12U	24	226.3	226.3	366	±45	±45	±70

Figure 4.1 shows a scheme of a 1U CubeSat with its cube of tolerance for the CG localization. Consider the point P as the coordinates of the center of gravity (CG). Therefore, P can position itself anywhere within the purple cube to fulfill the CDS.

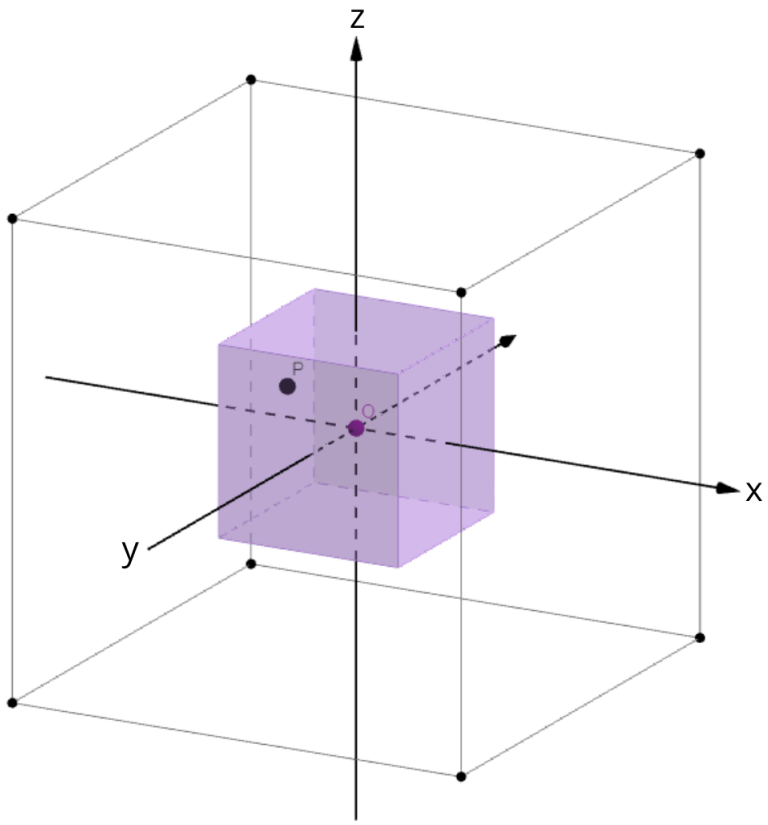

Figure 4.1. Illustration of the tolerance cube for the CG position in 1U CubeSat.

The rigid body sample is designed as an instance of the CubeSat class, which is initialized with a specified size (ranging from 1U to 12U) and the number of subsystems it contains. The CubeSat class includes a method that creates Subsystem objects, representing the various subsystems within the CubeSat. The collection of these subsystems forms what we call the configuration, which defines the overall assembly of the CubeSat. Based on this assembly, all other attributes of the CubeSat are subsequently calculated. Figure 4.2 shows the implementation of the generation of a CubeSat sample. Now, we describe each class used in the process.

4.1.1 Class Subsystem

The `Subsystem` class represents a simplified model of actual CubeSat subsystems, such as batteries, onboard computers, solar arrays, attitude control actuators, payloads, and more. Each subsystem is modeled as a mass point, with properties like mass and coordinates that can either be randomly generated or specified by the user. In this work, the set of Subsystems is commonly referred to as the CubeSat configuration.

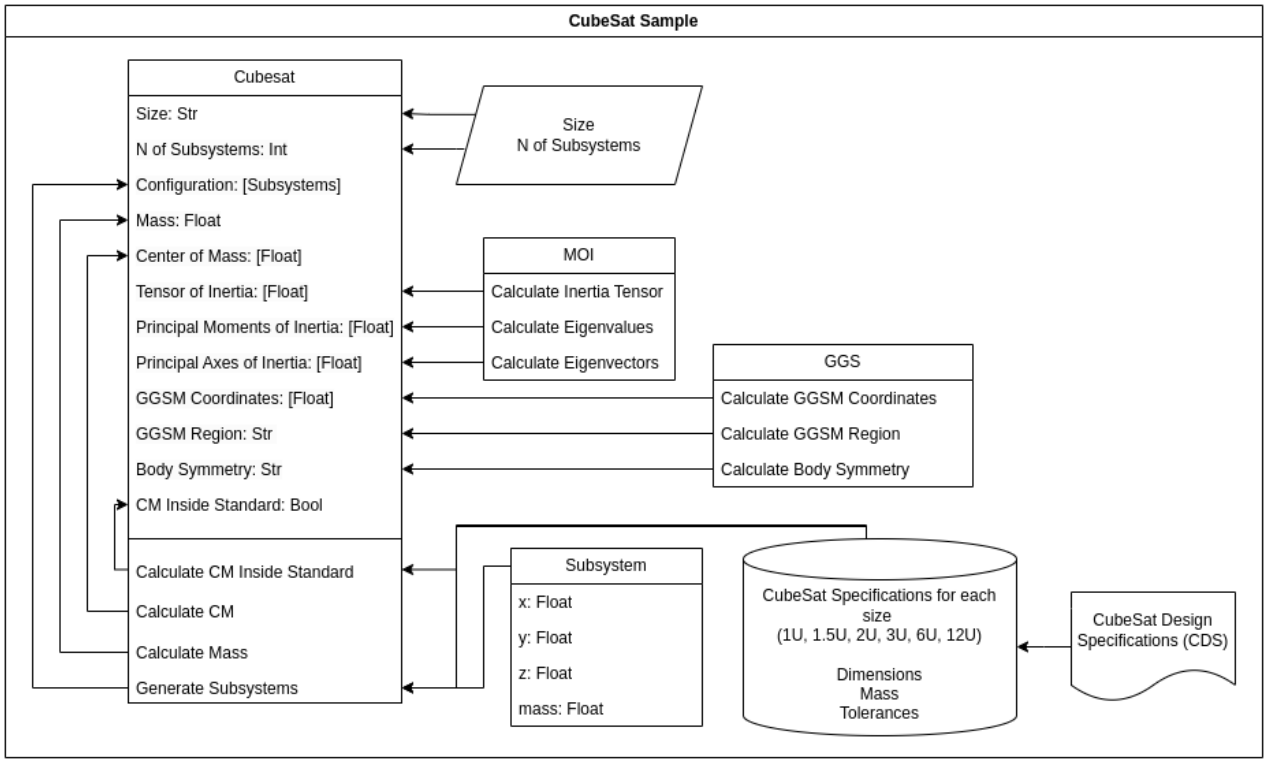

Figure 4.2. Class Diagram of Key Components for CubeSat Sample Implementation.

4.1.2 Class CubeSat

The `CubeSat` class is an abstraction of a real Cubesat, where the main attributes of a CubeSat relevant to the analysis were implemented, shown in Table 4.2.

Table 4.2. Attributes of the `CubeSat` Class

Attribute	Type	Description
`size`	str	The size of the CubeSat. Possible values: 1U, 1.5U, 2U, 3U, 6U, 12U.
`nOfSubsystems`	`int`	Number of subsystems in the CubeSat.
`configuration`	`list[Subsystems]`	Objects Subsystem within the CubeSat.
`mass`	`float`	Total mass of the CubeSat.
`centerOfMass`	`numpy.ndarray`	Coordinates of the CubeSat's CM.
`momentsOfInertia`	`numpy.ndarray`	Principal moments of inertia (J) for the CubeSat.
`axisOfInertia`	`numpy.ndarray`	Principal axes of inertia of the CubeSat.
`tensorOfInertia`	`numpy.ndarray`	Inertia tensor matrix for the CubeSat.
`ggsMapCoordinates`	`numpy.ndarray`	GGSM coordinates of the CubeSat.
`stabilityRegion`	`str`	GGSM region of the CubeSat. Possible values: Lagrange, Debra-Delp, Pitch, Roll-Yaw, Unstable.
`bodySymmetry`	`str`	Symmetry type of the CubeSat's body. Possible values: Axisymmetric or Triaxial.
`cmInsideStd`	`bool`	Indicates whether the CM is within the CDS limits.

The `CubeSat` class is initialized with the attribute `size`, which represents the standardized size and form factor (in units of U, ranging from 1U to 12U) as specified in (JOHNSTONE,

2022). It also receives the attribute `nOfSubsystems`, defining the number of subsystems the user intends for the CubeSat. With these two attributes, the implementation can either randomly generate or accept a predefined set of `Subsystem` objects to form the CubeSat's configuration. The random generation respects the mass and dimension constraints for the selected CubeSat size, consulting a database based on Table 4.1.

Once the configuration is defined, the feature calculation process begins. First, the total mass of the system is calculated as the sum of the masses of all subsystems. Next, the CM is calculated. It's important to note that since the actual mechanical design is assembled and tested on Earth, we assume the CG and CM coincide. This assumption aligns with (JOHNSTONE, 2022), which uses CG terminology, and is pertinent because this work focuses on how the CDS tolerances allow configurations to fall into different stability regions on the Gravity-Gradient Stability Map (GGSM).

Following this, the inertia features are calculated using the `MOI` class. First, Eqs. (2.28) to (2.33) are applied to compute the inertia tensor. Then, the `eig` function from the `numpy.linalg` library (NUMPY DEVELOPERS, 2024) is used to determine the eigenvalues and eigenvectors of the MOI tensor. These results are assigned to their respective attributes, as illustrated in Figure 4.2.

With the inertia features established, the implementation proceeds to calculate the GGS characteristics. This begins with computing the GGSM coordinates using Eqs. (3.37) and (3.39). The coordinates (κ_1, κ_3) are then used to identify the GGSM stability region of the configuration, as shown in Figure 3.1, indicating the CubeSat's stability. Next, the body symmetry of the CubeSat is determined, with possible values listed in Table 4.2. At last, the code verifies whether the generated sample's CM complies wit the CDS tolerance requirements, checking the database once more.

4.2 IMPLEMENTATION OF THE ATTITUDE MOTION

The implementation of the attitude dynamics was also based on a class abstraction of the motion, the simulation of the attitude contains several classes involved. However, the main classes involved on the implementation of the attitude motion were `AttitudeDynamics` and

`Orbit`, shown in Figure 4.3. Those classes contain the main attributes and methods responsible for propagating the motion.

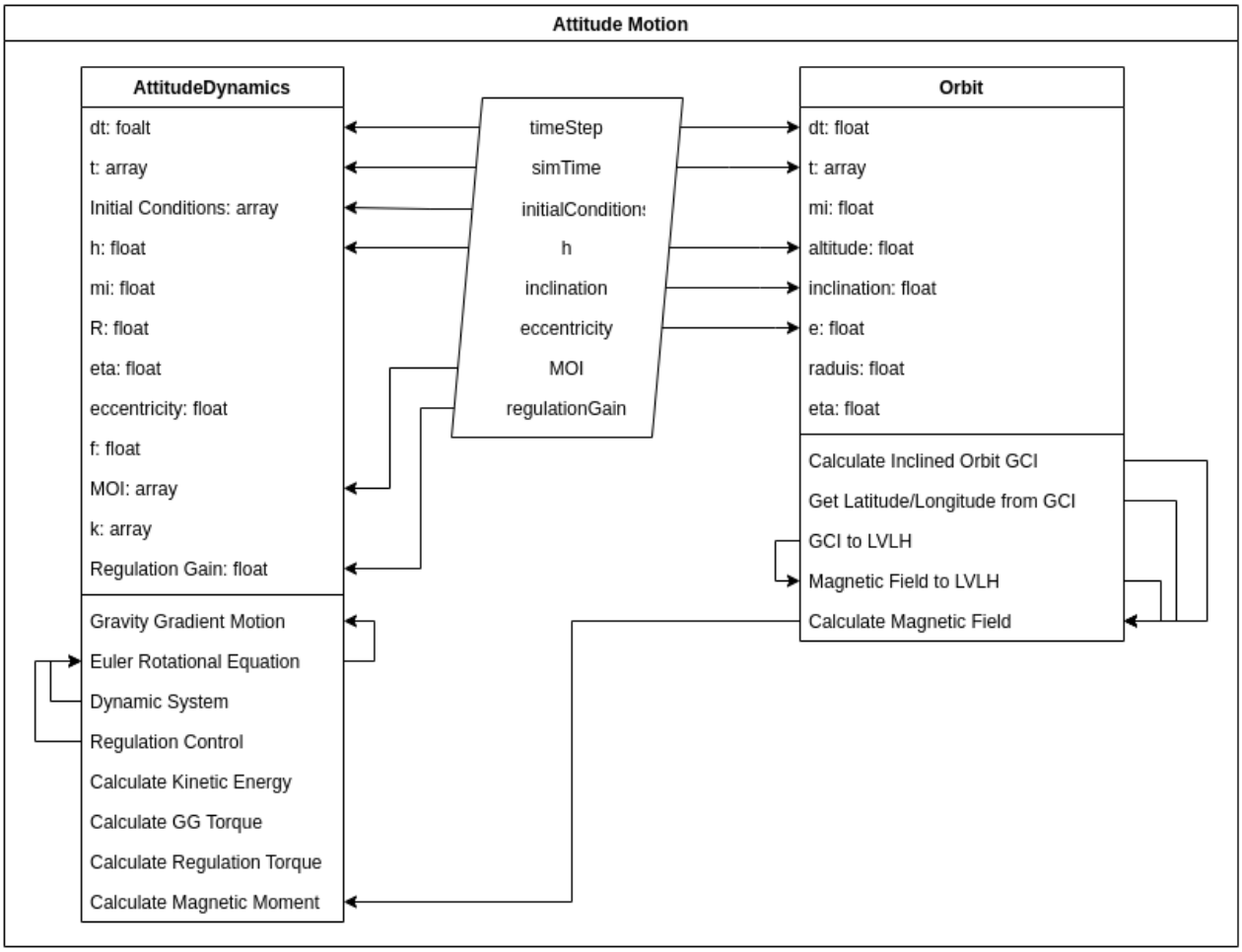

Figure 4.3. Class Diagram of Key Components for Attitude Motion Implementation

4.2.1 Class AttitudeDynamics

The `AttitudeDynamics` class is the abstraction of the attitude of the rigid body in space, and it is responsible for all the calculations concerning the attitude motion. It uses parameters such as principal moments of inertia, gravitational constants, and control gains to calculate various dynamic properties, including rotational kinematics, control torque, and energy functions. Key operations include the calculation of the Euler rotational equation, dynamic system matrix, and control inputs for stabilization and regulation of attitude.

This class includes several primary methods for analyzing attitude motion. First, the `Euler Rotational Equation` method implements Euler's rotational equation, as defined in

Table 4.3. Attributes of the `AttitudeDynamics` Class.

Attribute	Type	Description
`dt`	`float`	The simulation time step, in seconds.
`t`	`numpy.ndarray`	Array of time values from 0 to the specified total simulation time.
`MOI`	`numpy.ndarray`	Principal moments of inertia (J) of the rigid body.
`mi`	`float`	Gravitational parameter (μ).
`h`	`float`	Satellite altitude in meters.
`R`	`float`	Radius of the Earth in meters.
`eta`	`float`	Mean motion of the orbit (η).
`eccentricity`	`float`	Orbital eccentricity (e).
`f`	`float`	True anomaly (f) in radians.
`regulationGain`	`float`	Gain for the control law.
`k`	`list[float]`	Body inertia ratios ($\kappa_1, \kappa_2, \kappa_3$)

Eq. (2.39). This method utilizes the `Dynamic System` and `Regulation Control` methods to compose Eq. (2.39). It operates with or without regulation control, the latter occurring when `regulationGain` is set to zero. The `Dynamic System` method provides the system's state matrix, Eq. (3.36), which incorporates the effects of gravity-gradient (GG) torque. The `Regulation Control` method implements the control law, Eq. (4.6), which will be discussed further in this chapter.

The `Gravity Gradient Motion` method integrates the `Euler Rotational Equation` over time using Python's `scipy.integrate` solver `odeint` (THE SCIPY COMMUNITY., 2024), which offers accuracy comparable to the 4th-order Runge-Kutta method with faster computational performance (MIYAMOTO *et al.*, 2023).

Additional but essential methods for attitude dynamics analysis include `Calculate Kinetic Energy`, `Calculate GG Torque`, `Calculate Regulation Torque`, and `Calculate Magnetic Moment`, each of which is self-explanatory by name. All these methods use the solution from `Gravity Gradient Motion` to do their respective calculations.

4.2.2 Class Orbit

The class `Orbit` is an auxiliary class, mainly to calculate the geomagnetic field vector in a certain orbit. Its main use is to provide the geomagnetic field to calculate the magnetic moment generated by the magnetorquer, Eq. (2.54). Its attributes are specified in Table 4.4.

The `Orbit` class is initialized with the following inputs: orbit altitude, inclination, and eccentricity. The `Calculate Inclined Orbit GCI` method computes the position and veloc-

Table 4.4. Attributes of the `Orbit` Class

Attribute	Type	Description
`dt`	`float`	The simulation time step, in seconds.
`t`	`numpy.ndarray`	Array of time values from 0 to the specified total simulation time.
`altitude`	`float`	Satellite altitude in meters.
`inclination`	`float`	Orbit's inclination in radians.
`e`	`float`	Orbital eccentricity (e).
`radius`	`float`	Orbit's radius ($r = R + h$).
`mi`	`float`	Gravitational parameter (μ).
`eta`	`float`	Orbit's mean motion (η).
`wEarth`	`float`	Earth's rotation.

ity vectors in the Geocentric Inertial (GCI) frame at each time step of the orbit simulation. Next, the `Get Latitude/Longitude from GCI` method takes the position vector array and extracts latitude and longitude values. This enables the calculation of the geomagnetic field vector, which is performed using the International Geomagnetic Reference Field (IGRF) model, specifically implemented in Python as pyIGRF (PYTHON SOFTWARE FOUNDATION, 2024).

The IGRF is a set of mathematical models describing the Earth's large-scale internal magnetic field (ALKEN *et al.*, 2021b; ALKEN *et al.*, 2021a). The pyIGRF library calculates the magnetic field's intensity and performs coordinate transformations between Geographical and Geomagnetic frames (PYTHON SOFTWARE FOUNDATION, 2024). The geomagnetic field intensity vector is initially given in North-East-Down (NED) coordinates, which is then converted to GCI coordinates and subsequently to Local Vertical Local Horizontal (LVLH) coordinates, representing the body frame, using the `GCI to LVLH` method.

4.3 CONTROL LAW

For the control law, the classical regulation problem is chosen. The regulation problem is a typical feedback control system that regulates the attitude and angular velocity vectors to zero (MARKLEY; CRASSIDIS, 2014; NISE, 2015; MIYAMOTO *et al.*, 2023; CHAURAIS *et al.*, 2015; HORRI; PALMER, 2012). Knowing that the system is linearized - Eq. (3.35) - around the relative equilibrium condition, Eq. (3.40), then

$$\delta\mathbf{x} = \mathbf{x}. \tag{4.1}$$

Therefore, the regulation control law is given by (NISE, 2015):

$$\dot{\mathbf{x}} = \mathbf{A}\mathbf{x} + \mathbf{C}\mathbf{u} \tag{4.2}$$

$$\dot{\mathbf{x}} = \mathbf{A}\mathbf{x} + \mathbf{C}(\mathbf{r} - \mathbf{K}\mathbf{x}), \tag{4.3}$$

where $\mathbf{K}$ is the feedback gain vector, $\mathbf{C}$ is the control matrix, $\mathbf{u} = -\mathbf{K}\mathbf{x}$ is the control vector, and $\mathbf{r}$ is the reference vector. In the regulation control case, the reference $\mathbf{r}$ is set to zero leading Eq. (4.3) to

$$\dot{\mathbf{x}} = \mathbf{A}\mathbf{x} - \mathbf{C}\mathbf{K}\mathbf{x}. \tag{4.4}$$

As the goal of this section is not to propose an optimal state feedback controller, but rather to compare different configurations submitted to a stabilizing controller, a constant gain empirically adjusted is used for all state variables, that is

$$\mathbf{K} = -(k\mathbf{I})\mathbf{x}. \tag{4.5}$$

The control gains used in each CubeSat size are specified in Table 4.7. The control matrix $\mathbf{C}$ is given by

$$\mathbf{C} = \begin{bmatrix} J_1^{-1} & 0 & 0 & J_1^{-1} & 0 & 0 \\ 0 & J_2^{-1} & 0 & 0 & J_2^{-1} & 0 \\ 0 & 0 & J_3^{-1} & 0 & 0 & J_3^{-1} \end{bmatrix}. \tag{4.6}$$

Thus, the control law is:

$$\mathbf{C}\mathbf{u} = -\mathbf{C}\mathbf{K}\mathbf{x}, \tag{4.7}$$

The control law is the same for both actuators models, although the control torques differ in nature, since the magnetic torque is an external torque while the reaction wheels produce an internal torque. The following equations indicate the control torques are calculated for each case, recalling Eqs. (2.53) and (2.58):

$$\mathbf{J}_B^c\mathbf{C}\mathbf{K}\mathbf{x} = \mathbf{L}_B^{\text{mag}} = \mathbf{m} \times \mathbf{B}, \tag{4.8}$$

$$\mathbf{J}_B^c\mathbf{C}\mathbf{K}\mathbf{x} = -\mathbf{L}_{\text{eff}}^w = \mathbf{L}_B^w + \boldsymbol{\omega}_B^{BI} \times \mathbf{H}_B^w. \tag{4.9}$$

Additionally, the control efforts also differ for the magnetorquer, which is the produced magnetic moment:

$$\mathbf{m} = (\mathbf{B} \times \mathbf{J}_B^c\mathbf{C}\mathbf{K}\mathbf{x})/B^2. \tag{4.10}$$

For the reaction wheels, the angular momentum is the control effort metric, which is obtained by integrating the following:

$$\mathbf{L}_B^w = \dot{\mathbf{H}}_B^w = \mathbf{C}\mathbf{K}\mathbf{x} - \boldsymbol{\omega}_B^{BI} \times \mathbf{H}_B^w. \tag{4.11}$$

4.3.1 Performance metrics

Performance metrics related to the attitude motion and control dynamics are defined to present the performance analysis of the control system in Chapter 5. For clarity, this Subsection is dedicated to explain and define these metrics. To calculate the peak-to-peak values of the metrics the following equation is used:

$$\Delta y = y_{\max} - y_{\min}. \tag{4.12}$$

To analyze the peak values of the control efforts, the maximum value is:

$$y_{\text{peak}} = \max(y_{\max}, \text{abs}(y_{\min})). \tag{4.13}$$

The percent decrease for all metrics is defined by:

$$y_{\%} = \frac{y_{\text{HARKE}} - y_{\text{LARKE}}}{y_{\text{HARKE}}}, \tag{4.14}$$

where the subscript y_{HARKE} represents the CubeSat configurations with Higher Average Rotational Kinetic Energy (HARKE), and the subscript y_{LARKE} represents the CubeSat configurations with Lower Average Rotational Kinetic Energy (LARKE). Therefore, if the resulting values from Eq. (4.14) are positive means a decrease, and if the values are negative indicates an increase, about the reference y_{HARKE}. The following list explains all the metrics to be analyzed in the Results chapter:

- **Peak-to-Peak Attitude Motion**: the Euler angle presenting the largest peak-to-peak value. We calculate the peak-to-peak value of each Euler angle, using Eq. (4.12), and select the largest one.

- **Peak-to-Peak Angular Velocity**: the angular velocity component presenting the largest peak-to-peak value. We calculate the peak-to-peak value of each component of the angular velocity vector, using Eq. (4.12), and select the largest one.

- **Peak-to-Peak Control Torque**: the control torque component presenting the largest peak-to-peak value. We calculate the peak-to-peak value of each component of the applied control torque, using Eq. (4.12), and select the largest one.

- **Peak-to-Peak Reaction Wheel Angular Momentum**: the reaction wheel angular momentum presenting the largest peak-to-peak value. We calculate the peak-to-peak **h** value generated by each axis wheel, using Eq. (4.12), and select the largest one.

- **Peak-to-Peak Magnetorquer Magnetic Moment**: the magnetorquer magnetic moment presenting the largest peak-to-peak value. We calculate the peak-to-peak value of the generated **m** by the magnetorquer in each axis, using Eq. (4.12), and select the largest one.

- **Transient Period**: the instant t where the transient regime finishes, the steady state criteria is $y < 10^{-5}$.

- **Mean Control Torque**: the average of the control torque vector's norm, during the simulation.

- **Maximum Reaction Wheel Angular Momentum**: the maximum control efforts produced by the reaction wheels. We calculate the maximum $\mathbf{H}_B^w$ of each wheel, using Eq. (4.13), and select the largest one.

- **Maximum Magnetorquer Magnetic Moment**: the maximum control efforts produced by the magnetorquer. We calculate the maximum **m** of each magnetorquer, using Eq. (4.13), and select the largest one.

- **Average Kinetic Rotational Energy in Closed-Loop**: the average of the Lyapunov candidate function, Eq. (4.16), during the closed-loop simulation.

4.4 EMPIRICAL MODELS OF STABILITY INDICES BASED ON ARKE

Set a direct relation of the GG stability with the mechanical design parameters for instance, mass distribution, CM location, MOI or even the inertia ratios κ_1 and κ_3 is a challenging analysis. However, proposing an index that relates any of the parameters mentioned previously with the GGS, in order to incorporate the GGS into the mechanical project to enhance its attitude stability performance was the primary goal of this study. To do so, it was imperative to set a validation metric for the proposed index. In this matter, a natural candidate of Lyapunov

Function are energy functions. For this work, we chose the rotational kinetic energy (RKE) to be the stability validation metric. The RKE was calculated using the following (MARKLEY; CRASSIDIS, 2014):

$$2E_K = \boldsymbol{\omega}^T \mathbf{J} \boldsymbol{\omega} = \omega_1^2 J_1 + \omega_2^2 J_2 + \omega_3^2 J_3. \tag{4.15}$$

In this section, we propose three empirical models for stability indices: the stability map margin, the trace of the inertia matrix and the sum of the roots' norms. The quality metric of the indices is the Average Rotational Kinetic Energy (ARKE), calculated as the arithmetic mean of the RKE:

$$ARKE = \left(\sum_{t=0}^{T} E_K(t) \right) /T. \tag{4.16}$$

Further in Subsections 4.4.1, 4.4.2 and 4.4.3, the stability indices are formulated and justified.

4.4.1 Stability Map Margin - SMM

The concept of stability margin refers to the maximum allowable excursion of one or more parameters describing a control system while maintaining its stability condition. Commonly used margins in classical control design include gain, phase, modulus, and delay margins (NISE, 2015; EUROPEAN COOPERATION FOR SPACE STANDARDIZATION, 2010). The Stability Map Margin (SMM) was proposed empirically based on this concept to investigate differences between the dynamic and kinematic behavior of points within the GGSM, and next classify those points.

Through the ARKE simulation, Figure 4.20, for each CubeSat size, we generated heatmaps of the ARKE for each region of the stability map, Figure 3.1. Using these heatmaps, we analyzed the ARKE distribution patterns to develop an empirical model of attitude stability based on the GGSM. Therefore, based on the identified patterns, we proposed formulas for the SMM empirical model.

The SMM is defined as the distance between the coordinates (κ_1, κ_3), representing the inertia ratios of a given configuration, and the nearest boundary that demarcates the transition from one GGSM stability region to another. Now, we pass through each GGSM region and explain the proposed formula for the SMM.

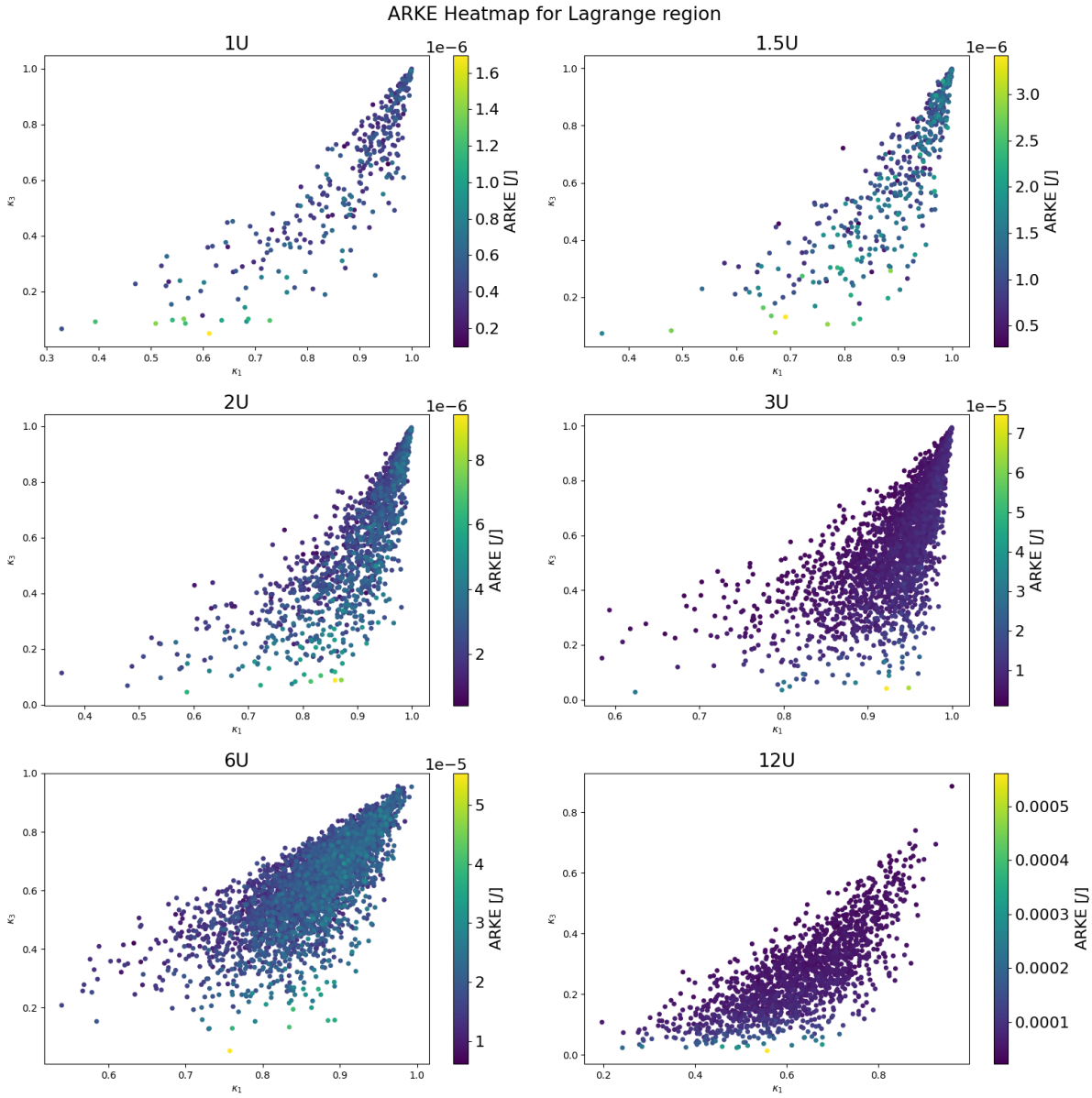

Figure 4.4. GGSM-ARKE Heatmap of the 1U-12U configurations with Lagrange stability.

A relatively uniform ARKE distribution is observed in Figure 4.4. Nonetheless, higher ARKE points are predominantly located closer to the Pitch stable region, $\kappa_1 \leq 0$. This pattern is even more explicit in sizes 2U and 12U. Therefore, the SMM formula for Lagrange configurations was defined as the vertical distance from the point to the pitch boundary, $\kappa_3 = 0$:

$$SMM_{\text{Lagrange}} = \kappa_3. \tag{4.17}$$

In Figure 4.5, which corresponds to the GGSM Debra-Delp region, we observe that the concentration of higher energy points is also near to the Debra-Delp curve, which is the boundary with the Pitch stable region. Therefore, the algorithm calculates the distance from the point

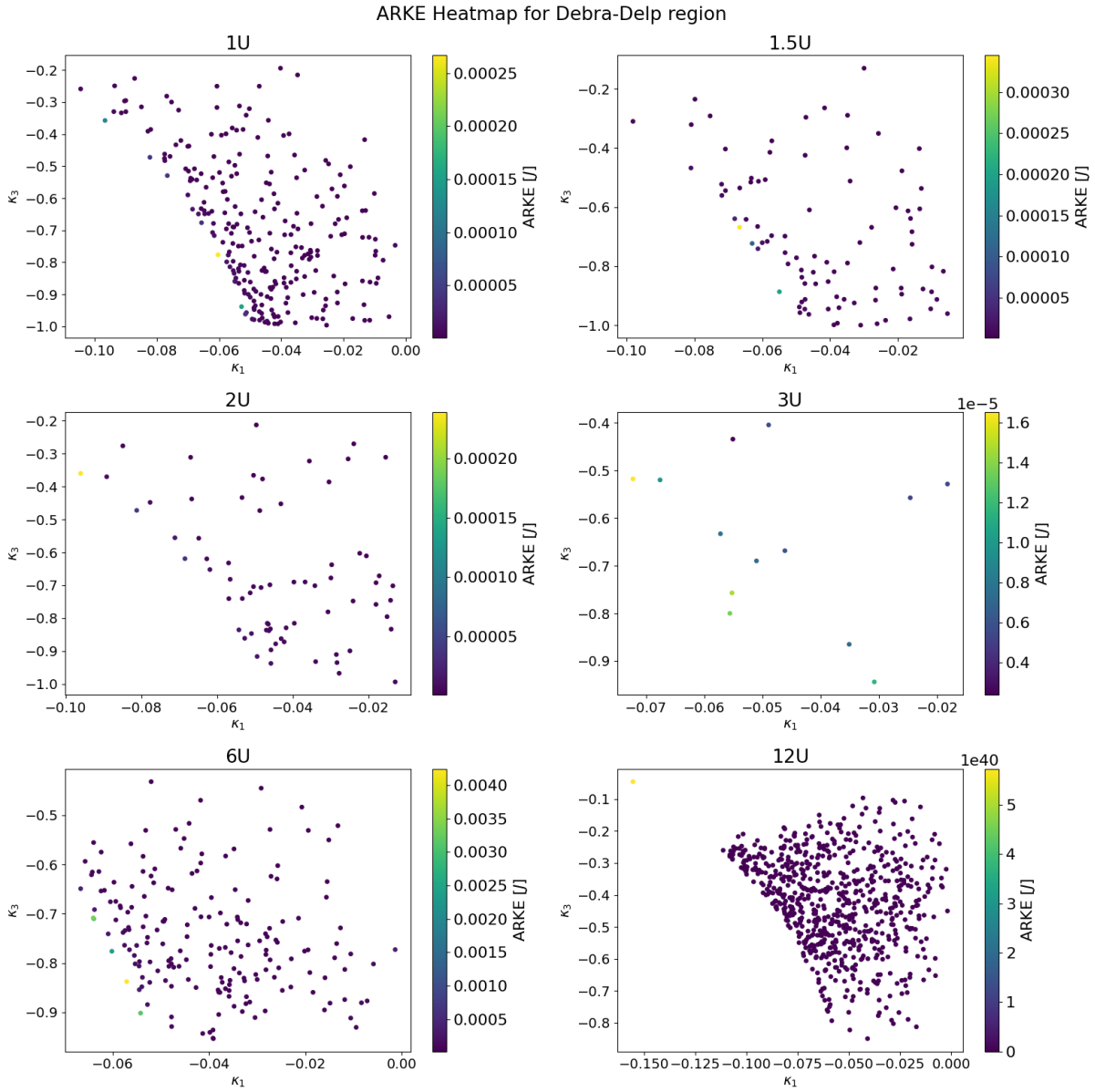

Figure 4.5. GGSM-ARKE Heatmap of the 1U-12U configurations with Debra-Delp stability.

(κ_1, κ_3) to the Debra-Delp curve, given by Eq. (3.76), using the `minimize_scalar` function from `scipy.optimize` (THE SCIPY COMMUNITY., 2024):

$$SMM_{\text{DD}} = d(f_{\text{DD}}(\kappa_3) - p), \quad p = (\kappa_1, \kappa_3). \tag{4.18}$$

For the Pitch stable region, Figure 4.6, higher energy points are concentrated in the lower right and left corners of the stability map, prompting the definition of the SMM as:

$$SMM_{\text{Pitch}} = abs(\kappa_1) + abs(\kappa_3). \tag{4.19}$$

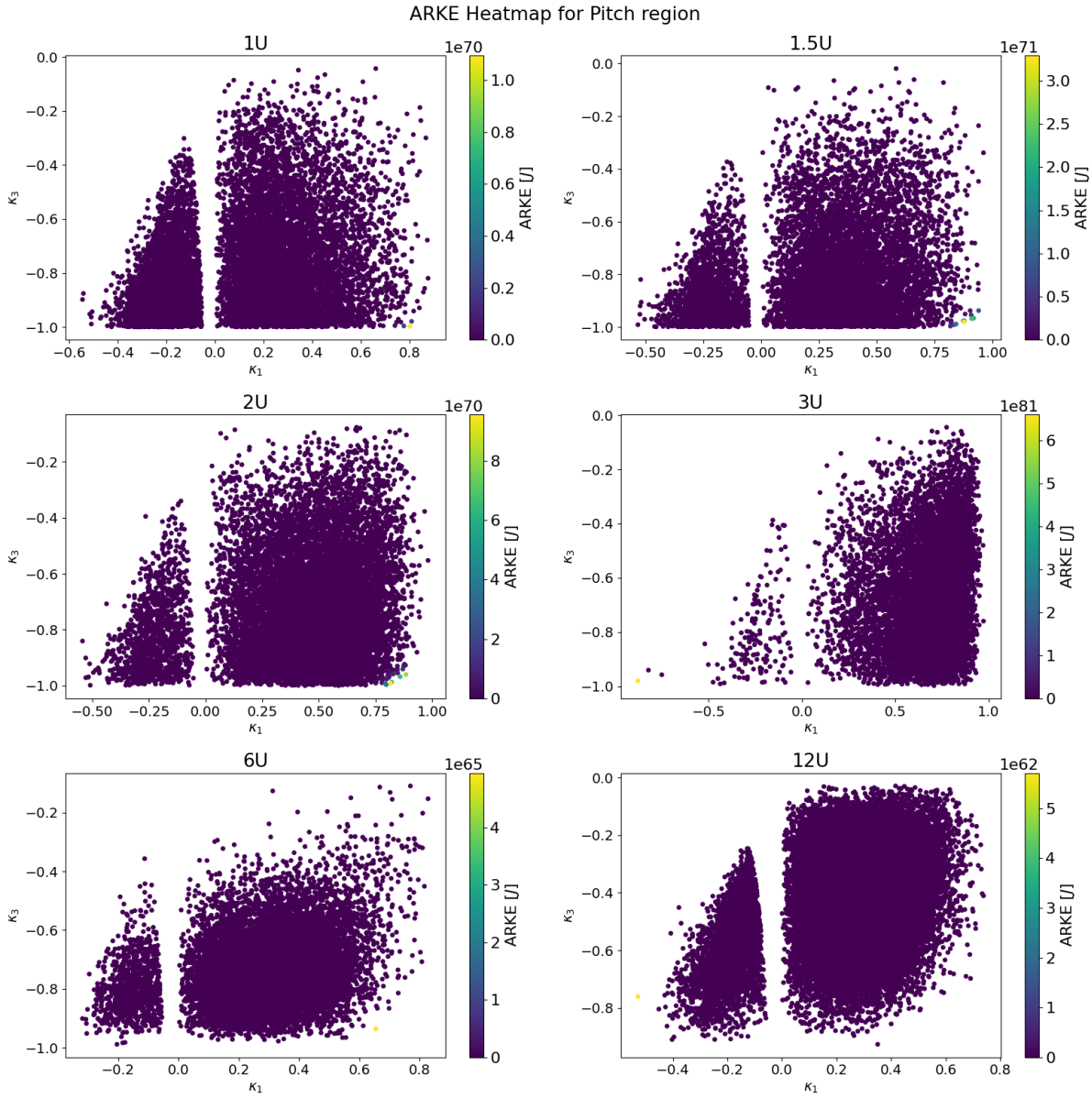

Figure 4.6. GGSM-ARKE Heatmap of the 1U-12U configurations with Pitch stability.

In Figure 4.7, representing the Roll-Yaw stable region, the higher energy points are mostly concentrated in the upper corner of the stability map, leading to the formulation of the SMM as:

$$SMM_{Roll-Yaw} = \kappa_3. \tag{4.20}$$

Lastly, in the Unstable region, Figure 4.8, the higher energy points are concentrated in the upper left corner of the stability map, resulting in the SMM being defined as:

$$SMM_{Unstable} = abs(\kappa_1) + \kappa_3. \tag{4.21}$$

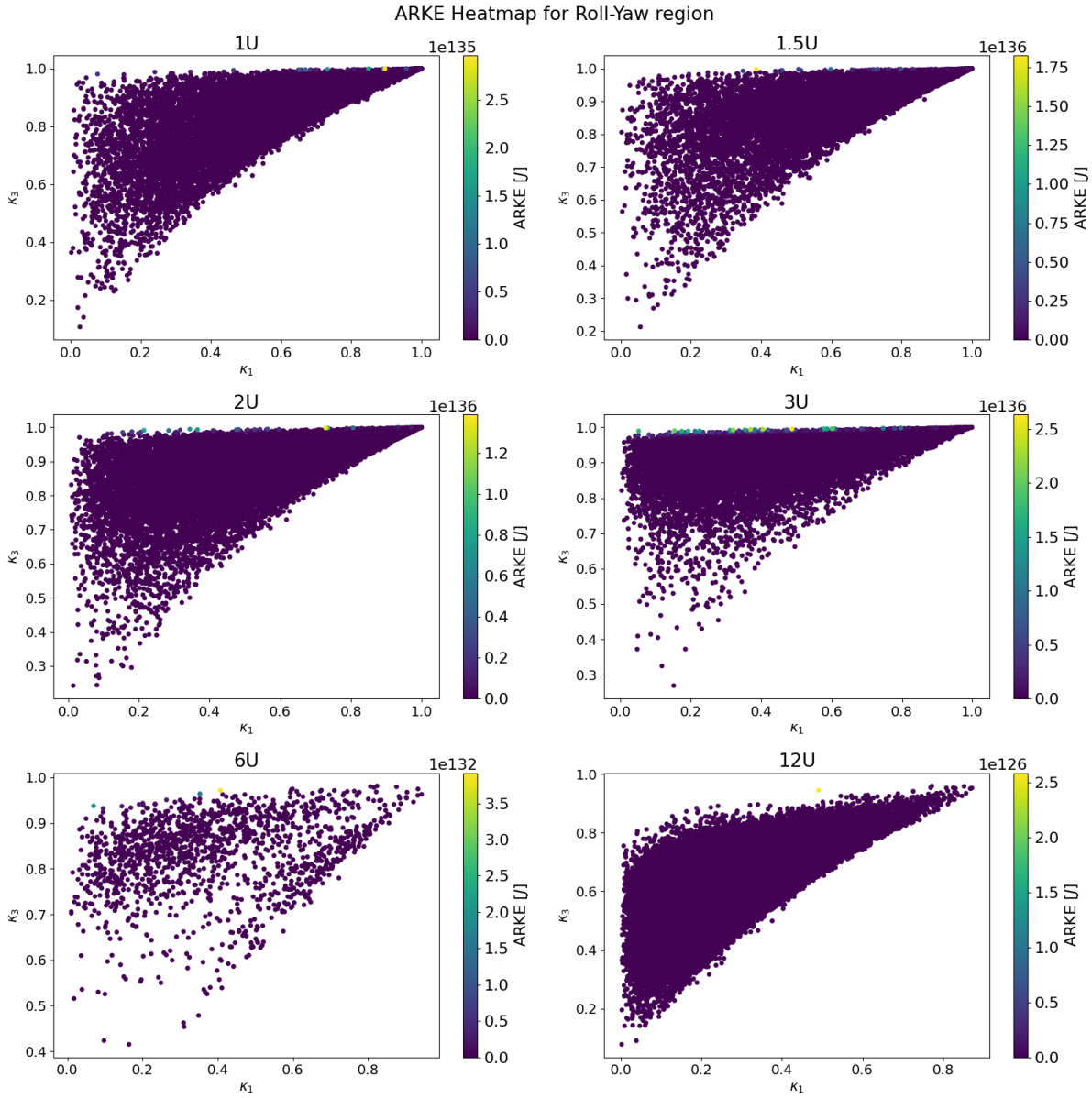

Figure 4.7. GGSM-ARKE Heatmap of the 1U-12U configurations with Roll-Yaw stability.

4.4.2 Trace of Inertia Tensor - tr(J)

The trace of the inertia tensor is proposed empirically as a stability index since the principal moments of inertia are directly related to the RKE equation, Eq. (4.15). Although, the body velocity, $\boldsymbol{\omega}$, is also present in the RKE equation, for the three-axis stable regions - Lagrange and Debra-Delp - the trace of $\mathbf{J}_B^c$ index can be promising, since for these regions the attitude remains oscillatory within a constant range.

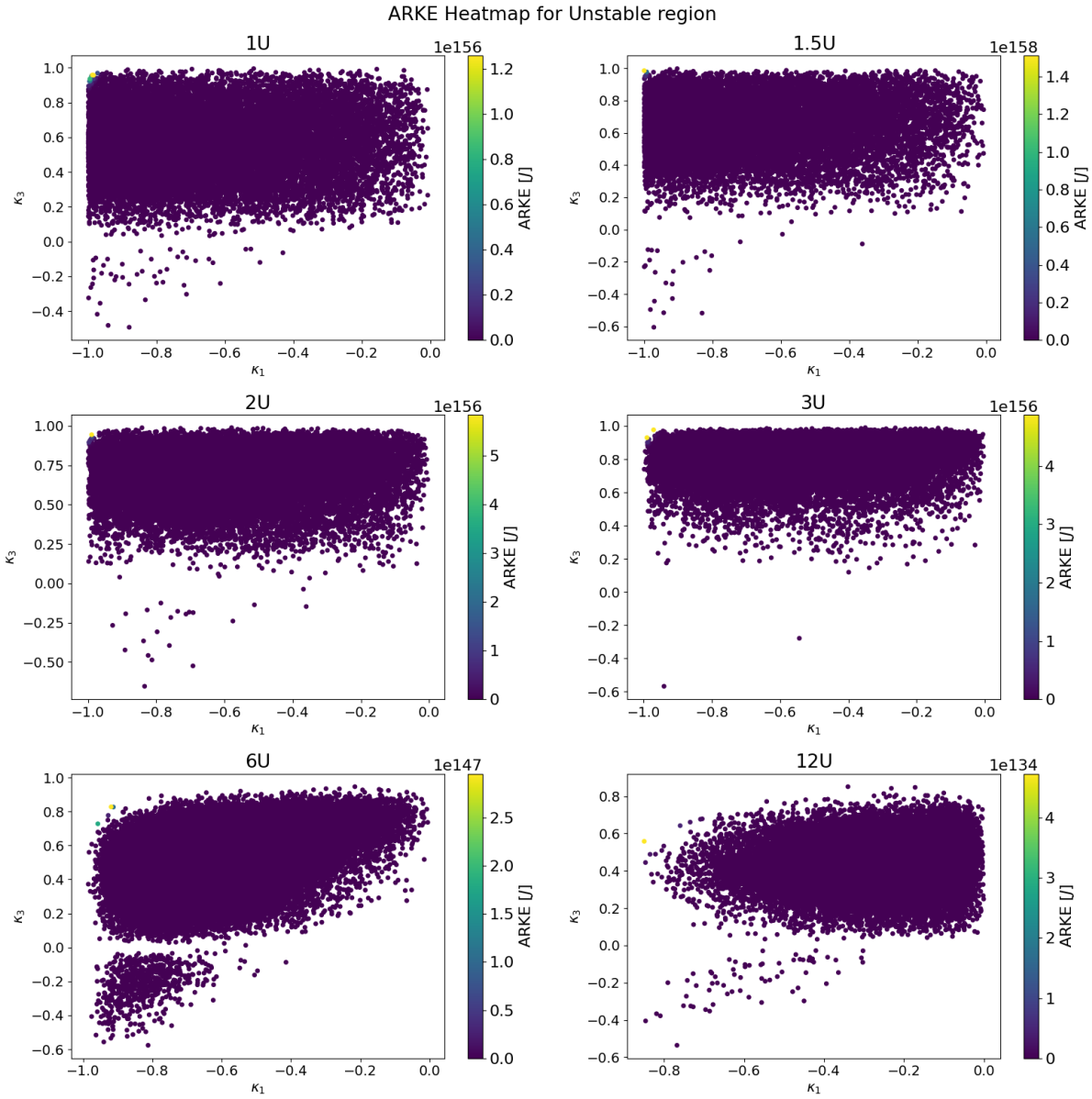

Figure 4.8. GGSM-ARKE Heatmap of the 1U-12U configurations within the Unstable region.

4.4.3 Sum of the Norm of the Characteristic Roots - SNCR

The summation of the roots' norm of the dynamic system, Eq. (3.36), is an approach inspired by the modulus margin, described in (EUROPEAN COOPERATION FOR SPACE STANDARDIZATION, 2010), from the classical control design theory. The analysis relates the Sum of the Norm of the Characteristic Roots (SNCR) to the ARKE and seeks for patterns in each region of the GGSM. Similarly to the SMM, we generated ARKE heatmaps of the complex plane of roll-yaw and pitch systems and formulated the calculation of the SNCR index following the patterns presented in the heatmaps.

For the Lagrange region, as shown in Figures 4.9 and 4.10, we observe a pattern similar to the SMM index, characterized by a nearly uniform ARKE distribution across the roots of both systems. Therefore, we formulate the SNCR for this region as follows:

$$SNCR = \sum_{i=1}^{n} \sqrt{s_i^2}, \tag{4.22}$$

where s is the set of roots for both Roll-Yaw and Pitch systems. This formulation ensures that all characteristic roots equally contribute to the system's dynamics.

Figures 4.11 and 4.12 represent the roots of the configurations from the Debra-Delp region. In this region, when the characteristic roots of the Roll-Yaw system approach the origin, they exhibit higher ARKE patterns. Consequently, the SNCR for the DD region is defined as:

$$SNCR = \sum_{i=1}^{n} \sqrt{(s_i^{RY})^2}, \tag{4.23}$$

where s^{RY} denotes the roots of the Roll-Yaw system.

For the region characterized by stable Pitch motion, illustrated in Figures 4.13 and 4.14, we observe that higher energy roots are located at the extremes of the complex plane for both systems. Thus, we use the same SNCR formula as in Eq. (4.22), considering all roots to contribute to the system's dynamics equally.

In the Roll-Yaw stable region of the GGSM, the ARKE pattern appears only for the roots of the Pitch system, as seen in Figure 4.15 and Figure 4.16. Therefore, the SNCR formula for the Roll-Yaw region is:

$$SNCR = \sum_{i=1}^{n} \sqrt{(s_i^{P})^2}, \tag{4.24}$$

where s^P represents the roots of the Pitch system.

Finally, in the Unstable region, the higher energy roots are also located at the extremes of the complex plane, demonstrated in Figure 4.17 and Figure 4.18. Thus, we apply Eq. (4.22) again, treating all roots as equally contributing to the body's attitude dynamics.

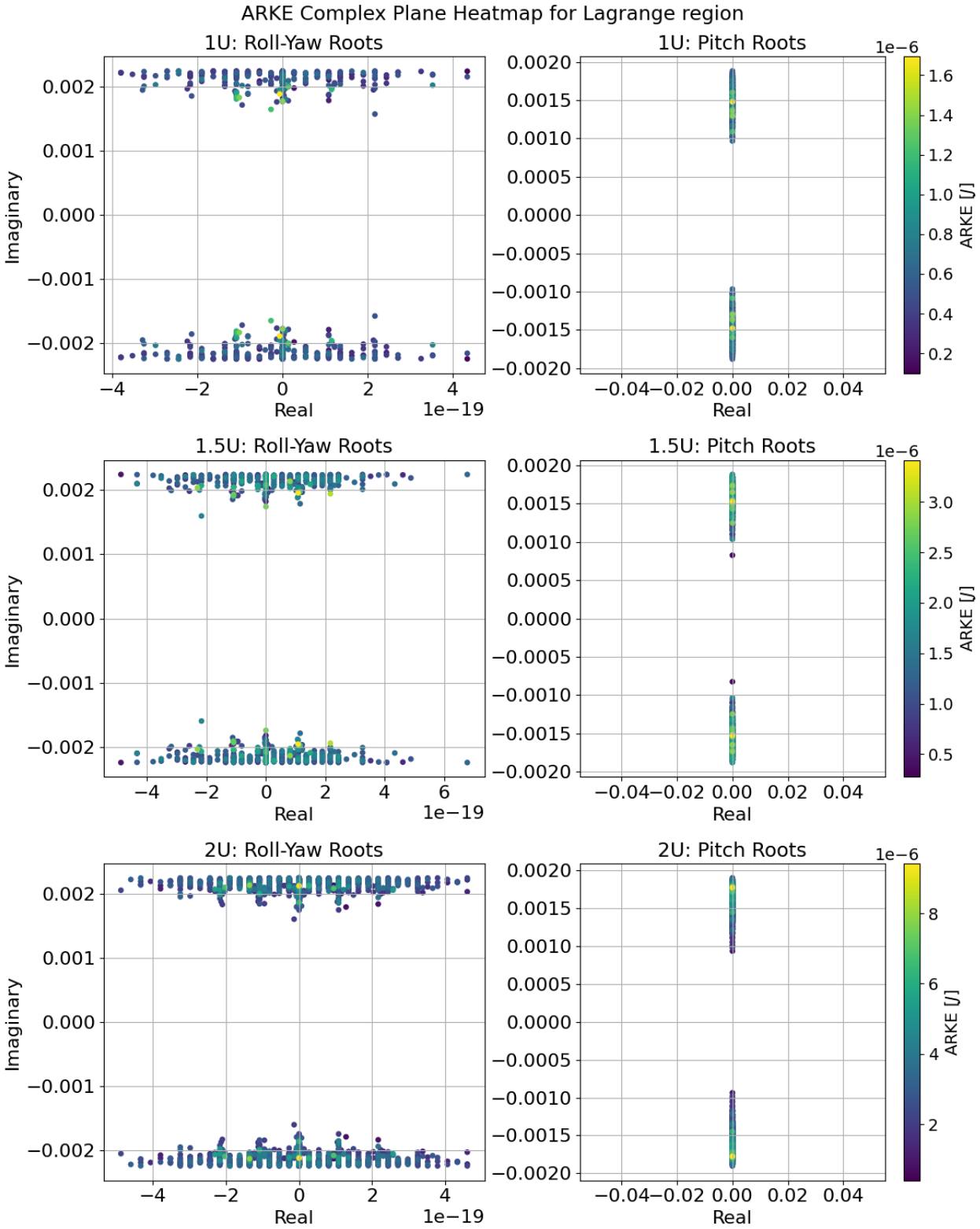

Figure 4.9. ARKE Heatmap of the system's characteristic roots of 1U-2U Configurations with Lagrange stability.

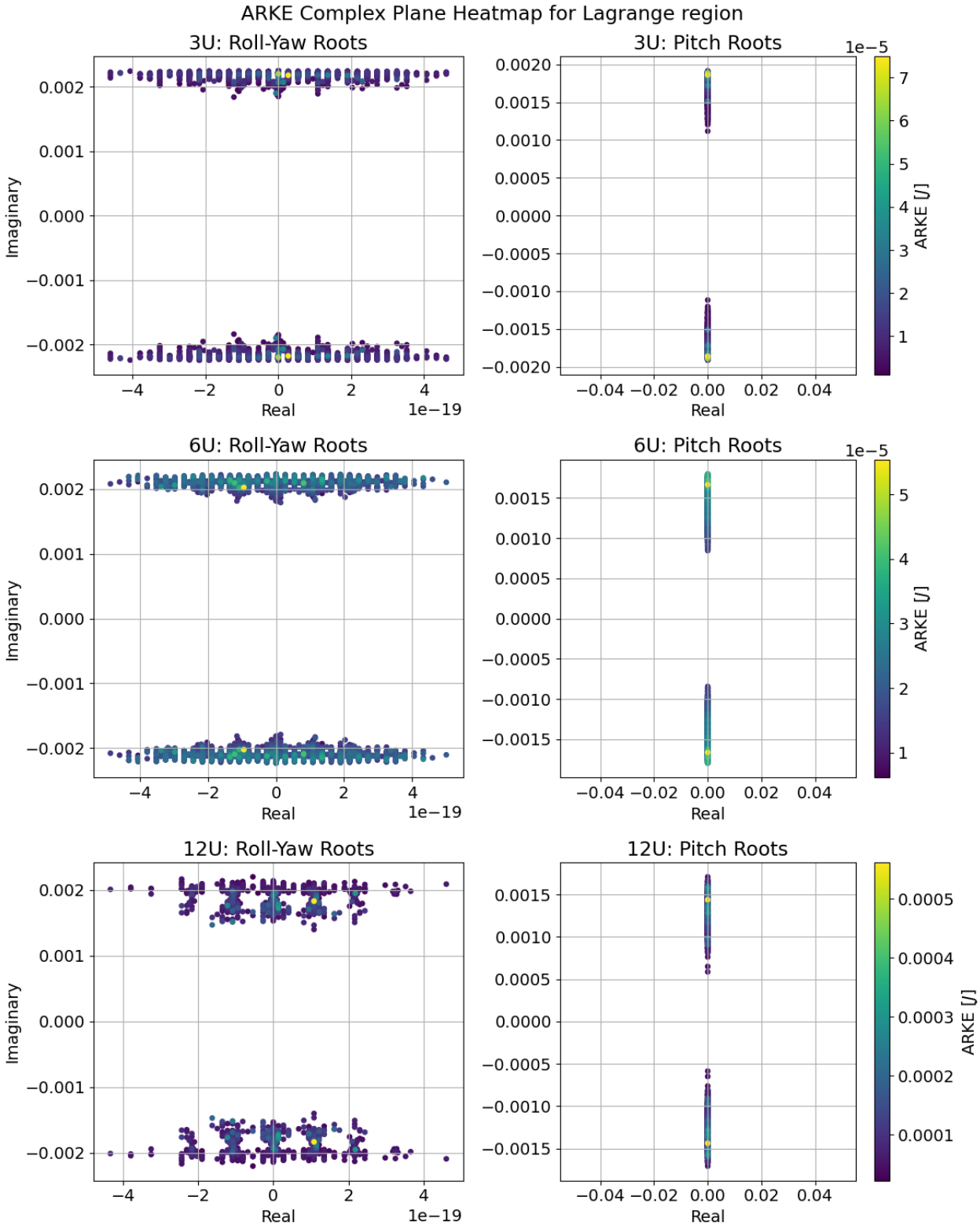

Figure 4.10. ARKE Heatmap of the system's characteristic roots of 3U-12U configurations with Lagrange stability.

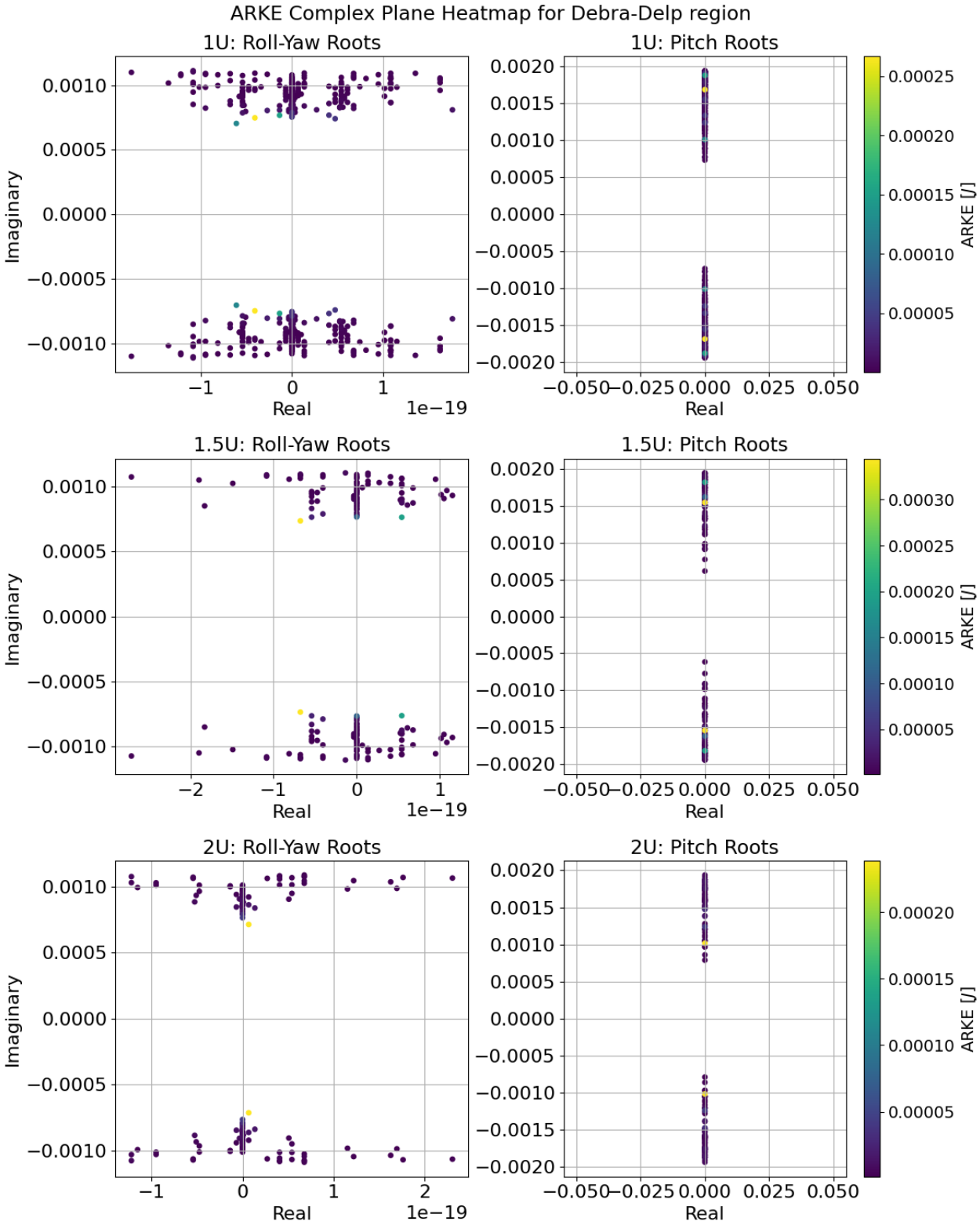

Figure 4.11. ARKE Heatmap of the system's characteristic roots of 1U-2U configurations with Debra-Delp stability.

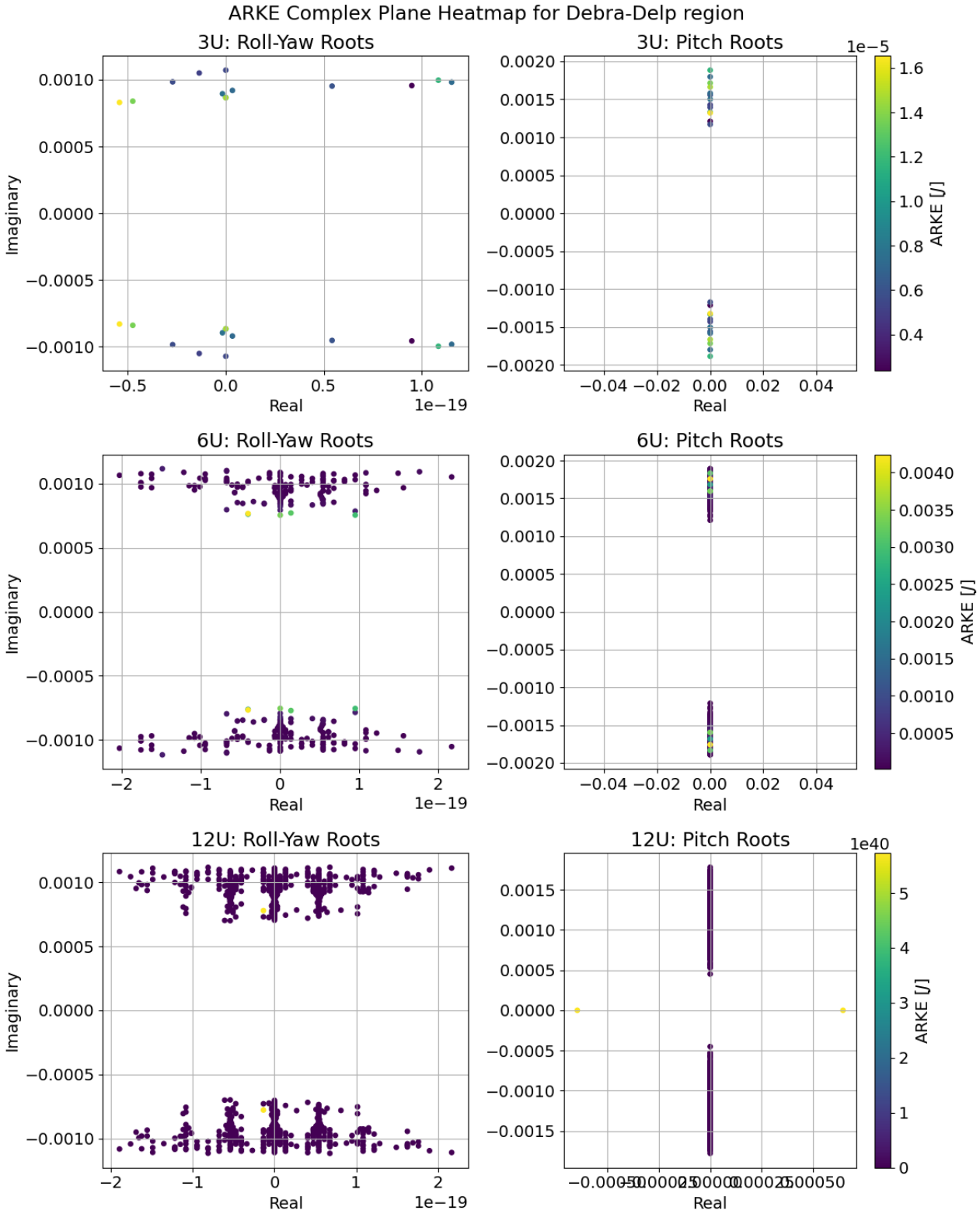

Figure 4.12. ARKE Heatmap of the system's characteristic roots of 3U-12U configurations with Debra-Delp stability.

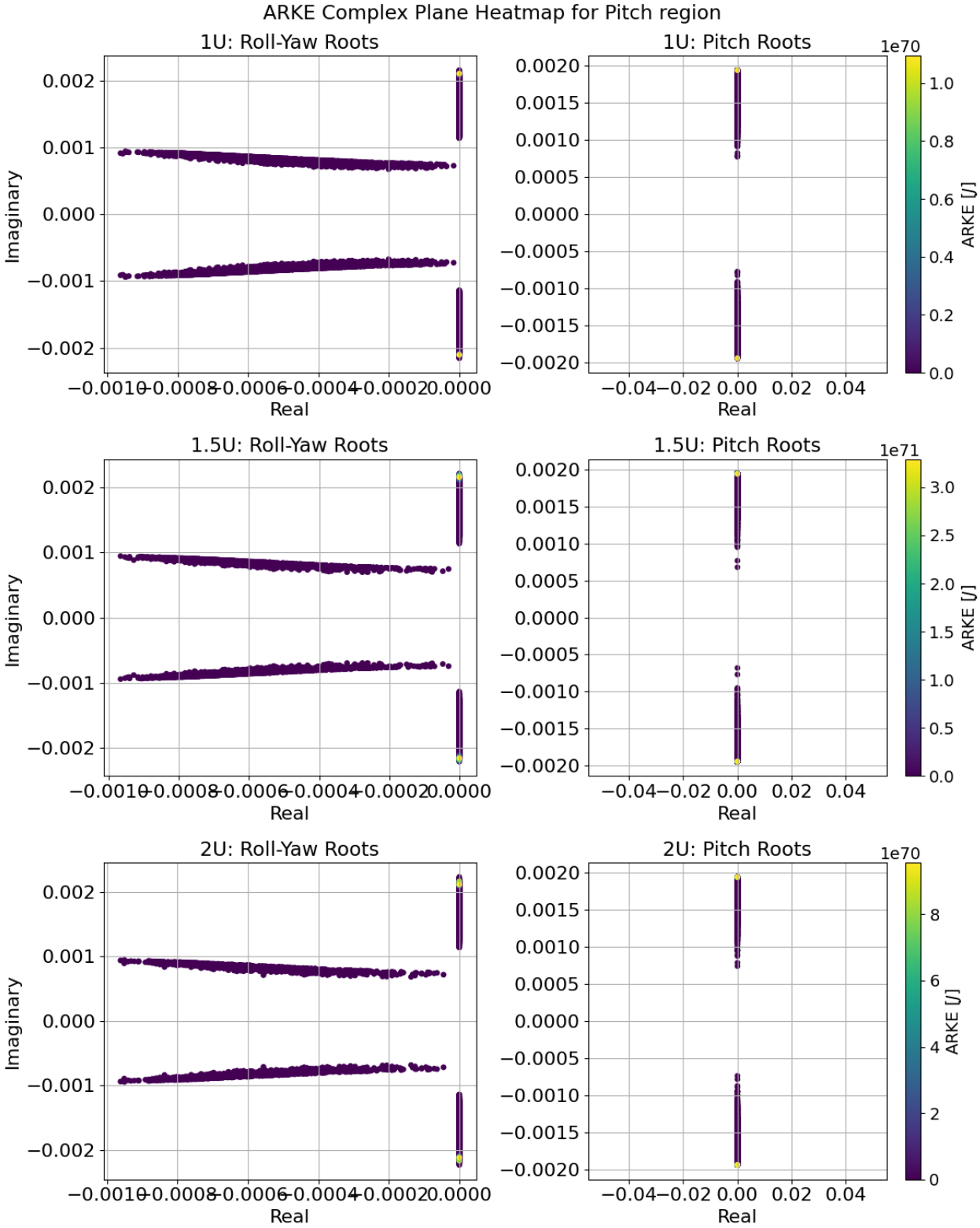

Figure 4.13. ARKE Heatmap of the system's characteristic roots of 1U-2U configurations with Pitch stability.

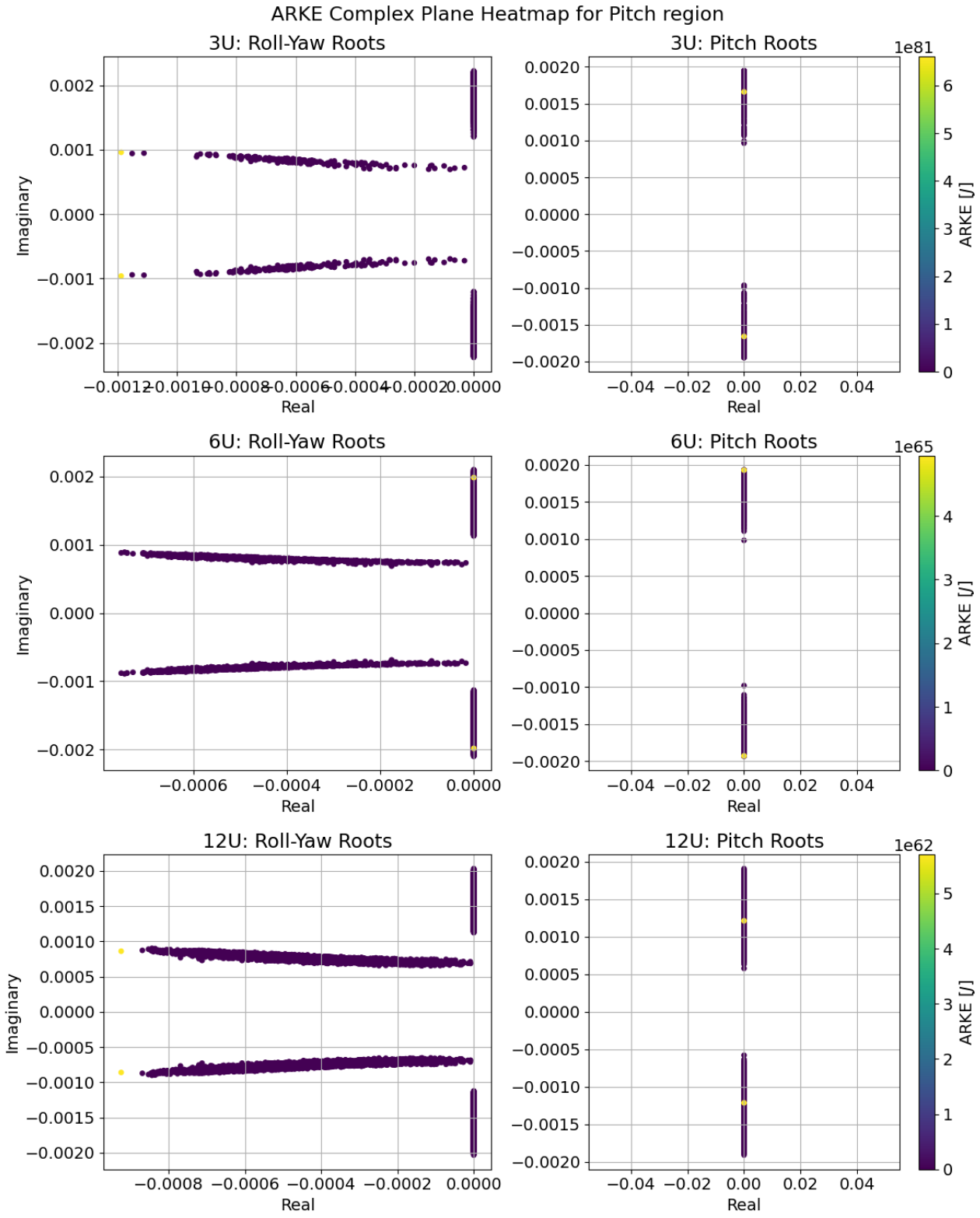

Figure 4.14. ARKE Heatmap of the system's characteristic roots of 3U-12U configurations with Pitch stability.

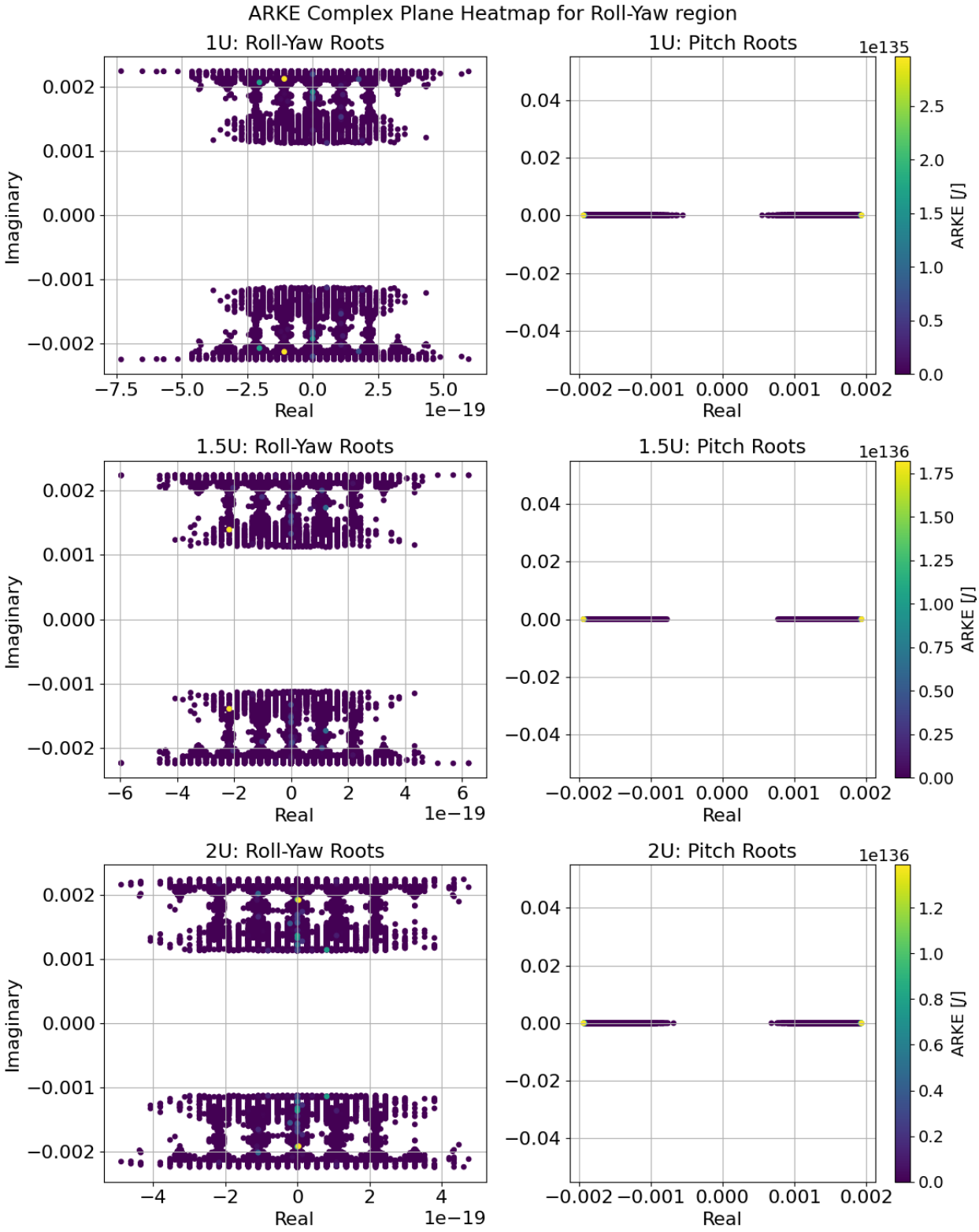

Figure 4.15. ARKE Heatmap of the system's characteristic roots of 1U-2U configurations with Roll-Yaw stability.

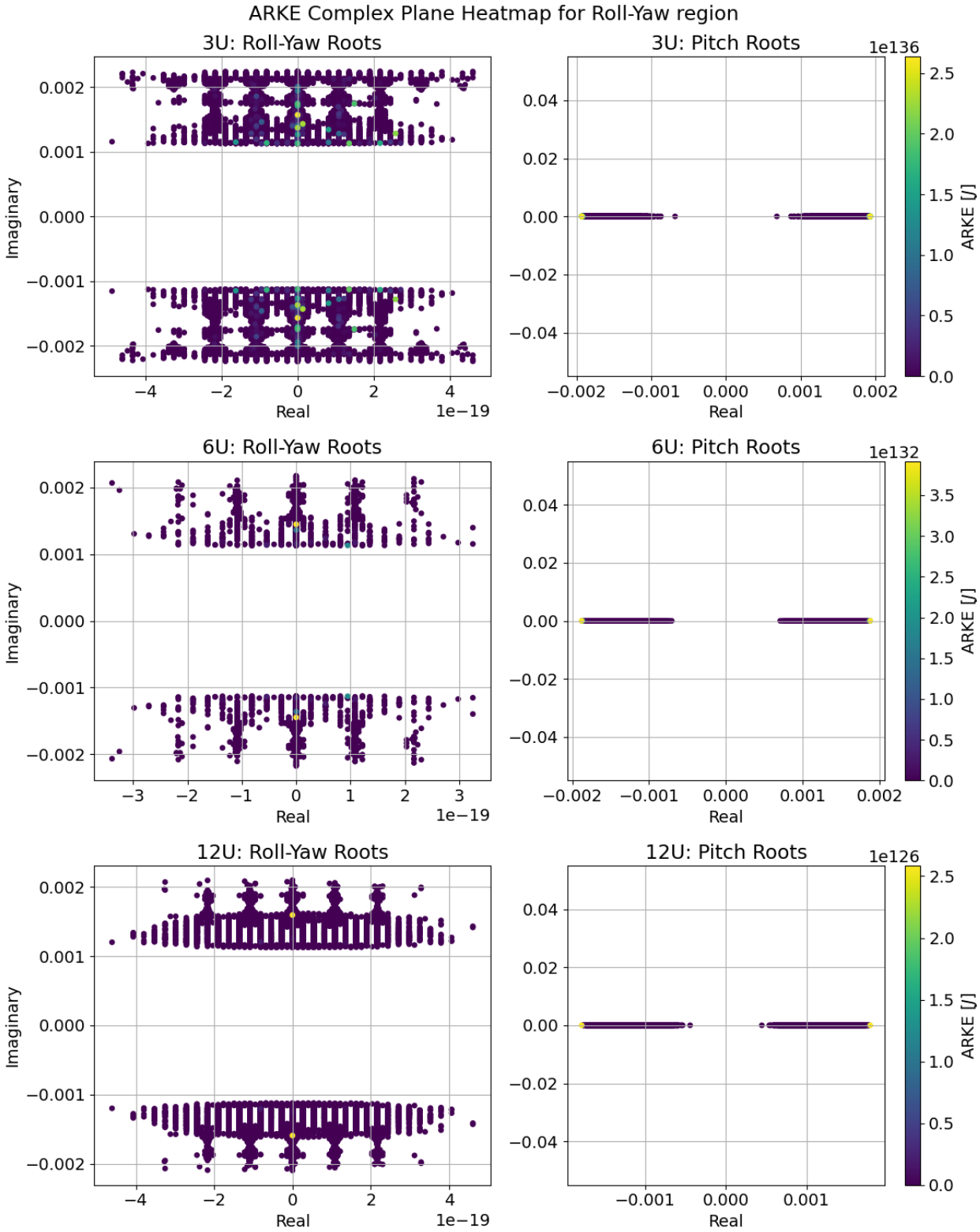

Figure 4.16. ARKE Heatmap of the system's characteristic roots of 3U-12U configurations with Roll-Yaw stability.

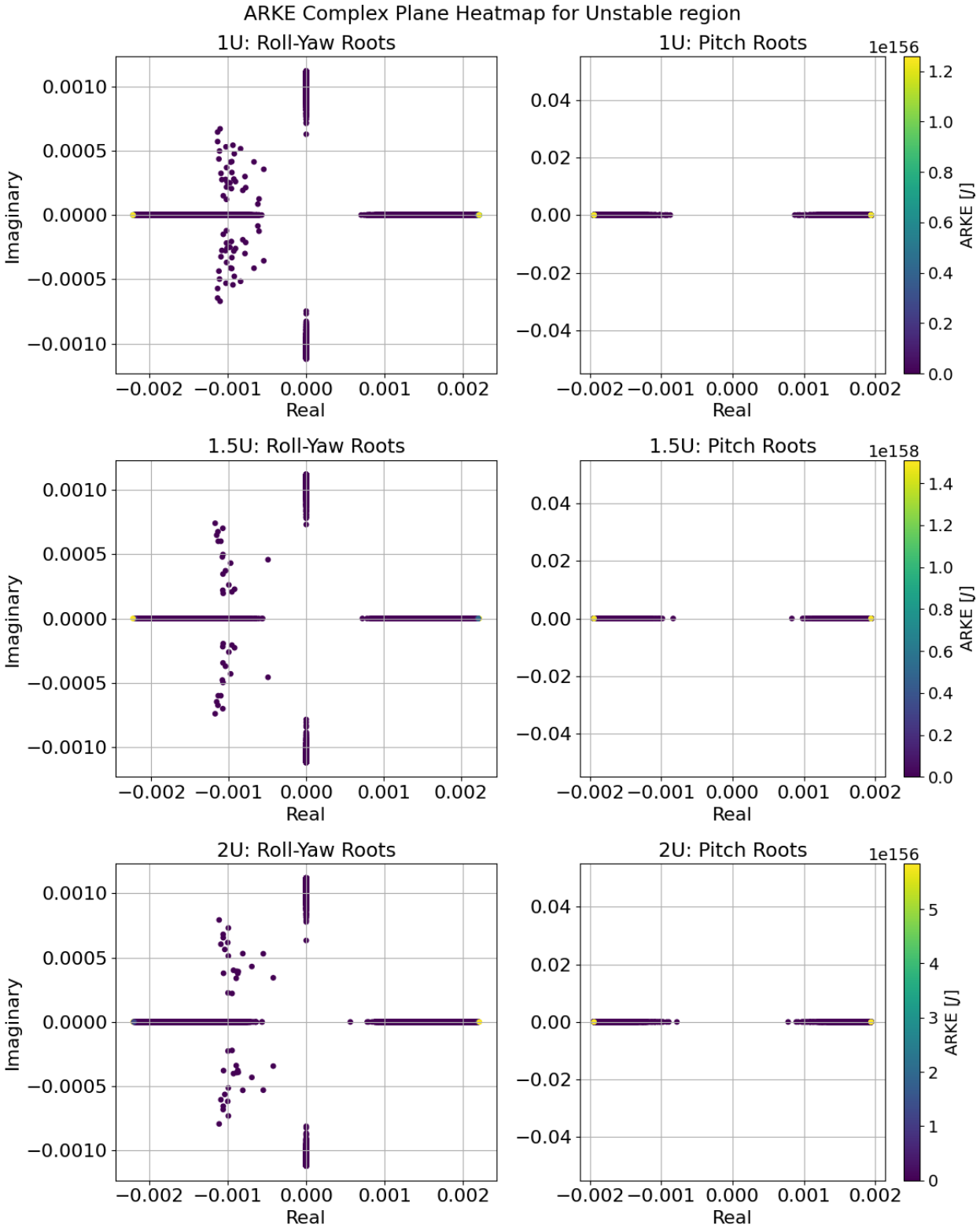

Figure 4.17. ARKE Heatmap of the system's characteristic roots of 1U-2U configurations within Unstable region.

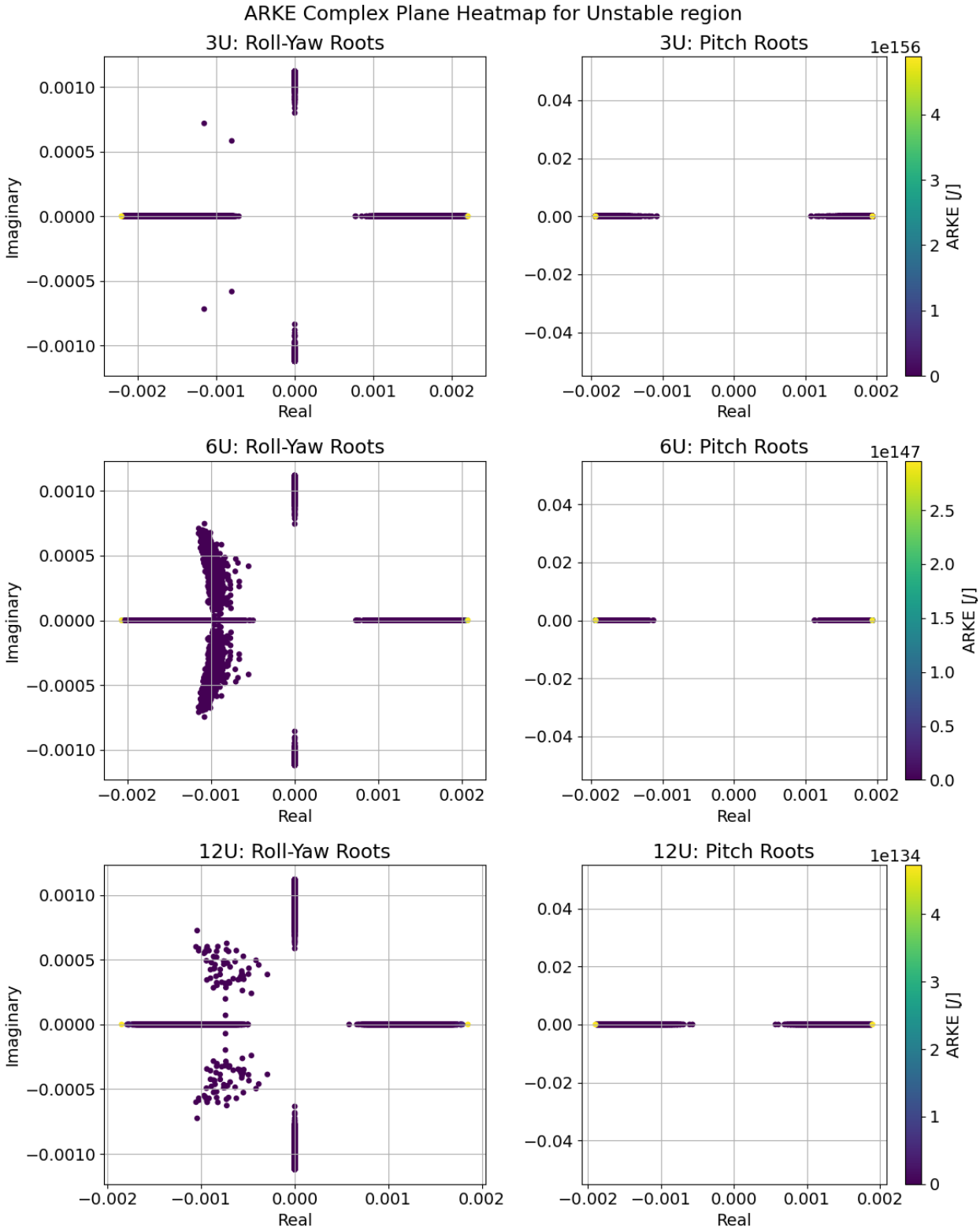

Figure 4.18. ARKE Heatmap of the system's characteristic roots of 3U-12U configurations within Unstable region.

4.5 DUMMY MASS GRID

The Dummy Mass Grid is a design enhancement proposal based on engineering model (EUROPEAN COOPERATION FOR SPACE STANDARDIZATION, 2023). It involves creating a grid of potential additional mass locations within the CubeSat to generate new configurations from the original design. For each potential mass location, the algorithm calculates all the CubeSat's body and GG stability features, analyzing opportunities for improved configurations. During this process, configurations belonging to different GGSM regions may emerge, which may increase or reduce its stability margin and cinematic performance.

The additional mass could represent a subsystem or a physical dummy mass. Its primary purpose is to determine an optimal location that enhances the CubeSat's attitude characteristics. Figure 4.19 illustrates the Dummy Mass Grid proposal. The example begins with an initially unstable 2U configuration.

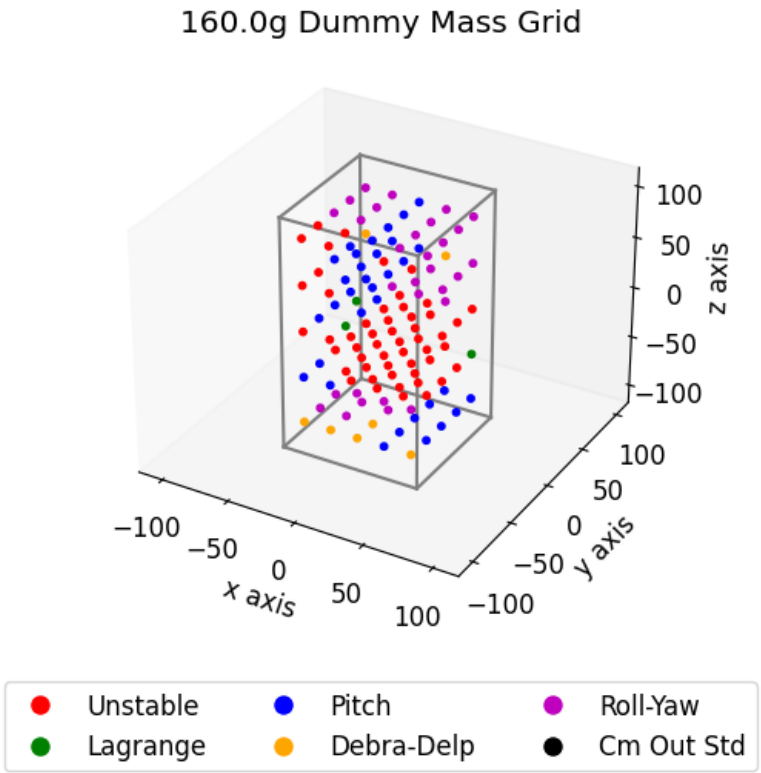

Figure 4.19. Example of the Dummy Mass Grid analysis in a 2U CubeSat. All dimensions are represented in $[mm]$ and the GGSM regions are color coded in the legend.

A 160g mass is added to the original configuration, and each point in the grid represents a potential location for the mass. At each location, the assembly exhibits different stability

characteristics. As shown, this method transforms an initially unstable configuration into one with numerous improved stability options, including configurations in all other GGSM regions. One important thing is that many better stability options appear with the additional mass.

4.6 SIMULATIONS

For this analysis, four types of simulations were conducted: the Average Rotational Kinetic Energy (ARKE) simulation, the regulation control simulation, the attitude motion simulation for power generation analysis, and the dummy mass simulation for design optimization.

4.6.1 ARKE simulation

The ARKE simulation is the primary analysis of this work and serves as the basis for the other three simulations. In the ARKE simulation, we investigate patterns in ARKE to identify empirical models for stability indices. This involves generating a large number of CubeSat samples, propagating their attitude motion under GG torque alone, calculating the average kinetic energy of the motion, and examining ARKE patterns corresponding to proposed stability indices. Figure 4.20 presents the flowchart detailing the algorithm structure, while Table 4.5 lists the parameters used in this simulation.

During the post-processing step, to compare the performance of the empirical models, we used the Least Squares Polynomial Fitting (LSPF) to adjust a curve and calculate the Mean Square Error (MSE) of the data to the adjusted curve. To do the polynomial fitting we used polynomials of order from 1 to 20. As we saw in the heatmaps scale, for the regions in which there is any axis of instability the values grow exponentially, due to this we did the curve adjustment with the normalized ARKE data:

$$x_i = \frac{x_i - x_{min}}{x_{max} - x_{min}}. \tag{4.25}$$

Table 4.5. Parameters of the ARKE simulation

CubeSat Sample			
Size	**No. of samples**	**No. of samples according to CDS**	**No. of Subsystems**
1U	100000	50456	5
1.5U	100000	37010	5
2U	100000	62607	6
3U	100000	70515	7
6U	100000	87580	12
12U	100000	95799	16
Attitude Dynamics			
Time Step	0.1	$[s]$	
Simulation Time	86400	$[s]$	16 orbits
Orbit Altitude	500	$[km]$	LEO
Orbit Eccentricity	0		Circular orbit
Attitude Initial Conditions	$\begin{bmatrix} 0.8 & 0.5 & 0.6 \end{bmatrix}^T$	$[^\circ/s]$	Angular velocity $\boldsymbol{\omega}_B^{BI}$
	$\begin{bmatrix} 0 & 0 & 0 \end{bmatrix}^T$	$[^\circ]$	Euler angles $(\psi\ \theta\ \phi)$
Regulation Control Gain	0		GGS only
Polynomial Fitting			
Polymonial Orders	1-20		

4.6.2 Dummy Mass Grid Simulation

The Dummy Mass Grid simulation is a proposed method for design enhancement, aimed at identifying potential configurations that improve the original CubeSat design. The flow diagram for this simulation is presented in Figure 4.21.

The process begins by selecting a CubeSat sample to improve. In this study, we chose the LARKE configurations for each CubeSat size. Next, the following inputs are defined: the CubeSat size to investigate; the Grid Nodes, corresponding to the number of divisions along each axis of the CubeSat body; the Mass Fraction, representing the fraction of the CubeSat's total mass allowed by (JOHNSTONE, 2022), as detailed in Table 4.1; The number of masses to simulate, generating the mass array. The input values used to generate the grid are summarized in Table 4.6.

Once the simulation inputs are configured, the algorithm calculates new CubeSat samples based on the generated grid and performs the attitude dynamics analysis for the open-loop system. Finally, the simulation outputs include plots and Excel files summarizing the results.

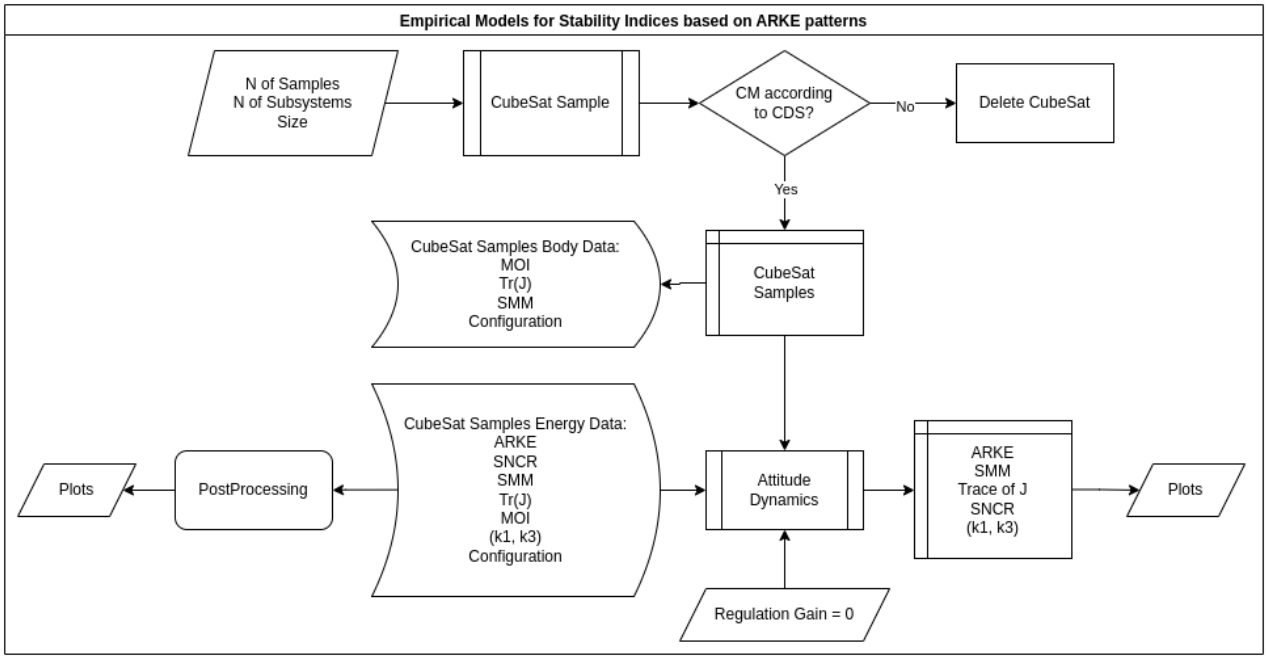

Figure 4.20. Diagram representing the simulation flow of the investigation for empirical models of stability indices based on ARKE patterns.

Table 4.6. Dummy Mass Grid inputs

Size	Dummy Mass Array $[g]$	No. Grid Nodes	No. of Grid Points
1U	[40, 80, 120, 160, 200]	5	125
1.5U	[60, 120, 180, 240, 300]		
2U	[80, 160, 240, 320, 400]		
3U	[120, 240, 360, 480, 600]		
6U	[240, 480, 720, 960, 1200]		
12U	[480, 960, 1440, 1920, 2400]		

4.6.3 Regulation Control Simulations

The simulations involving the regulation control system primarily aim to demonstrate the improvements in motion and control efforts when using empirical models of stability indices to evaluate a design. In this work, we conducted two types of control simulations.

The first simulation compares the control performance of two samples from the same GGSM region with extreme ARKE values: LARKE and HARKE. These data are extracted during the ARKE simulation and saved in an Excel file. Subsequently, the attitude motion is simulated in a closed-loop system, and performance metrics, as outlined in Subsection 4.3.1, are analyzed. The flowchart for this simulation is presented in Figure 4.22, while the simulation parameters are detailed in Table 4.5 and Table 4.7.

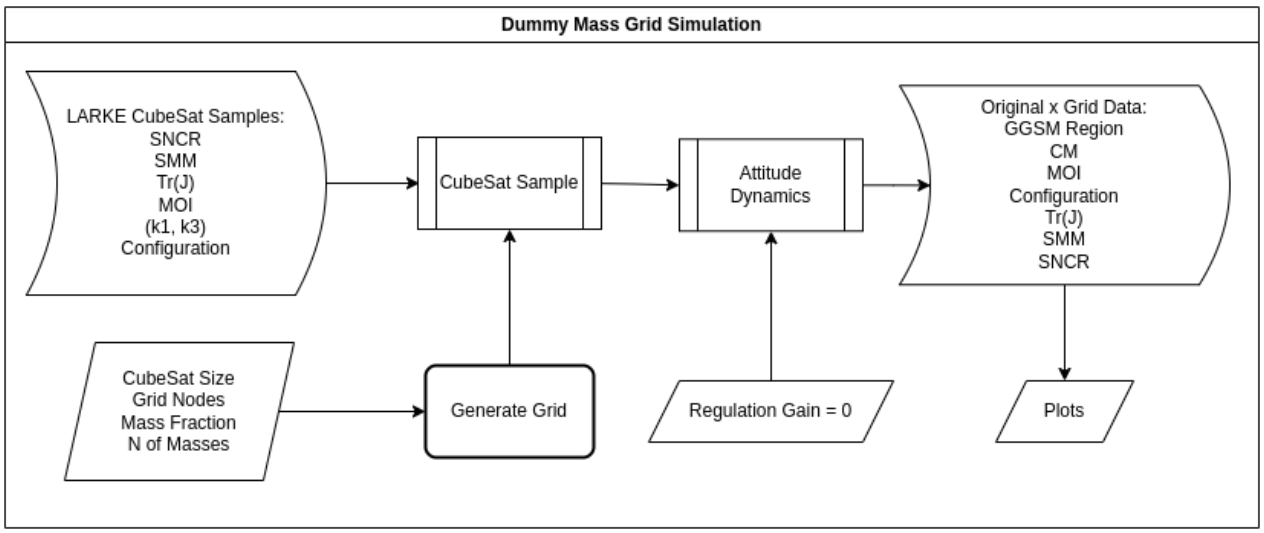

Figure 4.21. Diagram representing the simulation flow of the investigation for empirical models of stability indices based on ARKE patterns.

The second analysis compares the attitude control responses of an initial LARKE configuration, derived from the ARKE simulation, with its improved design based on the Dummy Mass Grid analysis. First, the algorithm reads the Excel file generated by the Dummy Mass Grid simulation (Figure 4.21) and identifies the proposed configuration with the best Stability Index among the configurations generated by the grid, referred to as the improved Dummy Mass design. Subsequently, the algorithm follows the same process as the previous simulation, as shown in Figure 4.23.

The input parameters for this simulation are detailed in Table 4.7 and Table 4.9. Both simulations produce plots and Excel files summarizing the results.

4.6.4 Attitude Motion and Power Generation Simulation

Both STK and Python were utilized to analyze the impact of GGS attitude motion on power generation. In Python, we selected the configuration with the lowest ARKE for each CubeSat size, propagated its attitude motion, and generated plots of the Euler angles. These Euler angles were then exported to an Excel file and converted to a `.a` file, the attitude format compatible with STK. The CubeSat sizes for this simulation range from 1U to 6U. Figure 4.24 presents the mechanical models of CubeSats available in the STK models database (AVELINO *et al.*, 2024).

Table 4.7. Simulation parameters of the Attitude and Control systems

Attitude Motion			
Time Step OL	1	$[s]$	
Simulation Time OL	43200	$[s]$	8 orbits
Time Step CL	0.001	$[s]$	
Simulation Time CL	30	$[s]$	
Orbit Altitude	500	$[km]$	LEO
Orbit Inclination	45	$[^\circ]$	Inclined Orbit
Orbit Eccentricity	0		Circular orbit
Attitude Initial Conditions	$\begin{bmatrix} 0.8 & 0.5 & 0.6 \end{bmatrix}^T$	$[^\circ/s]$	Angular velocity $\boldsymbol{\omega}_B^{BI}$
	$\begin{bmatrix} 0 & 0 & 0 \end{bmatrix}^T$	$[^\circ]$	Euler angles $(\psi\ \theta\ \phi)$
	$\begin{bmatrix} 0 & 0 & 0 \end{bmatrix}^T$	$[Nms]$	Wheels Angular Momentum ($\mathbf{H}_B^w$)
Regulation Control Gain	0.02		Control Gain for 1U
	0.03		Control Gain for 1.5U
	0.04		Control Gain for 2U
	0.06		Control Gain for 3U
	0.12		Control Gain for 6U
	0.24		Control Gain for 12U

In STK, we configured the scenario according to Table 4.10 and simulated the power generated. The simulations spanned one year, with power generation samples during 24 hours on the 15th and 16th of each month. These specific days were chosen under the assumption that mid-month power generation would provide a reasonable estimate of the monthly average (KAZMI, 2024; AVELINO *et al.*, 2024). Figure 4.25 illustrates the flow of the described simulation.

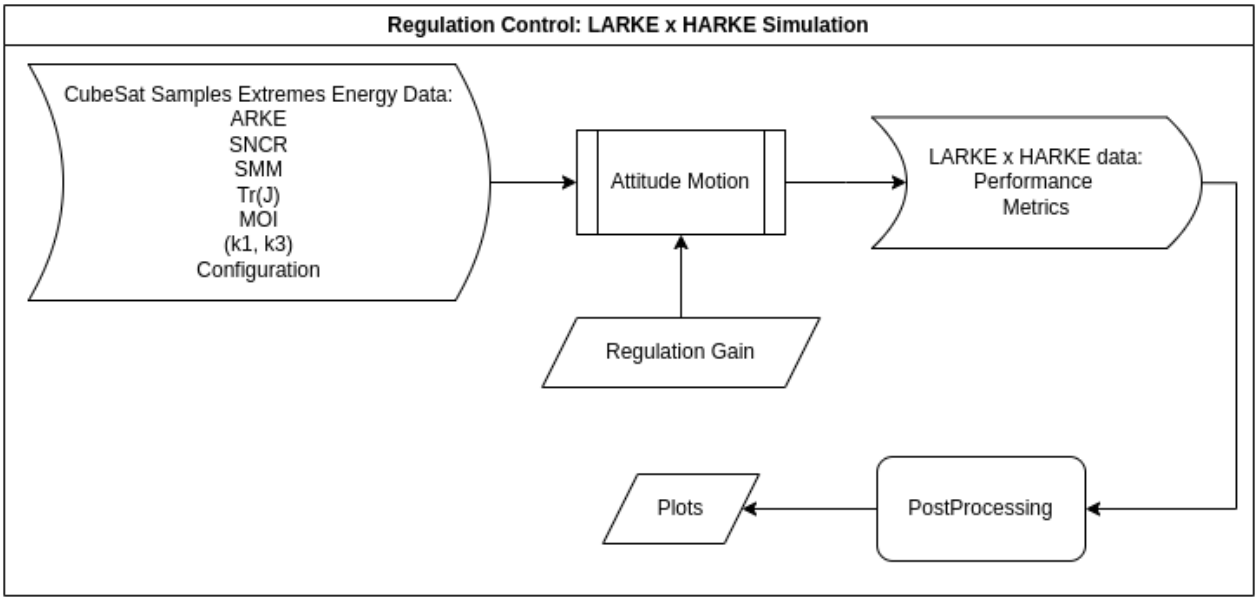

Figure 4.22. Diagram representing the simulation flow of the Regulation Control: LARKE x HARKE designs.

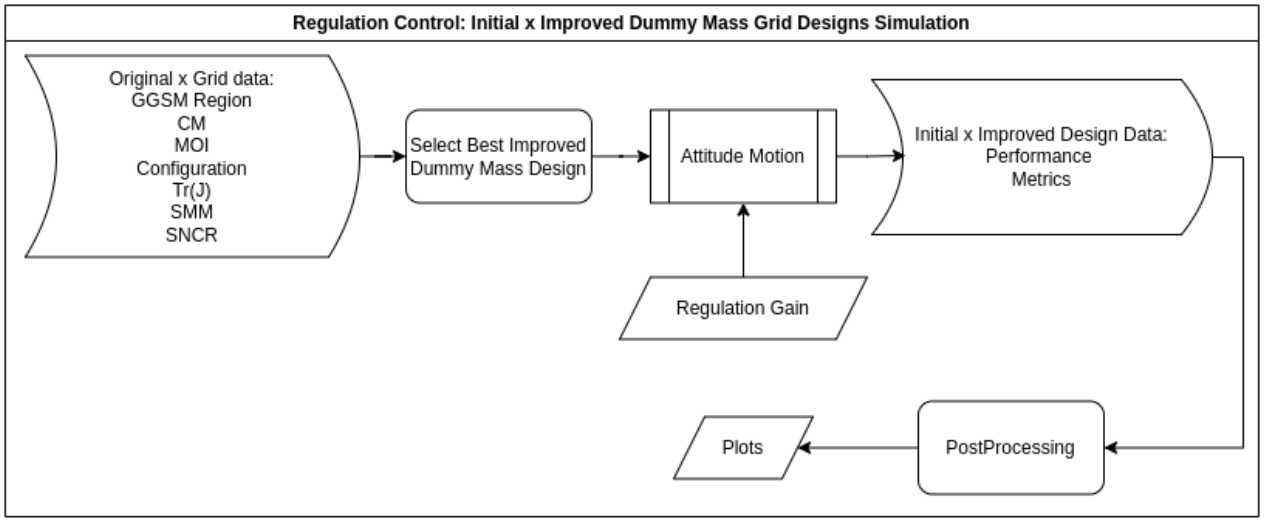

Figure 4.23. Diagram representing the simulation flow of the Regulation Control: Initial x Improved Dummy Mass Grid designs.

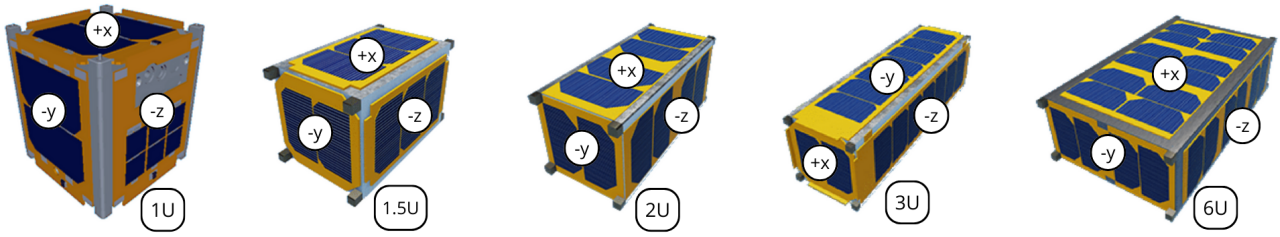

Figure 4.24. CubeSat models, with the indication of the face orientation, available in STK v.11 used in the power generation simulations. Source: Adapted from (AVELINO *et al.*, 2024)

Table 4.8. Parameters of the HARKE and LARKE designs, based on the ARKE Empirical Models for Stability Indices, under the same control system.

Size	GGSM Region	ARKE [J]		MOI $\begin{bmatrix} J_1 & J_2 & J_3 \end{bmatrix}$ $[kg \cdot m^2]$	
		HARKE	LARKE	HARKE	LARKE
1U	Lagrange	1.69e-6	9.84e-8	[0.0031 0.0032 0.0013]	[0.0008 0.0010 0.0002]
	Debra-Delp	2.67e-4	2.93e-7	[0.0049 0.0026 0.0029]	[0.0008 0.0004 0.0005]
	Pitch	1.09e+70	5.31e-4	[0.0051 0.0046 0.0005]	[0.0058 0.0034 0.0038]
	Roll-Yaw	2.96e+135	8.51e+31	[2.4981e-05 5.4847e-03 5.4624e-03]	[0.0026 0.0029 0.0029]
	Unstable	1.26e+156	4.31e+55	[7.2038e-05 3.3558e-03 3.4269e-03]	[0.0014 0.0016 0.0018]
1.5U	Lagrange	3.42e-6	2.74e-7	[0.0131 0.0137 0.0047]	[0.0020 0.0023 0.0007]
	Debra-Delp	3.45e-4	9.60e-7	[0.0058 0.0034 0.0037]	[0.0028 0.0021 0.0023]
	Pitch	3.29e+71	1.39e-3	[0.0181 0.0170 0.0011]	[0.0060 0.0030 0.0033]
	Roll-Yaw	1.82e+136	5.34e+48	[4.1768e-05 1.5100e-02 1.5084e-02]	[0.0044 0.0055 0.0053]
	Unstable	1.51e+158	9.37e+52	[3.7288e-05 5.0623e-03 5.0996e-03]	[0.0034 0.0039 0.0041]
2U	Lagrange	9.42e-6	4.03e-7	[0.0261 0.0264 0.0040]	[0.0033 0.0041 0.0010]
	Debra-Delp	2.39e-4	1.34e-6	[0.0098 0.0070 0.0079]	[0.0045 0.0034 0.0035]
	Pitch	9.56e+70	1.22e-2	[0.0359 0.0326 0.0033]	[0.0129 0.0079 0.0089]
	Roll-Yaw	1.39e+136	1.02e+42	[0.0001 0.0270 0.0269]	[0.0063 0.0085 0.0074]
	Unstable	5.84e+156	2.02e+49	[0.0009 0.0333 0.0342]	[0.0057 0.0066 0.0068]
3U	Lagrange	7.49e-5	1.08e-6	[0.1063 0.1067 0.0086]	[0.0088 0.0108 0.0027]
	Debra-Delp	1.65e-5	2.38e-6	[0.0173 0.0109 0.0122]	[0.0079 0.0054 0.0058]
	Pitch	6.61e+81	3.27e-3	[0.0864 0.0060 0.0820]	[0.0128 0.0076 0.0086]
	Roll-Yaw	2.63e+136	1.04e+42	[0.0010 0.1128 0.1123]	[0.0061 0.0080 0.0070]
	Unstable	4.88e+156	8.13e+71	[0.0010 0.0822 0.0831]	[0.0081 0.0114 0.0116]
6U	Lagrange	5.54e-5	6.12e-6	[0.0998 0.1011 0.0255]	[0.0410 0.0519 0.0260]
	Debra-Delp	4.24e-3	1.56e-5	[0.1762 0.0913 0.1013]	[0.0575 0.0393 0.0410]
	Pitch	4.95e+65	1.35e-2	[0.2108 0.1757 0.0375]	[0.1451 0.0795 0.0886]
	Roll-Yaw	3.92e+132	8.99e+44	[0.0061 0.1311 0.1286]	[0.0545 0.1080 0.0687]
	Unstable	2.96e+147	7.28e+75	[0.0170 0.1736 0.1892]	[0.0301 0.0423 0.0443]
12U	Lagrange	5.62e-4	2.24e-5	[0.3307 0.3327 0.1483]	[0.1567 0.1901 0.0786]
	Debra-Delp	1.88e-2	3.74e-5	[0.3179 0.2199 0.2492]	[0.1847 0.1568 0.1637]
	Pitch	5.71e+62	2.22e-2	[0.3599 0.1222 0.3122]	[0.2625 0.1851 0.2101]
	Roll-Yaw	2.59e+126	5.71e+25	[0.0499 0.4841 0.4596]	[0.1653 0.1811 0.1747]
	Unstable	4.73e+134	1.22e+35	[0.1240 0.4141 0.5195]	[0.1972 0.2122 0.2154]

Table 4.9. Parameters of the Initial and Improved Dummy Mass Grid designs, based on the ARKE Empirical Models for Stability Indices, under the same control system.

Size	Region		MOI $\left[\begin{array}{ccc} J_1 & J_2 & J_3 \end{array}\right]$ $[kg \cdot m^2]$		Empirical model			
					Initial		Improved	
	Initial	Improved	Initial	Improved	Model	Value	Model	Value
1U	Pitch	Debra-Delp	[0.0025 0.0023 0.0021]	[0.0026 0.0024 0.0025]	SMM	0.160	SMM	0.129
	Roll-Yaw	Lagrange	[0.0024 0.0027 0.0026]	[0.0029 0.0031 0.0027]	SNCR	0.001	SMM	0.071
	Unstable	Lagrange	[0.0014 0.0016 0.0017]	[0.0018 0.0020 0.0014]	SMM	0.204	SMM	0.122
1.5U	Pitch	Lagrange	[0.0055 0.0051 0.0049]	[0.0070 0.0074 0.0050]	SMM	0.123	Tr(J)	0.019
	Roll-Yaw	Lagrange	[0.0039 0.0050 0.0047]	[0.0063 0.0067 0.0045]	SNCR	0.001	Tr(J)	0.017
	Unstable	Lagrange	[0.0034 0.0038 0.0041]	[0.0040 0.0043 0.0036]	SMM	0.185	Tr(J)	0.012
2U	Pitch	Debra-Delp	[0.0056 0.0052 0.0048]	[0.0059 0.0054 0.0055]	SMM	0.165	SMM	0.14
	Roll-Yaw	Lagrange	[0.0060 0.0080 0.0069]	[0.0087 0.0089 0.0070]	SNCR	0.001	Tr(J)	0.025
	Unstable	Lagrange	[0.0055 0.0063 0.0065]	[0.0065 0.0068 0.0057]	SMM	0.162	Tr(J)	0.019
3U	Debra-Delp	Lagrange	[0.0149 0.0097 0.0099]	[0.01382 0.0187 0.01]	SMM	0.059	Tr(J)	0.043
	Pitch	Lagrange	[0.0079 0.0068 0.0058]	[0.0075 0.0082 0.0065]	SMM	0.320	Tr(J)	0.022
	Roll-Yaw	Lagrange	[0.0057 0.0075 0.0066]	[0.0112 0.0119 0.0072]	SNCR	0.001	Tr(J)	0.030
	Unstable	Lagrange	[0.0117 0.0078 0.0142]	[0.0118 0.0145 0.0081]	SMM	0.265	Tr(J)	0.034
6U	Pitch	Lagrange	[0.0583 0.0465 0.0395]	[0.0727 0.0850 0.0436]	SMM	0.419	Tr(J)	0.201
	Roll-Yaw	Roll-Yaw	[0.0534 0.1058 0.0673]	[0.0560 0.1083 0.0678]	SNCR	0.0014	SNCR	0.0013
	Unstable	Lagrange	[0.1002 0.0338 0.1152]	[0.1018 0.1182 0.0359]	SMM	0.236	Tr(J)	0.256
12U	Pitch	Debra-Delp	[0.2152 0.1982 0.1925]	[0.2212 0.2115 0.2119]	SMM	0.115	SMM	0.176
	Roll-Yaw	Lagrange	[0.1554 0.1702 0.1643]	[0.1848 0.1990 0.1647]	SNCR	0.001	SMM	0.086
	Unstable	Lagrange	[0.1854 0.1994 0.2025]	[0.2075 0.2172 0.1921]	SNCR	0.003	SMM	0.05

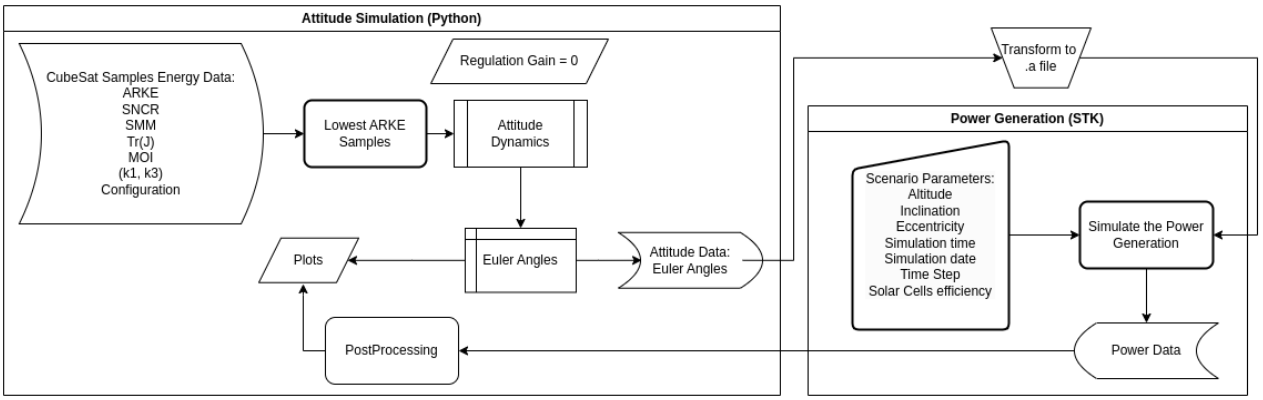

Figure 4.25. Diagram representing the simulation flow of the influence of the GGS motion of the Power Generation.

Table 4.10. Parameters of the Attitude Motion and Power Generation Simulation simulation

CubeSat Samples			
Size	**MOI** $\left[\begin{array}{ccc} J_1 & J_2 & J_3 \end{array}\right]$ $[kg \cdot m^2]$	**ARKE** $[J]$	**GGSM Region**
1U	[0.00042989 0.00050906 0.0001171]	5.15e-8	Lagrange
	[0.00035437 0.0002054 0.00021647]	1.18e-7	Debra-Delp
	[0.00066279 0.0007746 0.00072568]	1.15e+31	Roll-Yaw
	[0.00113665 0.0006458 0.00072075]	8.87e-5	Pitch
	[0.00145294 0.00164775 0.0017856]	4.37e+55	Unstable
1.5U	[0.00159181 0.00200268 0.00052667]	1.92e-7	Lagrange
	[0.00287418 0.00244893 0.00265397]	7.83e-7	Debra-Delp
	[0.00261552 0.00544104 0.00326911]	5.09e+40	Roll-Yaw
	[0.00224129 0.00156386 0.00177321]	1.75e-04	Pitch
	[0.00253218 0.00287697 0.00309353]	1.09e+54	Unstable
2U	[0.00443056 0.00501243 0.00063303]	4.89e-7	Lagrange
	[0.00240375 0.00143461 0.00155222]	8.83e-7	Debra-Delp
	[0.00881896 0.01102408 0.01003692]	9.68e+38	Roll-Yaw
	[0.00686733 0.00383907 0.00428031]	4.41e-4	Pitch
	[0.00467008 0.00531888 0.00556401]	5.73e+49	Unstable
3U	[0.01044325 0.01159306 0.00199933]	1.24e-6	Lagrange
	[0.01217584 0.00891192 0.00945791]	2.94e-6	Debra-Delp
	[0.01351292 0.01727998 0.01541091]	1.10e+39	Roll-Yaw
	[0.01002433 0.00704063 0.00807088]	523.13	Pitch
	[0.01150798 0.01352612 0.01529382]	1.64e+67	Unstable
6U	[0.04776759 0.06044112 0.02260638]	6.43e-6	Lagrange
	[0.04874524 0.03264122 0.03515224]	1.45e-5	Debra-Delp
	[0.06064768 0.08037582 0.06816748]	1.16e+36	Roll-Yaw
	[0.09102948 0.04705864 0.05226268]	7.41e-3	Pitch
	[0.15421741 0.04891905 0.17123922]	7.28e+75	Unstable

Attitude Motion			
Time Step	0.1	$[s]$	
Simulation Time	86400	$[s]$	16 orbits
Orbit Altitude	500	$[km]$	LEO
Orbit Inclination	90	$[^\circ]$	Polar Orbit
Orbit Eccentricity	0		Circular orbit
Attitude Initial Conditions	$\left[\begin{array}{ccc} 0.8 & 0.5 & 0.6 \end{array}\right]^T$	$[^\circ/s]$	Angular velocity $\boldsymbol{\omega}_B^{BI}$
	$\left[\begin{array}{ccc} 0 & 0 & 0 \end{array}\right]^T$	$[^\circ]$	Euler angles $(\psi\ \theta\ \phi)$
	$\left[\begin{array}{ccc} 0 & 0 & 0 \end{array}\right]^T$	$[Nms]$	Wheels Angular Momentum $(\mathbf{H}_B^w)$
Regulation Control Gain	0		GGS only
Power Generation			
Time Step	60	$[s]$	
Simulation Time	86400	$[s]$	1 day
Simulation Dates	15th-16th	$[day]$	Each month of 2024
Orbit Altitude	500	$[km]$	LEO
Orbit Inclination	90	$[^\circ]$	Polar Orbit
Orbit Eccentricity	0		Circular orbit
Solar-Cells Efficiency	0.3		BOL efficiency

CHAPTER 5

RESULTS AND DISCUSSIONS

In this chapter, we focus on presenting and discussing the results obtained from the four simulations described in the previous chapter. For the ARKE empirical models of stability indices, we analyze the performance of each proposed index in relation to the normalized ARKE data for each GGSM region and each CubeSat size. The selection of the most suitable empirical model is based on the minimum mean squared error (MSE) of the polynomial fitting.

For the Dummy Mass Grid simulation, we explore the potential enhancements to the initial configurations of all six CubeSat sizes in each GGSM region. The best configuration from the grid is chosen based on the empirical models developed in this work. These optimized configurations are later compared with the original ones in the regulation control simulation, where performance metrics of the systems are evaluated.

In addition to the regulation control results, this chapter discusses the performance metrics for LARKE and HARKE configurations in each GGSM region for all CubeSat sizes. Lastly, a dedicated section examines the relationship between the attitude motion of GGS CubeSats and power generation, presenting results on power output and solar incidence for CubeSats ranging from 1U to 6U.

5.1 ARKE EMPIRICAL MODELS FOR STABILITY INDICES

This section presents the primary analyses and results of this work. Using the proposed models, defined in Eqs. (4.17) and (4.24), we evaluate the Least Squares Polynomial Fit (LSPF) and Mean Squared Error (MSE) of the normalized ARKE data for each empirical model. To visualize the ARKE distribution of the empirical models, we also include the polynomial fitting for each GGSM region of the 12U size. The 12U simulation is highlighted as it has the largest number of samples, following the CDS, as detailed in Table 4.5.

Additionally, we also present the ARKE patterns of the Lagrange and Unstable regions of the 6U size, since these cases have a larger number of samples, and represent the best-suited empirical models for those regions in the majority of the cases.

Table 5.1 presents the empirical models with the lowest MSE for the 20th-order polynomial fitting, along with a comparison to the MSE of the other proposed models. Starting with the Lagrange region, analyzing Table 5.1, we observe the Tr(J) model emerges as the best-suited stability index for CubeSat sizes ranging from 1.5U to 6U. The 6U size, having the largest number of Lagrange samples, further reinforces Tr(J) as a reliable stability index for the Lagrange region. In Figure 5.1, we can see the majority of ARKE data well fitted to the Tr(J) model.

However, the SMM model also stands out as the most suitable index for the 1U and 12U sizes. It is worth noting that for the 1U size, the MSE difference between the SMM and Tr(J) indices is minimal Table 5.1, suggesting that Tr(J) could also be a viable model option for 1U configurations, also verified in Figure 5.2. Conversely, for the 12U size, the SMM model's MSE is five times smaller than that of Tr(J), achieving the Lagrange region's lowest MSE order of 10^{-4}. Figure 5.3, also confirms that the ARKE pattern shows some dispersed points on the Tr(J) models, while the data fits much better the SMM model.

The ARKE patterns for the Debra-Delp region identified the SMM model as the most suitable stability index across all CubeSat sizes, achieving MSE values on the order of 10^{-3} and 10^{-4} for the 20th-degree polynomial fitting. However, in some cases, such as the 3U size, the Debra-Delp data is sparsely sampled, which may impact the convergence of the LSFP algorithm. Further investigations with a larger and more representative sample size may be necessary. Nevertheless, in general, the ARKE patterns for the Debra-Delp region are best fitted by the SMM model, as also illustrated in Figure 5.4.

Similarly to Debra-Delp pattern, for the Pitch region the SMM model stands out as the best-suited model for the normalized ARKE data. It has the least MSE for all sizes, of orders from 10^{-4} to 10^{-7} for the 20th-degree polynomial, Table 5.1. Figure 5.5 demonstrates the ARKE pattern and the empirical models fitting for the Pitch region. The SMM index indicates that the ARKE metric improves as one approaches the Lagrange or Debra-Dep regions. This result aligns with the expectations set by the heatmap presented in Figure 4.6.

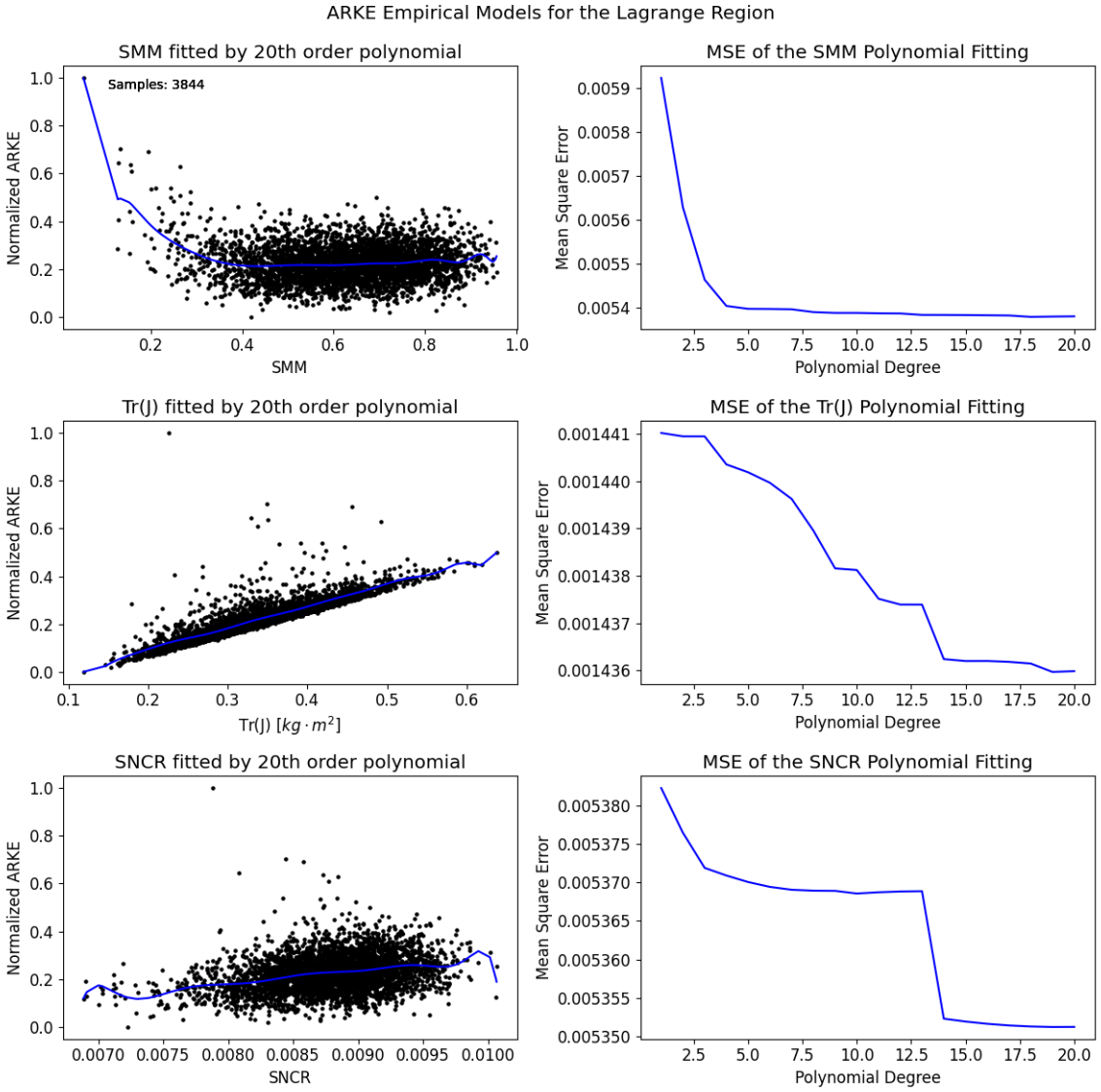

Figure 5.1. Normalized ARKE patterns for SMM, tr(J), and SNCR models for the 6U configurations in the Lagrange region.

For the Roll-Yaw region, the SNCR settled itself as the best empirical model for all sizes. Presenting MSE in many cases three times smaller than the second least MSE and achieving MSE orders of 10^{-5} to 10^{-6}. This result strengthens the assumptions proposed for the SNCR model for the Roll-Yaw region, Eq. (4.24), confirming the expected dominance of the pitch system roots, as seen in Figure 4.7. In Figure 5.6, the performance of each empirical model is presented.

Lastly, from Table 5.1 we have that the SMM model performed incredibly well for the Unstable region, with MSE order of 10^{-5} and 10^{-5}. The typical ARKE pattern for the Unstable region, considering the empirical models, can be seen and analyzed in Figure 5.7. As we can

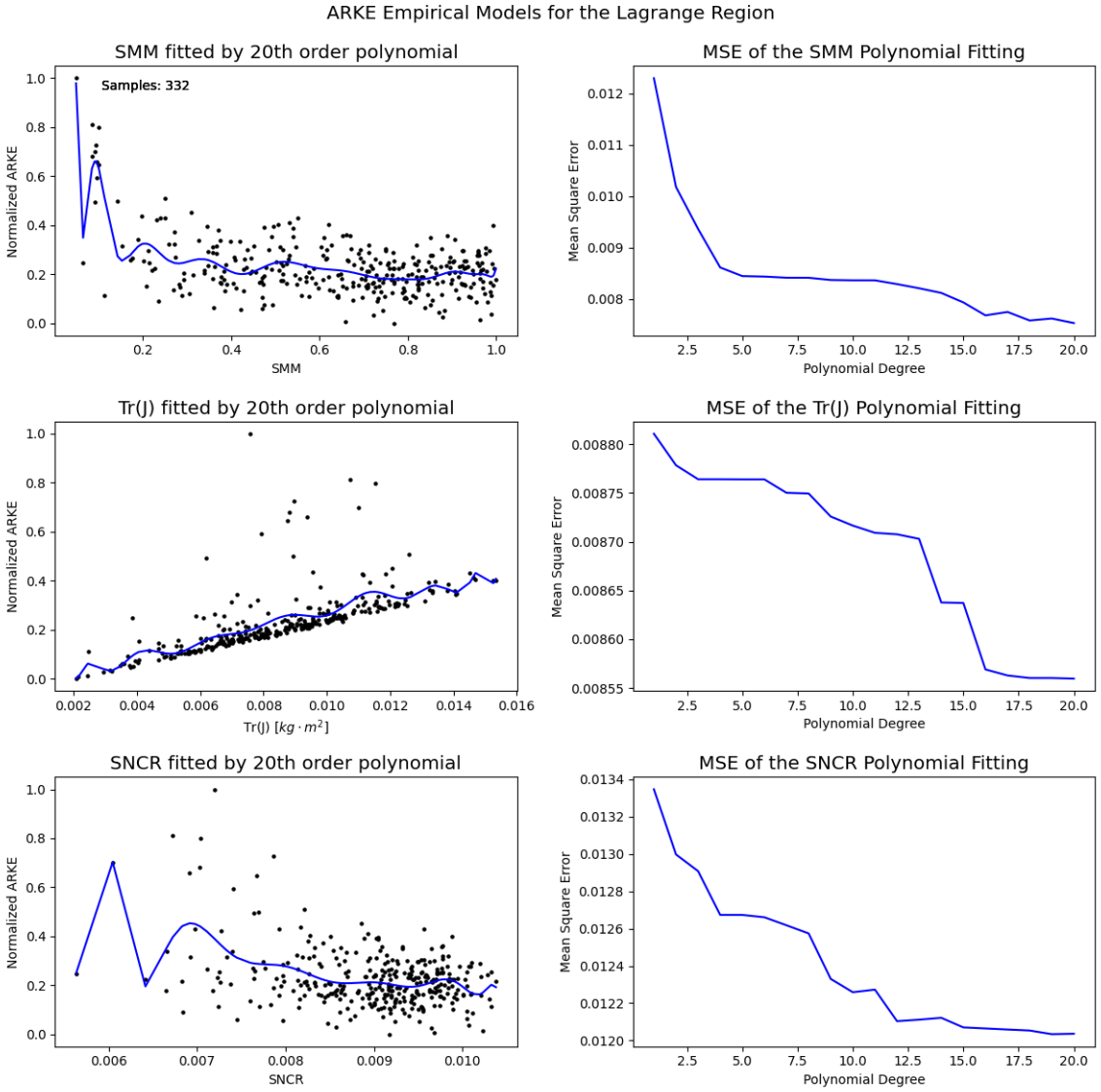

Figure 5.2. Normalized ARKE patterns for SMM, tr(J), and SNCR models for the 1U configurations in the Lagrange region.

see, the normalized ARKE patterns for SMM and SNCR models are very similar, this behavior is also reflected in the data presented by this region in Table 5.1.

Even for 12U size where the SNCR presented better MSE, the SMM model could be used as the stability index, given the minute MSE difference, $1.9 \cdot 10^{-7}$, also confirmed in Figure 5.8. These results align with the expectation from both heatmaps, Figs Figure 4.8, Figure 4.17 and Figure 4.18, presented previously.

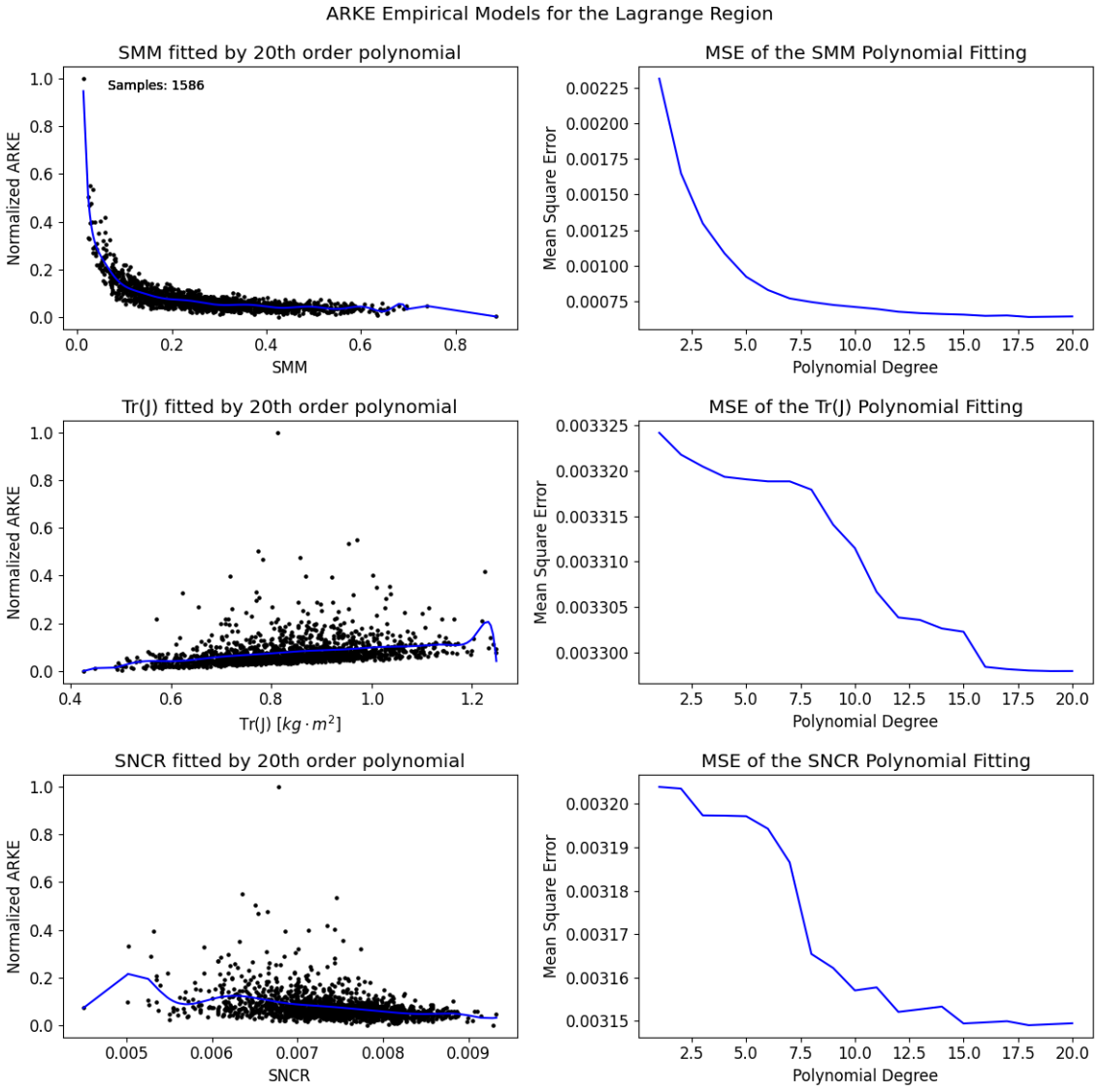

Figure 5.3. Normalized ARKE patterns for SMM, tr(J), and SNCR models for the 12U configurations in the Lagrange region.

Table 5.1. Empirical Models with Least MSE with 20th order polynomial.

Size	GGSM Region	No. of Samples	Best Empirical Model	MSE			
				Least	SMM	Tr(J)	SNCR
1U	Lagrange	332	SMM	7.53e-3	7.53e-3	8.56e-3	1.20e-2
	Debra-Delp	255	SMM	2.28e-3	2.28e-3	6.03e-3	5.59e-3
	Pitch	11848	SMM	6.71e-6	6.71e-6	9.05e-5	5.54e-5
	Roll-Yaw	19611	SNCR	3.12e-5	9.69e-5	9.74e-5	3.12e-5
	Unstable	18410	SMM	4.16e-5	4.16e-5	1.62e-4	7.33e-5
1.5U	Lagrange	464	Tr(J)	6.92e-3	1.58e-2	6.92e-3	1.96e-2
	Debra-Delp	89	SMM	2.77e-3	2.77e-3	1.40e-2	1.25e-2
	Pitch	8208	SMM	8.22e-5	8.22e-5	2.88e-4	1.20e-4
	Roll-Yaw	14998	SNCR	3.56e-5	9.63e-5	9.68e-5	3.56e-5
	Unstable	13251	SMM	3.53e-6	3.53e-6	8.72e-5	4.47e-5
2U	Lagrange	1403	Tr(J)	3.88e-3	7.36e-3	3.88e-3	9.43e-3
	Debra-Delp	69	SMM	1.97e-4	1.97e-4	1.34e-2	1.31e-2
	Pitch	12098	SMM	9.31e-5	9.31e-5	2.40e-4	1.66e-4
	Roll-Yaw	25840	SNCR	3.71e-5	1.16e-4	1.16e-4	3.71e-5
	Unstable	23197	SMM	1.53e-5	1.53e-5	4.68e-5	3.23e-5
3U	Lagrange	2686	Tr(J)	1.20e-3	1.33e-3	1.20e-3	2.31e-3
	Debra-Delp	13	SMM	6.64e-4	6.64e-4	1.70e-2	2.42e-2
	Pitch	9037	SMM	1.03e-4	1.03e-4	1.10e-4	1.11e-4
	Roll-Yaw	30359	SNCR	1.09e-4	3.20e-4	3.21e-4	1.09e-4
	Unstable	28420	SMM	2.37e-5	2.37e-5	7.10e-5	4.52e-5
6U	Lagrange	3844	Tr(J)	1.44e-3	5.38e-3	1.44e-3	5.35e-3
	Debra-Delp	187	SMM	6.02e-4	6.02e-4	1.36e-2	9.70e-3
	Pitch	12421	SMM	9.69e-7	9.69e-7	8.05e-5	6.64e-5
	Roll-Yaw	1492	SNCR	9.56e-5	8.81e-4	9.29e-4	9.56e-5
	Unstable	69636	SMM	5.90e-6	5.90e-6	2.16e-5	6.30e-6
12U	Lagrange	1586	SMM	6.42e-4	6.42e-4	3.30e-3	3.15e-3
	Debra-Delp	703	SMM	6.36e-4	6.36e-4	3.24e-3	3.13e-3
	Pitch	32146	SMM	2.95e-5	2.95e-5	3.11e-5	3.11e-5
	Roll-Yaw	32790	SNCR	6.25e-6	2.89e-5	3.07e-5	6.25e-6
	Unstable	28573	SNCR	6.93e-6	7.12e-6	3.58e-5	6.93e-6

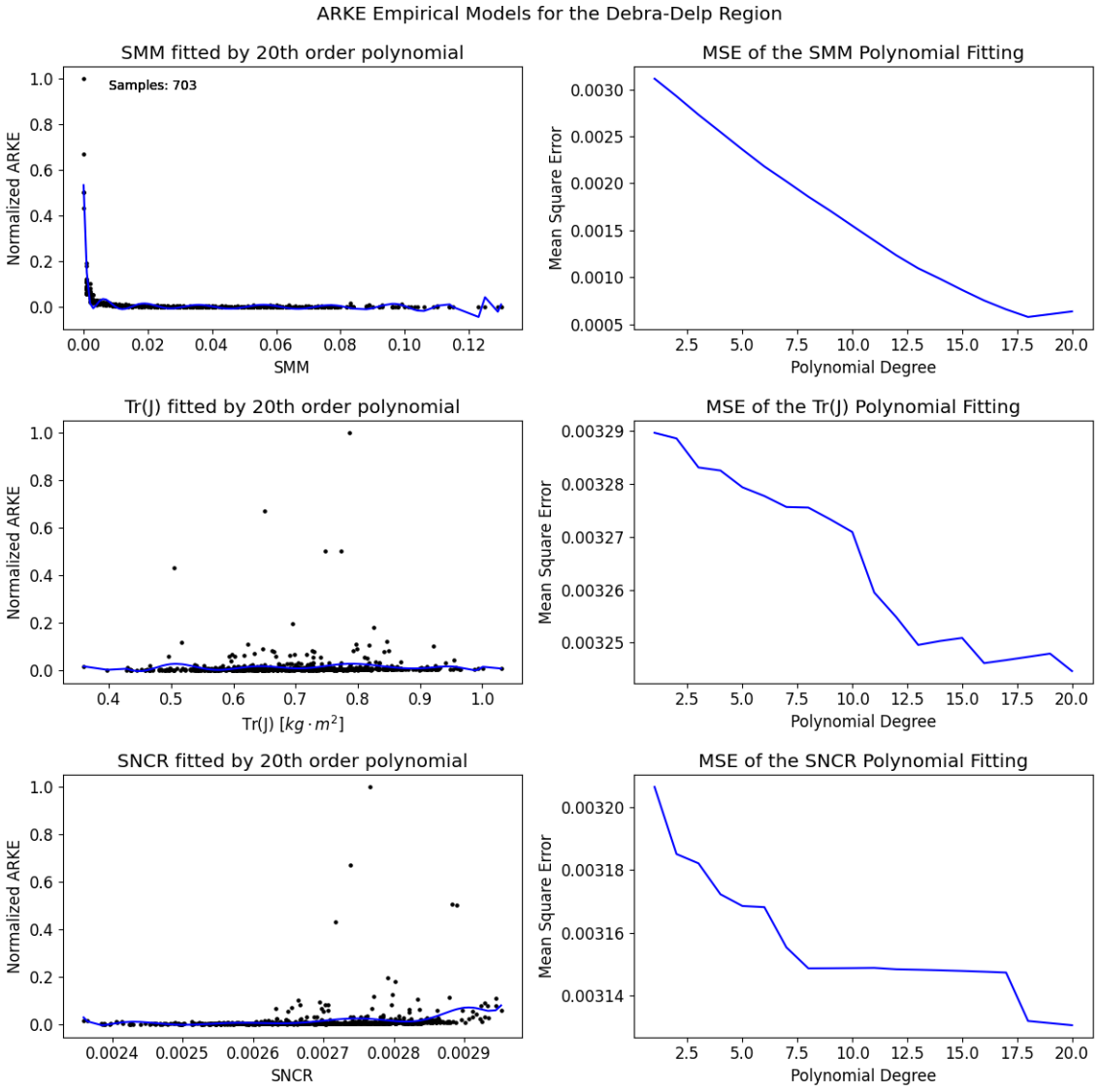

Figure 5.4. Normalized ARKE patterns for SMM, tr(J), and SNCR indices for the 12U configurations in the Debra-Delp region.

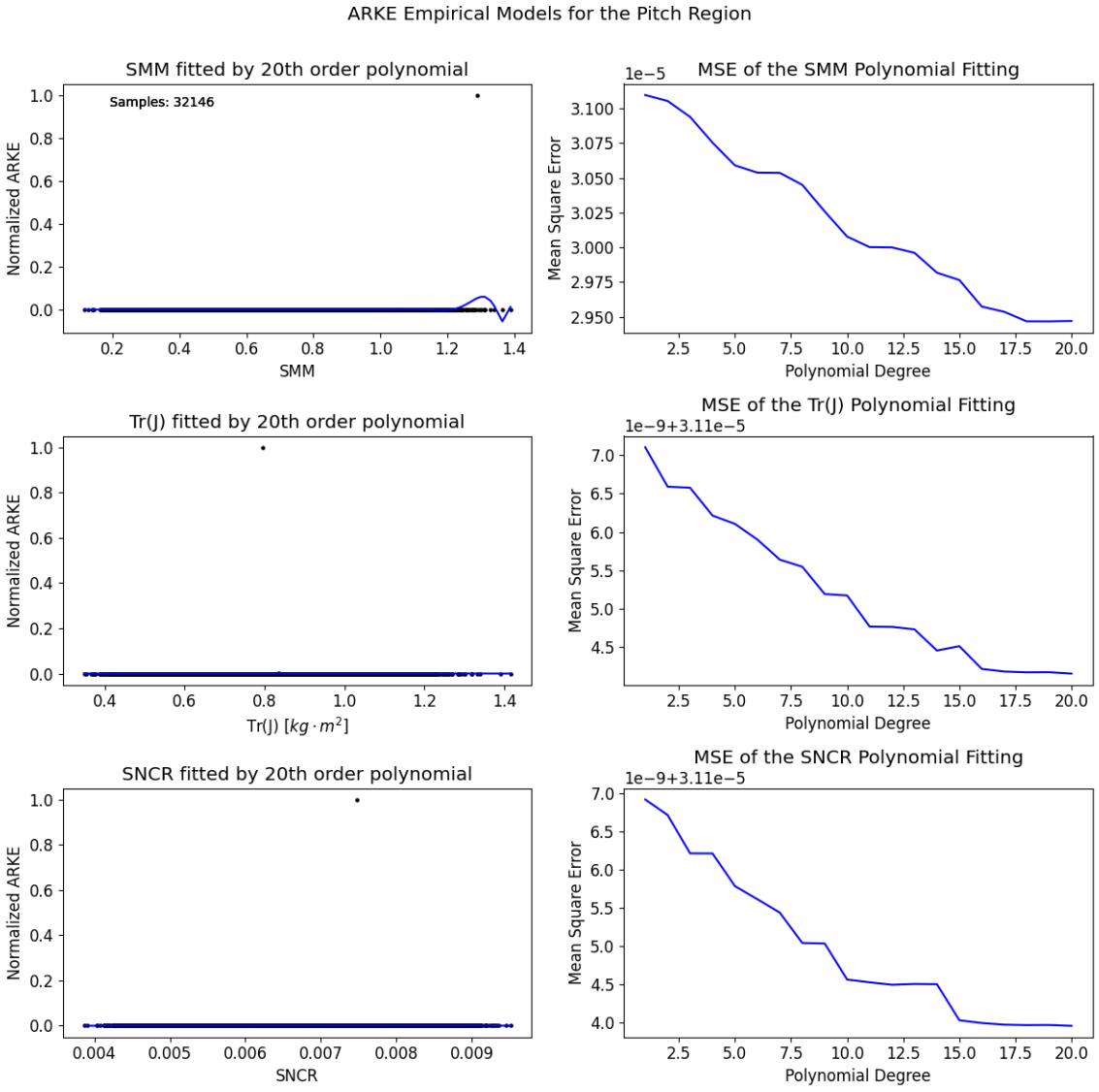

Figure 5.5. Normalized ARKE patterns for SMM, tr(J), and SNCR indices for the 12U configurations in the Pitch region.

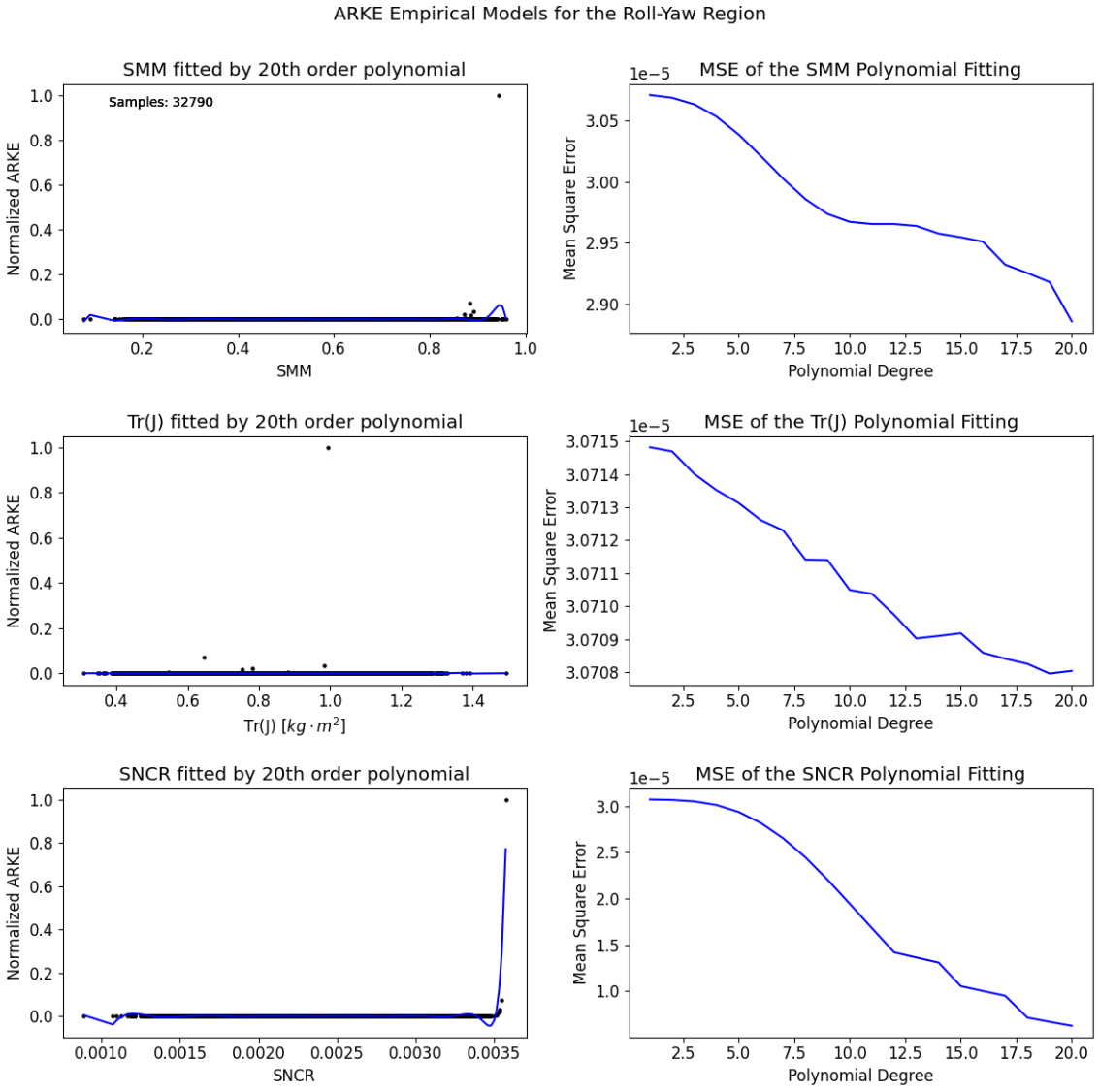

Figure 5.6. Normalized ARKE patterns for SMM, tr(J), and SNCR indices for the 12U configurations in the Roll-Yaw region.

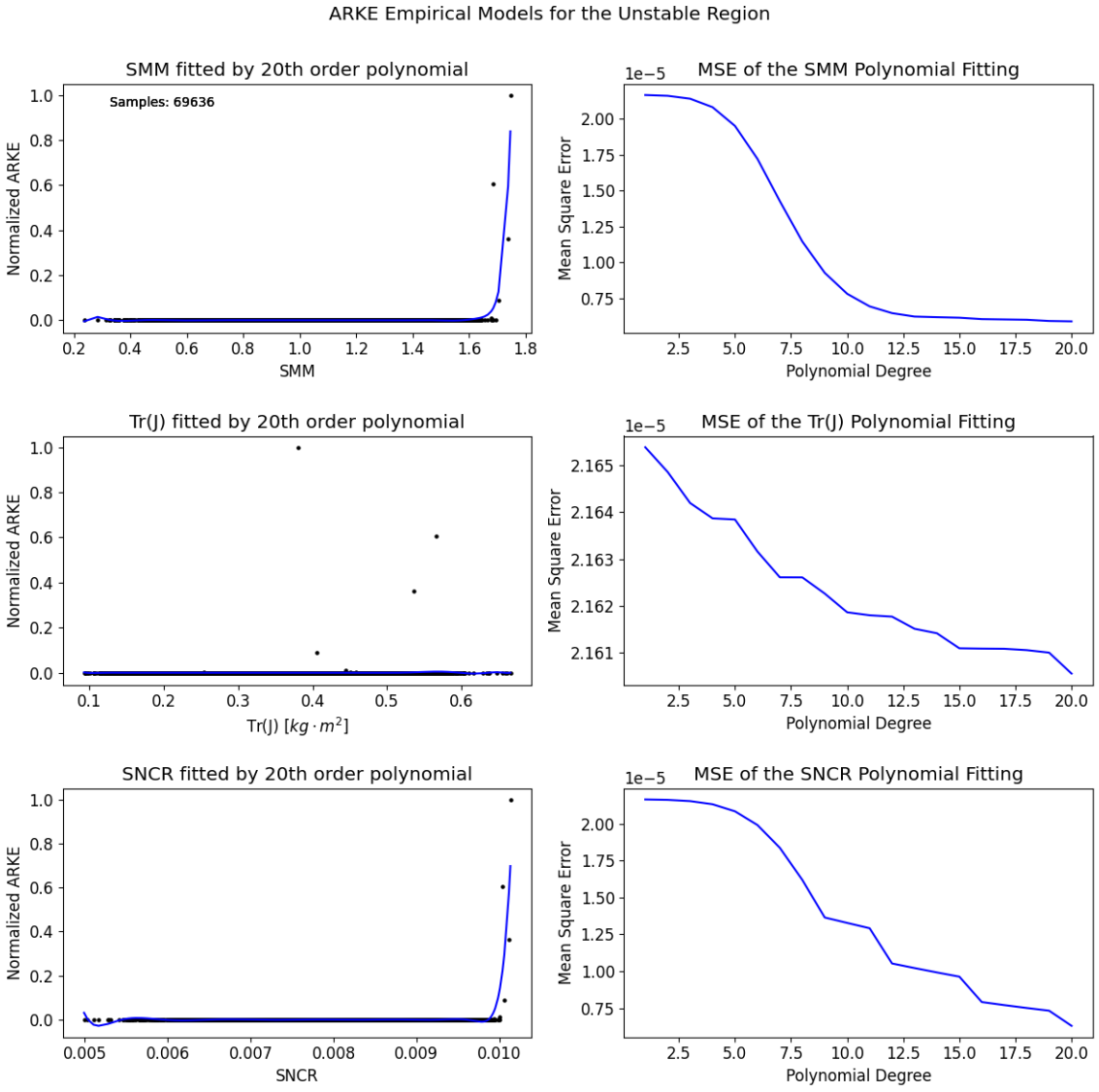

Figure 5.7. Normalized ARKE patterns for SMM, tr(J), and SNCR indices for the 6U configurations in the Unstable region.

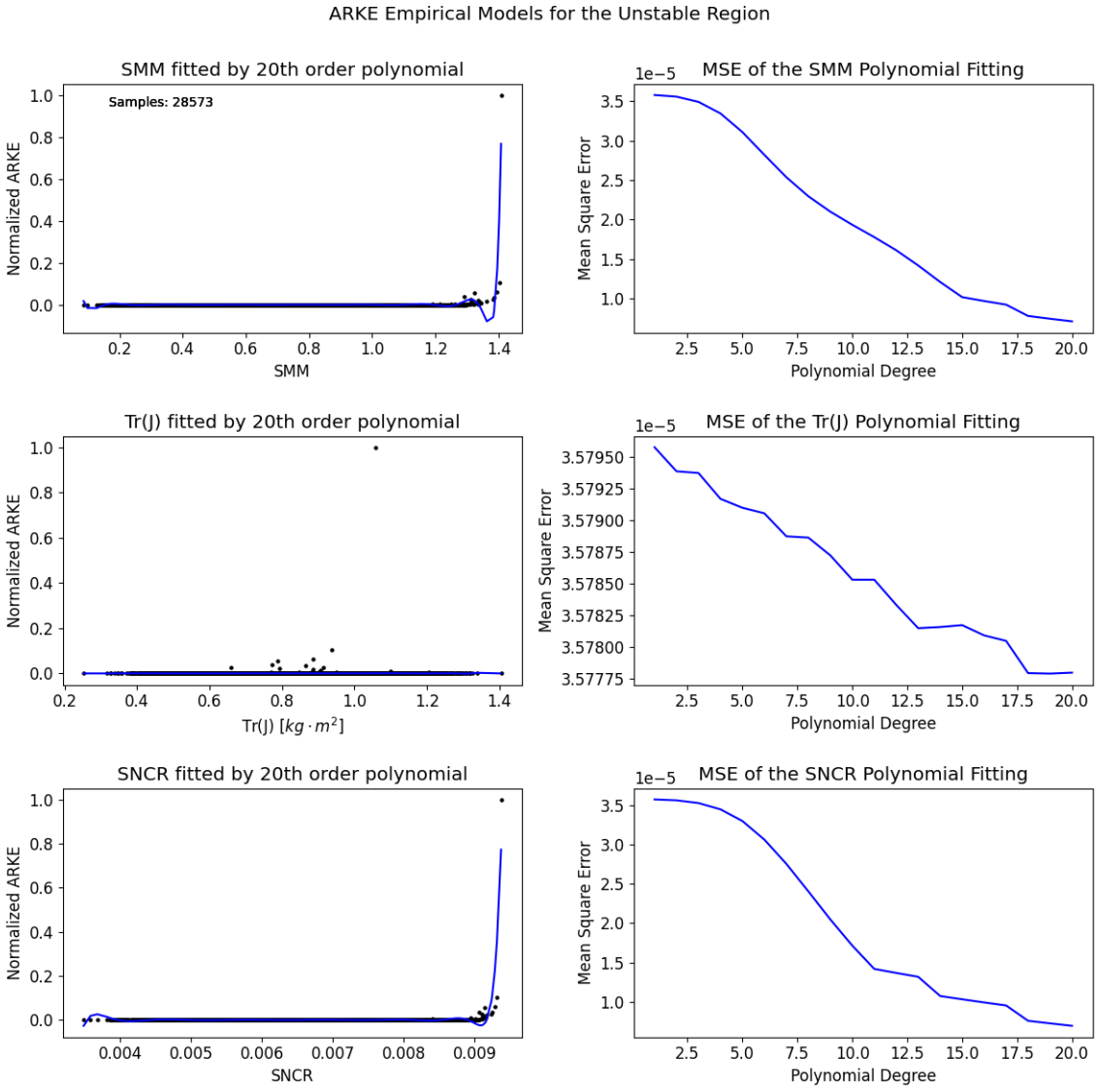

Figure 5.8. Normalized ARKE patterns for SMM, tr(J), and SNCR indices for the 12U configurations in the Unstable region.

5.2 DUMMY MASS GRID

For the dummy mass grid analysis we used the configurations presented in the LARKE column of the Table 4.7. According to Table 4.6, we generated 125 new designs from the original one, among them some with better GGS features. The number of new designs separated by region and dummy mass weight is presented in Table 5.3.

For designs originally belonging to the Lagrange region, at least one new configuration exhibited improved GGSM features. However, since this region is inherently three-axis stable, our analysis does not focus on it extensively. While an improved version may be desirable in some real-world design projects, it is not always advantageous to modify a statically stable project for another. Nevertheless, this method provides several viable options for enhancing GG stability features, if the need arises.

Considering the Debra-Delp region, although it is also three-axis stable, it is important to note that Debra-Delp configurations are gyrically stabilized. This characteristic can be affected if the mission design includes dampers in the ADCS. For this reason, the dummy mass grid offers valuable opportunities for GGSM enhancement, as demonstrated in at least one case from this study: the 3U CubeSat. For the 3U dummy mass grid, there are at least 17 improved design options in the Lagrange region. Figure 5.9 shows the potential locations for a 480g dummy mass to enhance stability design to the Lagrange region, represented by the green nodes.

For the Pitch region, we considered improved designs as those that achieve more than one stable axis, such as Lagrange, Debra-Delp, or Roll-Yaw. Analyzing Table 5.3, we observe between 9 and 41 potential improved designs with the addition of a mass representing 2% of the maximum weight allowed by the CubeSat standard.

From Table 5.3, it is evident that Lagrange-stable configurations can be achieved with dummy masses ranging from 2% to 10% of the maximum CubeSat weight. Such enhancements could mean expressive improvement in passive stabilization, analyzed further in this section. add

For the Roll-Yaw region, improved designs are those that achieve three stable axes, such as Lagrange and Debra-Delp. According to Table 5.3, achieving Lagrange stability is possible for nearly all CubeSat sizes with dummy masses ranging from 4% to 10% of the total system

mass. Additionally, numerous attitude improvements are achievable with Debra-Delp designs, considering missions without attitude dampers.

The 6U size was the only configuration that did not present region-improved options. However, some new Roll-Yaw designs showed better SNCR values than the original configuration. The best new design for the 6U size is detailed in Table 4.9, and its results are discussed in the following section of this chapter.

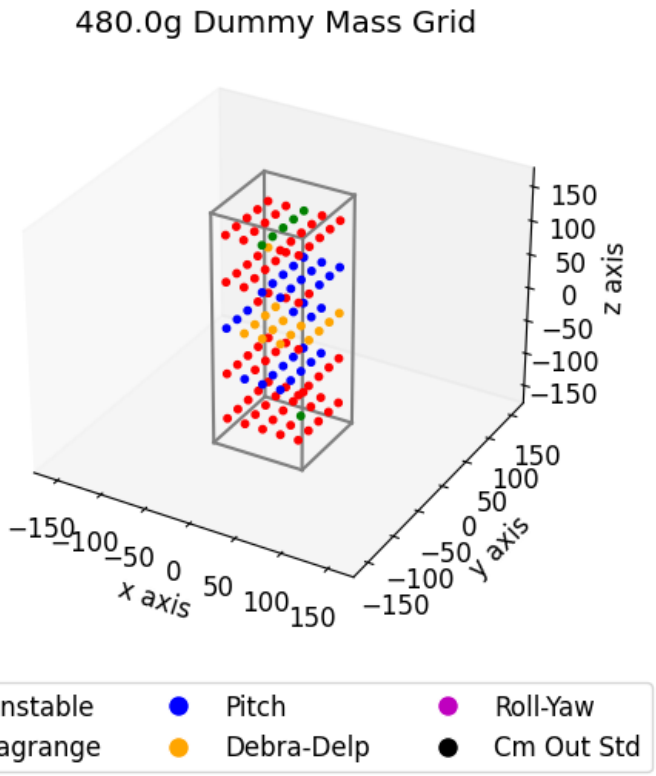

Figure 5.9. 480g dummy mass grid on the LARKE 3U CubeSat originally with Debra-Delp stability features.

Finally, for unstable configurations, we considered region-improved designs as those achieving any stable axis, including Lagrange, Debra-Delp, Roll-Yaw, or Pitch. For all CubeSat sizes, new designs belonging to the Lagrange region were identified. Furthermore, from 1U to 6U, Lagrange stability was achieved with the addition of a mass corresponding to 2% of the CubeSat's maximum weight. For the 12U size, Lagrange stability was achieved with a mass equivalent to 6% of the maximum weight, corresponding to a $5 \times 5 \times 5$ cm cube of lead, which would stabilize a 12U CubeSat effectively.

When propagating the attitude of the initial and best designs in open-loop, using the parameters described in Table 4.7, we observe significant improvements in the performance of the

best possible designs compared to the initial ones. These enhancements were anticipated, as the designs transition from an unstable to a stable GGSM region, considering only the passive stabilization provided by gravitational torque. The results, summarized in Table 5.2, demonstrate several cases where the attitude is exponentially improved with the addition of masses representing just 2% or 4% of the total system's mass.

This methodology can be particularly effective for missions without any active attitude control system (ADCS) but where stable attitude motion is still desirable. The case of semi-passive ADCS for these designs will be analyzed in the next section of this chapter. However, as we will show, the application of an attitude control system to a region-improved configuration does not always guarantee an enhancement in performance metrics.

Table 5.2. Initial and Improved designs features and performance metrics in of the open-loop system.

Size	Region		Total Systems Mass		Dummy Mass		Performance Metrics					
	Initial	Improved	Initial	Improved	Weight	Fraction	Peak-to-Peak Attittude Motion [°]	Initial Peak-to-Peak Angular Velocity [°/s]	ARKE in Open Loop [J]	Peak-to-Peak Attittude Motion [°]	Improved Peak-to-Peak Angular Velocity [°/s]	ARKE in Open Loop [J]
1U	Pitch	Debra-Delp	1920	2000	80	0.02	5.43e+4	5.62e+1	1.26e-4	4.55e+3	2.67e+0	5.27e-7
	Roll-Yaw	Lagrange	1840	2000	160	0.04	1.12e+13	6.16e+9	3.28e+11	3.70e+3	3.43e+0	6.54e-7
	Unstable	Lagrange	1920	2000	80	0.02	7.71e+18	6.73e+15	1.45e+23	3.21e+3	3.76e+0	4.23e-7
1.5U	Pitch	Lagrange	2760	3000	240	0.08	4.91e+3	4.71e+0	3.28e-6	3.64e+3	4.32e+0	2.05e-6
	Roll-Yaw	Lagrange	2700	3000	300	0.10	1.17e+17	9.06e+13	9.29e+19	3.76e+3	4.37e+0	1.94e-6
	Unstable	Lagrange	2940	3000	60	0.02	1.39e+18	1.16e+15	1.09e+22	3.58e+3	3.78e+0	1.03e-6
2U	Pitch	Debra-Delp	3680	4000	320	0.08	1.32e+5	1.38e+2	1.57e-3	3.85e+3	1.95e+0	1.19e-6
	Roll-Yaw	Lagrange	3760	4000	240	0.06	2.42e+15	1.65e+12	5.64e+16	5.95e+3	6.38e+0	6.14e-6
	Unstable	Lagrange	3840	4000	160	0.04	1.55e+17	1.21e+14	2.10e+20	3.97e+3	3.83e+0	1.87e-6
3U	Debra-Delp	Lagrange	5760	6000	240	0,04	7.17e+3	4.70e+0	5.21e-6	1.76e+3	3.00e+0	2.10e-6
	Pitch	Lagrange	5640	6000	360	0,06	4.35e+7	4.39e+4	1.25e+2	3.14e+3	3.59e+0	1.67e-6
	Roll-Yaw	Lagrange	5640	6000	360	0,06	2.47e+15	1.68e+12	5.50e+16	3.64e+3	4.47e+0	3.30e-6
	Unstable	Lagrange	5400	6000	600	0,10	5.98e+22	6.49e+19	5.33e+31	2.07e+3	3.07e+0	1.86e-6
6U	Pitch	Lagrange	11280	12000	720	0,06	8.33e+7	7.92e+4	2.90e+3	2.33e+3	3.34e+0	1.23e-5
	Roll-Yaw	Roll-Yaw	11760	12000	240	0.02	6.80e+15	4.79e+12	6.09e+18	5.08e+14	3.26e+11	3.16e+16
	Unstable	Lagrange	10800	12000	1200	0,10	4.20e+26	5.44e+23	1.36e+40	1.82e+3	3.08e+0	1.36e-5
12U	Pitch	Debra-Delp	21600	24000	2400	0,10	5.50e+3	5.25e+0	1.67e-4	3.21e+3	1.78e+0	3.87e-5
	Roll-Yaw	Lagrange	22560	24000	1440	0,06	1.34e+11	5.96e+7	2.40e+9	3.52e+3	3.63e+0	4.35e-5
	Unstable	Lagrange	22560	24000	1440	0,06	2.31e+13	1.31e+10	1.06e+14	4.01e+3	3.92e+0	5.80e-5

Table 5.3. Number of new designs generated by an original LARKE design for each GGSM region and cubesat size.

Original Design	New Designs	Dummy Masses for 1U					Dummy Masses for 1.5U					Dummy Masses for 2U				
		40g	**80g**	**120g**	**160g**	**200g**	**60g**	**120g**	**180g**	**240g**	**300g**	**80g**	**160g**	**240g**	**320g**	**400g**
Lagrange	Lagrange	36	19	11	10	9	36	14	8	5	6	21	10	6	3	0
	Debra-Delp	0	0	1	1	0	0	0	0	0	0	0	0	1	2	0
	Pitch	35	32	35	31	32	22	31	32	32	31	50	53	45	41	41
	Roll-Yaw	0	2	3	5	8	1	9	15	21	22	25	29	39	45	51
	Unstable	54	47	50	53	51	41	46	45	42	41	29	33	34	34	33
Debra-Delp	Lagrange	0	0	0	0	0	0	0	0	0	0	0	0	0	0	0
	Debra-Delp	113	91	74	61	49	74	45	29	20	15	44	28	16	12	8
	Pitch	12	34	43	45	44	44	47	43	36	32	81	74	65	56	45
	Roll-Yaw	0	0	8	19	30	4	13	18	21	23	0	12	23	27	33
	Unstable	0	0	0	0	2	3	20	35	48	55	0	11	21	30	39
Pitch	Lagrange	0	0	0	0	0	0	0	0	1	1	0	0	0	0	0
	Debra-Delp	20	20	10	9	4	24	27	17	9	7	0	8	10	9	6
	Pitch	67	34	28	23	22	79	55	41	31	24	80	52	39	32	26
	Roll-Yaw	4	12	23	29	33	0	8	17	26	31	41	47	51	53	59
	Unstable	34	34	39	39	41	22	35	50	58	62	4	18	25	31	34
Roll-Yaw	Lagrange	0	0	0	1	0	0	0	0	0	1	0	0	1	0	0
	Debra-Delp	10	16	9	8	5	6	9	11	7	6	27	22	17	9	6
	Pitch	0	6	15	12	13	1	12	21	26	26	31	36	39	46	48
	Roll-Yaw	100	75	58	45	41	108	86	72	73	70	67	67	68	68	68
	Unstable	15	28	43	59	66	10	18	21	19	22	0	0	0	2	3
Unstable	Lagrange	1	1	0	0	0	1	1	1	0	1	1	3	2	1	2
	Debra-Delp	7	10	7	5	3	2	14	10	11	6	1	7	7	4	7
	Pitch	26	22	17	8	10	36	39	33	25	23	30	33	29	24	15
	Roll-Yaw	4	13	27	23	25	25	25	39	47	55	24	30	38	50	55
	Unstable	87	79	74	64	62	61	46	42	42	40	69	52	49	46	46

Original Design	New Designs	Dummy Masses for 3U					Dummy Masses for 6U					Dummy Masses for 12U				
		120g	**240g**	**360g**	**480g**	**600g**	**240g**	**480g**	**720g**	**960g**	**1200g**	**480g**	**960g**	**1440g**	**1920g**	**2400g**
Lagrange	Lagrange	48	33	22	14	13	37	24	22	21	20	79	54	40	27	23
	Debra-Delp	0	0	0	0	0	0	0	0	2	0	0	0	0	0	0
	Pitch	1	5	6	10	10	5	11	12	11	13	22	33	35	39	39
	Roll-Yaw	0	0	0	2	5	0	0	0	0	0	0	0	0	0	1
	Unstable	76	87	97	99	97	58	45	46	46	47	24	38	50	59	62
Debra-Delp	Lagrange	0	1	5	6	5	0	0	0	0	0	0	0	0	0	0
	Debra-Delp	27	21	20	15	12	61	39	26	21	16	91	71	52	37	27
	Pitch	90	65	42	31	30	64	78	78	64	59	34	51	48	43	36
	Roll-Yaw	0	0	0	0	0	0	0	0	0	0	0	2	12	20	25
	Unstable	8	38	58	73	78	0	8	21	40	50	0	1	13	25	37
Pitch	Lagrange	9	3	2	1	0	0	0	1	0	3	0	0	0	0	0
	Debra-Delp	0	0	1	3	2	0	3	6	6	2	18	24	19	17	19
	Pitch	59	42	28	23	21	95	73	60	49	46	107	75	56	38	27
	Roll-Yaw	0	0	2	3	5	0	0	0	0	0	0	26	45	61	70
	Unstable	32	55	67	70	72	30	49	58	70	74	0	0	5	9	9
Roll-Yaw	Lagrange	0	1	1	3	4	0	0	0	0	0	0	0	1	0	0
	Debra-Delp	19	15	11	8	4	0	0	0	0	0	9	8	4	4	2
	Pitch	22	20	19	12	10	18	14	12	12	11	3	5	4	1	2
	Roll-Yaw	40	33	33	33	28	30	14	8	7	7	41	21	13	10	10
	Unstable	44	56	61	69	79	77	97	105	106	107	72	91	103	110	111
Unstable	Lagrange	11	14	12	10	8	17	18	17	16	17	0	0	1	0	0
	Debra-Delp	0	0	0	0	0	0	0	0	0	0	5	14	6	5	3
	Pitch	0	4	7	10	11	0	0	0	0	0	16	24	24	17	14
	Roll-Yaw	0	0	0	0	0	0	0	0	0	0	34	39	54	63	65
	Unstable	114	107	106	105	106	108	107	108	109	108	70	48	40	40	43

5.3 OPTIMIZATION OF THE SEMI-PASSIVE ACTUATION

In this section, we discuss the simulations concerning the use of semi-passive ADCS: regulation control with reaction wheels and magnetorquers, alongside the GGS. First, we compare the attitude and control performance of the ARKE and LARKE configurations from the same stability region, followed by a comparison between the initial and region-improved designs.

Improvements are observed in almost all cases in the HARKE and LARKE pairs. Starting with the percent decrease in transient periods, we find that as the CubeSat size increases, LARKE configurations exhibit shorter transient periods compared to HARKE designs. However, some exceptions arise, such as all 1.5U, unstable 1U, and Debra-Delp 2U and 3U pairs, where LARKE designs show percent increases over HARKE. Nevertheless, in the majority of HARKE-LARKE pairs, LARKE configurations outperform HARKE in terms of transient period.

For the ARKE in closed-loop metric, the vast majority of pairs display significant percent decreases, with values approaching 100% improvement in Lyapunov function values, such as for the 3U Lagrange, Pitch, and Roll-Yaw cases. In other cases, improvements range from 12.8% to 94%. Only one case, a percent increase of 1%, is observed, which is negligible compared to the other 29 cases.

Regarding peak-to-peak attitude motion, percent decreases of up to 90% are observed for LARKE compared to HARKE configurations, particularly in the 3U Roll-Yaw and Lagrange regions. Out of 30 HARKE-LARKE pairs, only one case—a 1U Pitch configuration—shows a percent increase in peak-to-peak attitude motion. This result is particularly relevant for missions requiring high-precision pointing.

The pattern of percentage decrease in peak-to-peak angular velocity becomes less pronounced, with 17 out of 30 cases showing better performance for the LARKE design compared to the HARKE design, and 13 cases showing the opposite. However, the observed differences are smaller compared to other metrics.

Moving to control metrics, the peak-to-peak control torque applied to the system shows improvements in two-thirds of the cases for LARKE relative to HARKE configurations, although with smaller percent decreases compared to other performance metrics. Nonetheless,

the average control torque applied during actuation presents higher percent decrease values in 29 out of 30 cases. These percentages reach 94% and 95% for the 3U Lagrange and Roll-Yaw cases, respectively, and range from 25% to 90% in most cases. One modest improvement of 1% is observed for the unstable LARKE 1.5U design, and a 14% increase in mean control torque is noted for the 1U LARKE Pitch configuration compared to HARKE. These results suggest a potential economy in power consumption by the attitude control system over the mission lifecycle.

For actuator performance metrics, the peak-to-peak angular momentum of the reaction wheels shows consistent improvements for LARKE systems compared to HARKE, with 29 out of 30 cases exhibiting enhancements. Improvements range from 12% for the 1.5U unstable pair to 94% for the 3U Roll-Yaw pair. These metrics can help analyze and set the actuator requirements and justify the choice of one, in the case of the reaction wheels use.

Lastly, the peak-to-peak magnetic moment generated by the magnetorquer shows less pronounced but still consistent improvements. Notably, designs with at least one unstable axis exhibit the largest improvements, ranging from 22% to 58%.

The second analysis involving the application of the regulation control system compares the initial configurations with the improved configurations derived from the dummy mass grid. From Table 5.5, it is evident that most metrics show a percent increase. Even in cases where a decrease is observed, the values are minimal in the majority of cases.

The transient period metric is the only one that predominantly shows improvements, with 12 out of 19 cases presenting better results. However, the percentage improvements are not significant. These findings suggest that the dummy mass grid approach may not offer substantial advantages for projects with active attitude control systems.

As indicated by the results in Table 5.5, adding mass to create more stable GGS configurations does not necessarily translate to improved attitude and control performance metrics for closed-loop systems.

Table 5.4. Percent decrease of HARKE to LARKE configurations in attitude and control performance metrics.

Size	GGSM Region	Transient Period [%]	ARKE in Closed-Loop [%]	Peak-to-Peak Attittude Motion [%]	Peak-to-Peak Angular Velocity [%]	Peak-to-Peak Control Torque [%]	Mean Control Torque [%]	Peak-to-Peak Reaction Wheel Angular Momentum [%]	Peak-to-Peak Magnetorquer Magnetic Moment [%]
1U	Lagrange	1.61	77.55	70.29	5.87	1.07	72.64	75.55	-6.19
	Debra-Delp	0.38	91.65	81.01	9.07	2.28	84.99	85.98	4.49
	Pitch	-5.97	-1.09	-10.41	-0.99	-0.49	-14.34	-13.83	29.43
	Roll-Yaw	-51.59	47.21	28.35	-8.47	-0.92	34.79	38.93	44.22
	Unstable	-5.72	52.01	37.49	-5.04	-0.34	38.22	46.02	40.46
15U	Lagrange	-5.53	91.97	80.06	11.81	4.99	86.34	86.19	5.17
	Debra-Delp	-4.04	56.93	48.11	4.4	1.18	51.38	54.94	5.3
	Pitch	-6.41	87.49	61.8	9.29	6.3	73.28	69.87	34.22
	Roll-Yaw	-28.34	72.24	53.97	-9.16	-1.09	61.12	64.86	46.77
	Unstable	-6.23	12.8	5.58	-7.6	-0.73	1.04	12.41	42.26
2U	Lagrange	15.08	94.19	83.59	14.57	8.33	89.15	89.15	25.05
	Debra-Delp	-8.7	66.97	48.7	5.06	1.68	56.92	56.35	1.92
	Pitch	30.07	84.08	60.53	9.64	9.33	70.71	67.56	37.06
	Roll-Yaw	17.97	79.5	62.19	-9.5	-1.23	69.65	72.17	47.93
	Unstable	22.1	89.25	72.33	-6.94	-1	80.74	80.92	49.29
3U	Lagrange	64.27	97.95	88.87	20.91	29.79	94.49	93.43	40.04
	Debra-Delp	-8.11	67.96	48.6	5.45	2.09	57.01	56.8	2.88
	Pitch	52.65	96.3	81.69	17.04	21.95	90.41	87.7	38.95
	Roll-Yaw	64.63	98.2	89.81	-2.62	9.46	95.14	94.45	62.35
	Unstable	50.31	94.76	82.55	-7.2	-0.93	88.86	88.43	56.09
6U	Lagrange	30.55	70.87	55.43	8.42	8.01	60.2	62.33	25.43
	Debra-Delp	69.92	84.7	63.84	11.18	19.21	74.19	71	19.31
	Pitch	31.01	52.88	27.92	4	14.84	39.36	33.83	31.88
	Roll-Yaw	29.59	31.17	19.69	-15	-5.68	25.55	22.53	35.94
	Unstable	61.86	88.66	73.13	-4.11	-0.56	80.38	79.88	56.79
12U	Lagrange	40.76	69.21	49.21	7.73	14.48	57.44	56.27	13.59
	Debra-Delp	16.45	57.74	38.81	5.73	11.37	47.19	45.25	8.75
	Pitch	40.3	36.89	24.46	3.42	10.8	31.64	29.63	22.63
	Roll-Yaw	47.56	72.39	46.5	-11.45	1.98	63.23	57.07	58.26
	Unstable	41.06	63.05	43.26	-4.87	6.25	56.14	54.43	57.73

5.4 POWER GENERATION AND ATTITUDE MOTION

In this section, we present the analysis of power generation under the influence of different attitude motions corresponding to the GGSM regions. These results are also presented and discussed in Avelino *et al.* (2024), which is one of the publications derived from this research. The analysis involved propagating the attitude motion of each configuration listed in Table 4.10 and subsequently simulating the power generation using the STK software. The simulations were conducted for one day, from the 15th to the 16th of each month throughout the year, and then the annual average power generation was calculated.

Table 5.5. Initial and Improved designs performance metrics for the closed-loop system.

Size	Initial Design GGSM Region	Improved Design GGSM Region	Transient Period [%]	ARKE in Closed-Loop [%]	Peak-to-Peak Attittude Motion [%]	Peak-to-Peak Angular Velocity [%]	Peak-to-Peak Control Torque [%]	Peak-to-Peak Reaction Wheel Angular Momentum [%]	Peak-to-Peak Magnetorquer Magnetic Moment [%]
1U	Pitch	Debra-Delp	0.61	-8.68	-3.28	-0.22	-0.05	-3.99	-0.06
	Roll-Yaw	Lagrange	1.46	-17.56	-15.65	-0.99	-0.25	-19.26	-0.17
	Unstable	Lagrange	-1.11	-30.78	-29.43	-1.28	-0.2	-34.83	-0.21
15U	Pitch	Lagrange	0.52	-52.47	-22.16	-1.76	-0.67	-28.9	-1.37
	Roll-Yaw	Lagrange	3.94	-53.43	-49.41	-3.16	-0.99	-64.55	-0.57
	Unstable	Lagrange	0.61	-14.22	-17.16	-1.03	-0.24	-20.99	-0.14
2U	Pitch	Debra-Delp	0.62	-8.66	-4.61	-0.32	-0.09	-5.67	-0.05
	Roll-Yaw	Lagrange	4.51	-27.43	-37.81	-2.63	-0.88	-49.35	0.22
	Unstable	Lagrange	1.85	-10.19	-15.27	-1.04	-0.29	-19.02	-0.06
3U	Debra-Delp	Lagrange	0.13	-54.85	6.26	0.6	0.27	8.04	-0.12
	Pitch	Lagrange	-0.12	-15.03	4.86	0.33	0.08	5.85	-0.4
	Roll-Yaw	Lagrange	3.88	-93.34	-80.85	-4.13	-1.06	-105.29	-0.79
	Unstable	Lagrange	-0.38	-32.47	-0.31	-0.02	-0.01	-0.3	0.51
6U	Pitch	Lagrange	-51.77	-83.99	-22.42	-2.22	-2.08	-27.28	-7.27
	Roll-Yaw	Roll-Yaw	32.89	-4.33	-2.08	-0.46	-0.36	-2.54	-0.23
	Unstable	Lagrange	3.81	-19.47	-1.32	-0.12	-0.18	-1.31	2.67
12U	Pitch	Debra-Delp	-0.86	-10.39	-2.55	-0.3	-0.43	-3.12	-1.17
	Roll-Yaw	Lagrange	-4.26	-25.8	-17.31	-1.83	-2.15	-21.04	-2.1
	Unstable	Lagrange	-2.13	-12.19	-10.89	-1.21	-1.6	-13.23	-1.03

Table 5.6. Annual average power generation across all GGSM regions and CubeSat sizes from 1U to 6U.

Size	Average Annual Power Generation $[Wh]$				
	Lagrange	Debra-Delp	Pitch	Roll-Yaw	Unstable
1U	46.35	46.14	46.28	46.12	46.04
1.5U	74.06	74.61	74.20	74.61	74.50
2U	105.61	103.56	104.12	105.61	105.55
3U	131.08	130.35	129.02	130.92	131.10
6U	328.64	328.30	328.04	325.37	324.32

Table 5.7. Best and worst case scenarios for the annual average power generation across all GGSM regions and CubeSat sizes from 1U to 6U, presenting the generated power values, absolute differences, and percent differences. Source: Adapted from Avelino *et al.* (2024).

Sizes	Best-Case		Worst-Case		Difference $[Wh]$	Percent Difference [%]
	Region	Annual Average Generated Power $[Wh]$	Region	Annual Average Generated Power $[Wh]$		
1U	Lagrange	46.53	Unstable	46.04	0.31	0.66
1.5U	Debra-Delp Roll-Yaw	74.61	Lagrange	74.06	0.55	0.75
2U	Lagrange Roll-Yaw	105.61	Debra-Delp	103.56	2.05	1.96
3U	Unstable	131.10	Pitch	129.02	2.08	1.60
6U	Lagrange	328.64	Unstable	324.32	4.32	1.32

Table 5.6 presents the annual average power generation values for each CubeSat size across the GGSM regions. Analyzing these results, it becomes evident that the fluctuations in annual average power generation across different GGSM regions are minimal.

For the 1U size, the Lagrange configuration achieved the highest power generation; however, the difference from the worst-case scenario, the Unstable configuration, was only 0.31 Wh. Similarly, for the 1.5U size, the best-case scenarios, Debra-Delp and Roll-Yaw, exhibited just a 0.55 Wh difference from the worst-case scenario, Lagrange. For the 2U size, the difference between the best configurations, Lagrange and Roll-Yaw, and the worst, Debra-Delp, was 2.05 Wh. In the 3U configurations, the Unstable case generated 2.08 Wh more than the worst-case scenario, Pitch. Finally, for the 6U size, the Lagrange configuration produced 4.32 Wh more than the Unstable configuration.

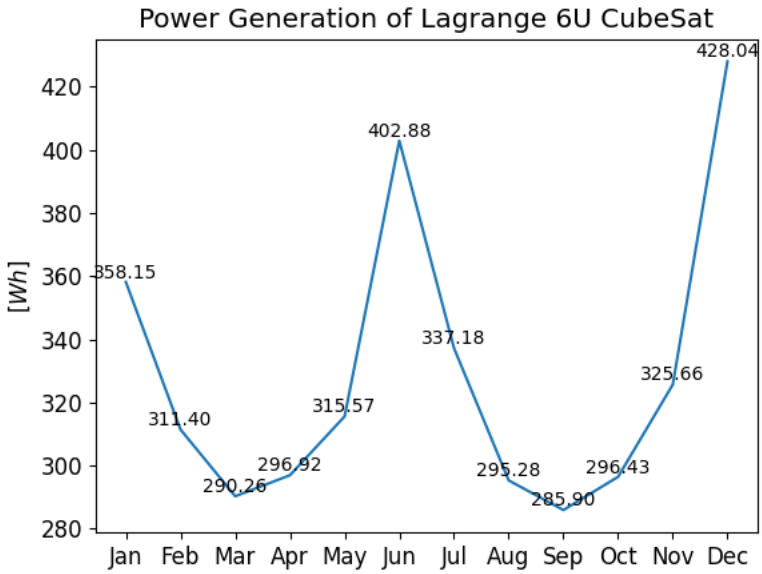

Figure 5.10. Monthly power generation pattern of a 6U CubeSat with Lagrange stability. Source: Avelino *et al.* (2024)

A summary of these findings, along with the percent differences between the best and worst scenarios, is provided in Table 5.7. These results reveal no distinct pattern or significant advantage in power generation was observed for any specific GGSM region. The attitude motion of GG-stabilized CubeSats resulted in nearly uniform power generation across all GGSM regions.

In addition, we analyzed the sun incidence periods for each CubeSat face across all GGSM regions during the months with the highest (December) and lowest (September) solar exposure, corresponding to the 500 km LEO polar orbit, as described in Table 4.10. As shown in Figure 5.11 and Figure 5.12, while fluctuations in the dperiods of sun incidence on individual

CubeSat faces were observed, the overall exposure across all faces did not reveal any privileged GGSM region.

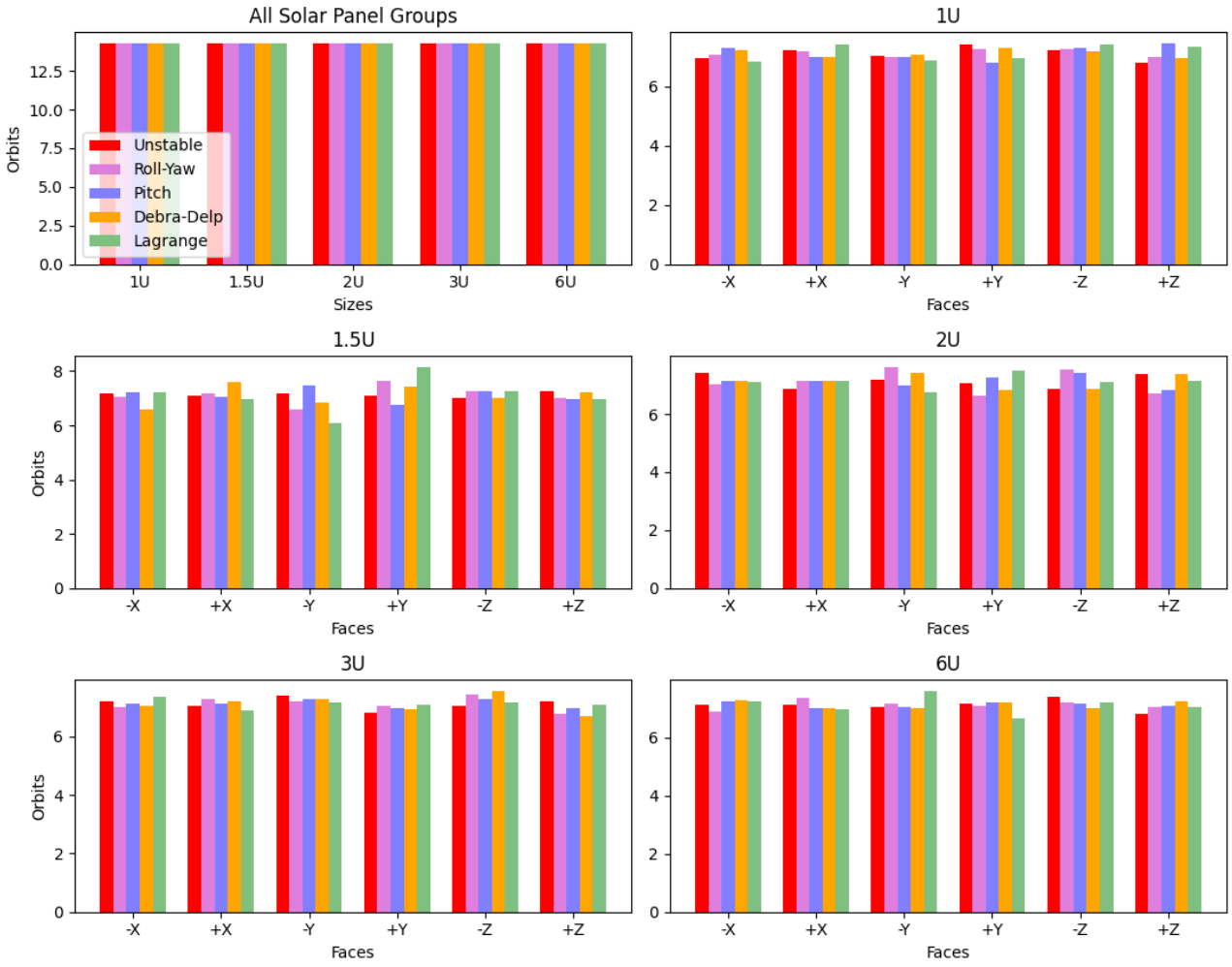

Figure 5.11. Period of solar exposure for each size and stability region in the month of maximum sun incidence - December. Source: Avelino *et al.* (2024)

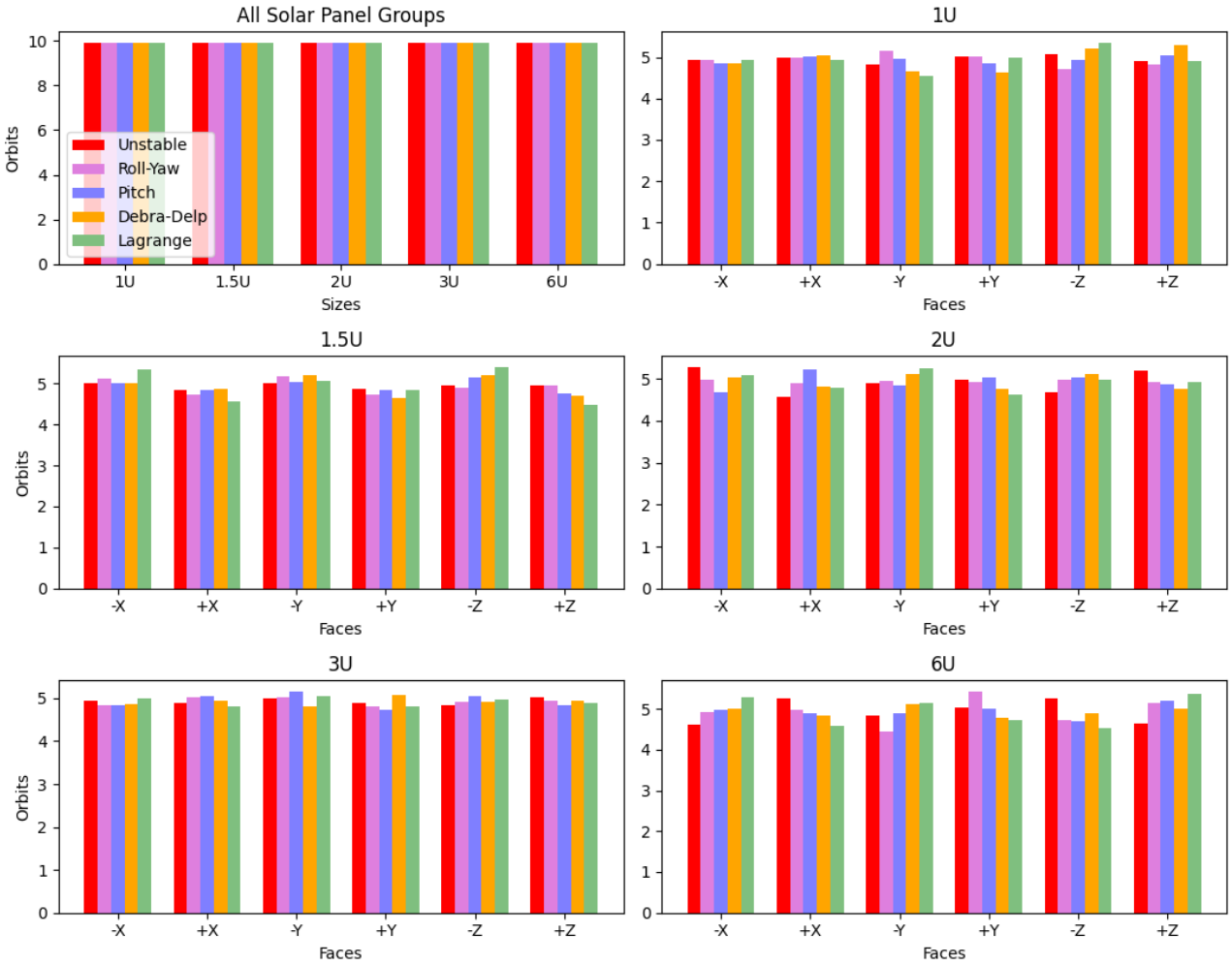

Figure 5.12. Periods of solar exposure for each size and stability region in the month of minimum sun incidence - September. Source: Avelino *et al.* (2024)

CHAPTER 6

CONCLUSION

In this research, we conducted an investigation into the attitude dynamics of spacecraft, specifically focusing on gravity-gradient stabilization (GGS) within the CubeSat standard. Our study revealed that mechanical designs adhering to the CubeSat Design Specification (CDS) (JOHNSTONE, 2022) can exhibit inertia ratios spanning any of the five stability regions of the Gravity-Gradient Stability Map (GGSM). The development of a empirical stability index model based on kinetic energy patterns has proven to be a valuable tool for designers in identifying optimal configurations for spacecraft attitude dynamics. This approach facilitates the achievement of a three-axis stable Lagrange configuration, which is crucial during the design phase. Furthermore, the analysis of improved designs based on GGS principles has demonstrated enhanced attitude and control performance, validating the effectiveness of this methodology in refining spacecraft stability and control.

We began by reviewing the fundamentals of attitude dynamics, including attitude representations, kinematics, and dynamics. The Euler angles and attitude matrix were defined as the primary representations used throughout this work. We also established the reference frames and derived the foundational equations for attitude dynamics, culminating in Euler's rotational equation. Furthermore, we introduced equations for key spacecraft torques, including gravitational torque, magnetic torque, and the internal torque generated by reaction wheels.

In formulating the problem, we reviewed the theoretical basis for gravity-gradient stabilization, presenting the equations governing attitude kinematics and dynamics. The study included a linear approximation achieved by system linearization through the Jacobian matrix and an analysis of the relative equilibrium state. We extended this analysis by examining the fundamentals of stability in linearized systems, addressing asymptotic and Lyapunov stability, the stability requirements for conservative and gyric systems, and their specific application to GGS. This process led to the derivation of the Gravity-Gradient Stability Map (GGSM).

The methodology defined the rigid body model based on CubeSat Design Specifications (JOHNSTONE, 2022) and detailed the implementation of the body and attitude dynamics in an object-oriented, Python-based framework. We also introduced a simple feedback control law and outlined performance metrics used for result evaluation. Subsequently, we developed empirical models of stability based on average rotational kinetic energy (ARKE) patterns from simulated CubeSat samples.

To investigate ARKE patterns, we proposed three empirical stability index models: the Stability Map Margin (SMM), the trace of the MOI tensor in the principal axis frame (Tr(J)), and the sum of the norm of the characteristic roots of the state matrix (SNCR). These indices were derived to identify and analyze ARKE patterns across the GGSM regions. Additionally, we proposed the Dummy Mass Grid method to enhance initial designs by adding a dummy mass at strategic locations to improve stability features. This method enabled us to explore better configurations systematically. The methodology concluded with diagrams and parameters for the simulations used to investigate the study's primary goals. These simulations included ARKE, Dummy Mass Grid, regulation control, and attitude motion and power generation analyses.

The ARKE simulation explored ARKE patterns using empirical stability indices, applying least squares polynomial fitting and mean square error (MSE) as a performance metric. The Dummy Mass Grid simulation investigated potential design enhancements and evaluated their performance. The regulation control simulations analyzed performance metrics for HARKE and LARKE configurations from the ARKE simulation, as well as initial and best designs derived from the Dummy Mass Grid. Lastly, the attitude motion and power generation simulations provided insights into the relationship between GGS-induced attitude dynamics and CubeSat power generation.

One of the main findings of this work was the evaluation of empirical models for stability indices based on ARKE patterns within the GGSM regions. Using the Least Squares Polynomial Fit (LSPF) and Mean Squared Error (MSE) as metrics, we validated the performance of the proposed models - SMM, Tr(J), and SNCR.

For the Lagrange region, the Tr(J) model emerged as the best-suited stability index for CubeSat sizes from 1.5U to 6U, as it consistently achieved the lowest MSE for these sizes.

However, for the 1U and 12U sizes, the SMM model outperformed Tr(J), particularly for the 12U size, where the SMM MSE was five times smaller, indicating its suitability for larger configurations. The empirical models for the Lagrange region achieved MSE of order 10^{-3} and 10^{-4}.

The SMM model also proved to be the most effective stability index for the Debra-Delp and Pitch regions, achieving MSE orders between 10^{-4} and 10^{-7}. ARKE patterns showed strong alignment with the SMM model for these regions, particularly as designs approached more stable regions like Lagrange or Debra-Delp, as supported by heatmaps and polynomial fittings.

For the Roll-Yaw region, the SNCR model demonstrated superior performance across all CubeSat sizes, with MSE values often three times smaller than other indices and raging from 10^{-4} and 10^{-5}, further validating its dominance in this region. Similarly, the SMM model excelled in the unstable region, with MSE orders of 10^{-5} and 10^{-6}. Even for cases where SNCR had slightly better MSE, such as the 12U size, the minimal difference confirmed the versatility of the SMM model as a reliable stability index. These results underline the robustness of the proposed empirical models and their alignment with ARKE patterns, offering valuable insights for selecting optimal stability indices during CubeSat design.

Another contribution of this work is the Dummy Mass Grid methodology, which systematically explores adding dummy masses to CubeSat configurations to enhance GGSM stability features. This approach demonstrated the potential to transform initial designs into improved configurations with better stability across multiple regions.

Although inherently three-axis stable for the Lagrange region, enhancements were viable with the search for a configuration with lower ARKE, which was beneficial for specific design scenarios. In the Debra-Delp region, improvements are particularly relevant for missions involving ADCS configurations with dampers, highlighting the value of the Dummy Mass Grid for achieving static stable designs, with masses from 4% to 10% of the total system's mass for the 3U cases.

In the Pitch region, adding small dummy masses enabled configurations with multiple stable axes, improving passive stabilization potential. Similarly, for the Roll-Yaw region, Lagrange and Debra-Delp stability were achieved for most CubeSat sizes, although the 6U size showed improvements in other stability metrics without region changes.

For initially unstable configurations, the method proved highly effective, enabling transitions to stable regions such as Lagrange, even with minimal mass additions. Notably, masses as small as 2% to 6% of the CubeSat's total weight significantly enhanced stability.

Open-loop attitude propagation of initial and improved designs demonstrated exponential performance enhancements for configurations transitioning from unstable to stable GGSM regions through passive stabilization. This methodology is particularly advantageous for missions lacking active ADCS, where stabilized attitude motion is desirable. However, subsequent analyses revealed that while region improvements enhance passive stabilization, they do not always translate directly to better performance metrics when active ADCS is applied.

This research also analyzed the use of semi-passive ADCS systems, combining regulation control with reaction wheels and magnetorquers alongside GGS. The comparison of HARKE and LARKE configurations demonstrated significant improvements in most metrics, particularly for transient periods, Lyapunov function values, and peak-to-peak attitude motion. LARKE configurations generally outperformed HARKE, with shorter transient periods as CubeSat sizes increased, and reductions in peak-to-peak attitude motion reaching up to 90%, making them particularly valuable for missions requiring precise pointing.

Control metrics further highlighted the advantages of LARKE configurations, with substantial decreases in average control torque, reaching up to 94% in some cases, suggesting potential power savings over the mission lifecycle. Actuator performance metrics, such as the angular momentum of reaction wheels and the magnetic moment of magnetorquers, showed consistent improvements for LARKE, supporting their effectiveness in optimizing ADCS requirements.

However, when comparing initial and region-improved configurations derived from the Dummy Mass Grid, the results indicated minimal benefits for closed-loop systems. While transient period metrics showed improvements in some cases, the overall percentage changes were not significant. These findings suggest that while region improvements enhance passive stabilization, they may not always provide substantial advantages in projects with active attitude control systems.

Considering the power generation analysis, this research revealed that the attitude motion of GG-stabilized CubeSats does not significantly impact power generation or solar incidence behavior. Across CubeSat sizes and GGSM regions, the annual average power generation

exhibited minimal fluctuations, with percentage differences between the best and worst cases ranging from 0.66% to 1.96%. Additionally, the analysis of sun incidence periods showed no privileged GGSM region for maximizing solar exposure. These findings suggest that the attitude motion induced by GGS provides consistent power generation performance across all GGSM regions, simplifying CubeSat mission planning and design when considering the EPS performance in missions with no active ADCS.

This work provided a comprehensive understanding of how gravity-gradient stabilization (GGS) influences stability across different CubeSat form factors by exploring the ARKE patterns of the proposed empirical stability indices. The direct application of these findings can significantly impact subsystem placement strategies, offering insights into the optimal positioning of components or the use of dummy masses to enhance stability through the Dummy Mass Grid methodology. Additionally, this work explored the integration of GGS with magnetorquers and reaction wheels, evaluating potential advantages and disadvantages when employing hybrid attitude control systems. Lastly, the study investigated the influence of attitude motion on power generation and concluded that, within the CubeSat standard, power generation remains consistent regardless of attitude motion from any GGSM region.

For future work, a primary improvement would be the inclusion of atmospheric drag in the attitude analysis, as this external torque plays a significant role in the attitude dynamics of satellites in low Earth orbit (LEO). Expanding the analysis to incorporate other environmental torques, such as solar radiation pressure and geomagnetic disturbances, could offer a more comprehensive understanding of CubeSat attitude behavior. Examining the influence of these torques on the proposed stability indices and control strategies would enhance the robustness of the methodology and strengthen the design recommendations.

Furthermore, applying the Dummy Mass Grid methodology in real CubeSat design processes, while accounting for practical considerations like manufacturability and mass budget constraints, would help bridge the gap between theoretical modeling and practical implementation. Future studies could also focus on refining control algorithms and integrating environmental torques into system modeling for semi-passive ADCS configurations, thereby approaching real scenarios and maximizing the reliability and performance benefits highlighted in this research.

Finally, experimental validation through hardware-in-the-loop simulations or on-orbit demonstrations would be invaluable. Such efforts would provide deeper insights into the real-world effectiveness of the proposed models and strategies, paving the way for more reliable and successful CubeSat missions.

6.1 PUBLISHED AND ACCEPTED PAPERS

This section lists the published and accepted papers that are directly or indirectly associated with this research.

- AVELINO *et al.*. The Impact of Gravity-Gradient Stabilization on ADCS Efficiency and Design Optimization in CubeSats. In: *IEEE Aerospace Conference*, Big Sky, Montana, 2025. ACCEPTED.

- AVELINO *et al.*. Analysis of the influence of gravity-gradient torque on power generation in the cubesat standard. In: *75th International Astronautical Congress*, Milan, 2024. PUBLISHED.

- BORGES *et al.*. Perception data system for satellite monitoring of strategic assets. In: *75th International Astronautical Congress*, Milan, 2024. PUBLISHED.

- BORGES *et al.*. The AlfaCrux CubeSat Mission Description and Early Results. *Applied Science*, 2022. PUBLISHED.

BIBLIOGRAPHY

ALKEN, P. *et al.* Evaluation of candidate models for the 13th generation international geomagnetic reference field. *Earth, Planets and Space*, v. 73, n. 1, p. 48, Feb 2021. Cited in pages 47.

ALKEN, P. *et al.* International geomagnetic reference field: the thirteenth generation. *Earth, Planets and Space*, v. 73, n. 1, p. 49, Feb 2021. Cited in pages 47.

AMJADIFARD, R. *et al.* Estimation of solar panels available power for a leo satellite in detumbling mode based on monte carlo analysis. *IEEE Aerospace and Electronic Systems Magazine*, v. 34, n. 5, p. 4–11, 2019. Cited in pages 4.

ANIGSTEIN, P. *et al.* Analysis of solar panel orientation in low altitude satellites. *Aerospace and Electronic Systems, IEEE Transactions on*, v. 34, p. 569 – 578, 05 1998. Cited in pages 4.

ARDUINI, C. *et al.* Active magnetic damping attitude control for gravity gradient stabilized spacecraft. *Journal of Guidance, Control, and Dynamics*, v. 20, n. 1, p. 117–122, 1997. Cited 3 time in pages 3, 21, and 22.

AVANZINI, G. *et al.* Attitude control of low earth orbit satellites by reaction wheels and magnetic torquers. *Acta Astronautica*, v. 160, p. 625–634, 2019. ISSN 0094-5765. Disponível em: <https://www.sciencedirect.com/science/article/pii/S009457651831974X>. Cited 2 time in pages 22 and 23.

AVELINO, Y. C. F. *et al.* Analysis of the influence of gravity-gradient torque on power generation in the cubesat standard. In: *75th International Astronautical Congress*. [S.l.: s.n.], 2024. Cited 14 time in pages v, vi, viii, 4, 25, 72, 73, 74, 95, 96, 97, 98, 99, and 105.

AVELINO, Y. C. F. *et al.* The impact of gravity-gradient stabilization on adcs efficiency and design optimization in cubesats. To appear in the 2025 IEEE Aerospace Conference. 2025. Cited in pages 105.

BECK, J. *Relative equilibria of a rigid satellite in a central gravitational field*. Tese (Doutorado), 11 1997. Cited in pages 2.

BORGES, R. A. *et al.* Perception data system for satellite monitoring of strategic assets. In: *Proceedings of the 75th International Astronautical Congress*. Milan, Italy: [s.n.], 2024. Cited in pages 105.

BORGES, R. A. *et al.* The alfacrux cubesat mission description and early results. *Applied Sciences*, v. 12, n. 19, 2022. ISSN 2076-3417. Disponível em: <https://www.mdpi.com/2076-3417/12/19/9764>. Cited in pages 105.

BOWDEN, M. Gravity gradient stabilized solar power satellite. In: *Applications of Space Developments*. [S.l.]: Pergamon, 1981. p. 313–336. Cited in pages 4.

CAPPELLETTI, C. *et al. CubeSat Handbook: From Mission Design to Operations*. [S.l.]: Elsevier Science, 2020. ISBN 9780128178843. Cited 3 time in pages 3, 4, and 24.

CAPPELLETTI, C. *et al.* Unicubesat: A test for a gravity-gradient solar array boom. *62nd International Astronautical Congress 2011, IAC 2011*, v. 5, p. 4097–4102, 01 2011. Cited in pages 2.

CHAURAIS, J. R. *et al.* Attitude control of an underactuated satellite using two reaction wheels. *Journal of Guidance, Control, and Dynamics*, v. 38, n. 10, p. 2010–2018, 2015. Cited 2 time in pages 23 and 47.

DANCHIK, R. J. An overview of transit development. *JOHNS HOPKINS APL TECHNICAL DIGEST*, v. 19, n. 1, 1998. Cited in pages 2.

DESOUKY, M. A. A. *et al.* A recursive approach for magnetic field estimation in spacecraft magnetic attitude control. *Aerospace*, v. 9, n. 12, 2022. ISSN 2226-4310. Disponível em: <https://www.mdpi.com/2226-4310/9/12/833>. Cited in pages 2.

EUROPEAN COOPERATION FOR SPACE STANDARDIZATION. *ECSS-E-HB-60-10A - Space Engineering: Control Performance Guidelines*. [S.l.], 2010. Cited 2 time in pages 51 and 56.

EUROPEAN COOPERATION FOR SPACE STANDARDIZATION. *ECSS-S-ST-00-01C Rev. 1 - Glossary of terms*. [S.l.], 2023. Cited in pages 68.

FINLEY, C. J. *NASA Space Science Data Coordinated Archive*. 2025. Disponível em: <https://nssdc.gsfc.nasa.gov/nmc/spacecraft/display.action?id=1965-089A>. Cited in pages 2.

FISCHELL, R. *et al.* A system for passive gravity-gradient stabilization of earth satellites. In: *Guidance and Control Conference*. [s.n.], 1964. Disponível em: <https://arc.aiaa.org/doi/abs/10.2514/6.1963-326>. Cited 3 time in pages 2, 4, and 24.

FRIK, M. A. Attitude stability of satellites subjected to gravity gradient and aerodynamic torques. *AIAA Journal*, v. 8, n. 10, p. 1780–1785, 1970. Disponível em: <https://doi.org/10.2514/3.5990>. Cited in pages 2.

GREY, J. P. *et al.* Analytic model for low earth orbit satellite solar power. *IEEE Transactions on Aerospace and Electronic Systems*, v. 56, n. 5, p. 3349–3359, 2020. Cited in pages 4.

HOGAN, E. A. *et al.* Three-axis attitude control using redundant reaction wheels with continuous momentum dumping. *Journal of Guidance, Control, and Dynamics*, v. 38, n. 10, p. 1865–1871, 2015. Cited 2 time in pages 22 and 23.

HORRI, N. M. *et al.* Practical implementation of attitude-control algorithms for an underactuated satellite. *Journal of Guidance, Control, and Dynamics*, v. 35, n. 1, p. 40–45, 2012. Cited 2 time in pages 23 and 47.

HUGHES, P. C. *Spacecraft Attitude Dynamics*. [S.l.]: Doves Publications, 2004. Cited 18 time in pages iv, 1, 8, 9, 10, 13, 19, 26, 29, 30, 31, 32, 33, 34, 35, 37, 38, and 39.

JIN, J. *et al.* Fault tolerant control for satellites with four reaction wheels. *Control Engineering Practice*, v. 16, n. 10, p. 1250–1258, 2008. ISSN 0967-0661. Disponível em: <https://www.sciencedirect.com/science/article/pii/S0967066108000233>. Cited in pages 23.

JOHNSTONE, A. *CubeSat Design Specification - Rev.4.1*. [S.l.], 2022. Cited 7 time in pages vii, 3, 41, 44, 70, 100, and 101.

KAZMI, S. C. N. *AGI Training and Certification - Small Satellite Series - Solar and Power Design*. 2024. (accessed 24.08.24). Disponível em: <https://register.agi.com/training/on-demand/small-sat/>. Cited in pages 73.

KRISHNAN, H. *et al.* Attitude stabilization of a rigid spacecraft using two momentum wheel actuators. *Journal of Guidance, Control, and Dynamics*, v. 18, n. 2, p. 256–263, 1995. Cited in pages 23.

LARSON, J. R. W. W. J. *Space Mission Analysis and Design*. [S.l.]: Springer Dordrecht, 1999. ISBN 978-0-7923-5901-2. Cited in pages 24.

LEE, D. *et al.* Geometric mechanics based nonlinear model predictive spacecraft attitude control with reaction wheels. *Journal of Guidance, Control, and Dynamics*, v. 40, p. 1–11, 12 2016. Cited in pages 23.

LIKINS, P. W. *et al.* Uniqueness of equilibrium attitudes for earth-pointing satellites. *Journal of the Astronautical Sciences*, v. 13, p. 87–88, 1966. Cited 2 time in pages 2 and 32.

LäTT, S. *et al.* Estcube-1 nanosatellite for electric solar wind sail in-orbit technology demonstration. *Proceedings of the Estonian Academy of Sciences*, 05 2014. Cited in pages 2.

MARKLEY, F. L. *et al. Fundamentals of Spacecraft Attitude Determination and Control*. [S.l.]: Microcosm Press and Springer, 2014. Cited 24 time in pages iv, 1, 2, 8, 9, 10, 11, 12, 13, 14, 15, 17, 18, 19, 20, 21, 22, 23, 26, 31, 38, 39, 47, and 51.

MASLOVA, A. *et al.* Modeling of the aerodynamic moment acting upon a satellite. *Cosmic Research*, v. 48, p. 362–370, 08 2010. Cited in pages 2.

MEIROVITCH, L. *et al.* On the effect of aerodynamic and gravitational torques on the attitude stability of satellites. *AIAA Journal*, v. 4, n. 12, p. 2196–2202, 1966. Disponível em: <https://doi.org/10.2514/3.3876>. Cited in pages 2.

MIYAMOTO, K. *et al.* Attitude dynamics of satellites with variable shape mechanisms using atmospheric drag torque and gravity gradient torque. *Acta Astronautica*, v. 202, p. 625–636, 2023. ISSN 0094-5765. Disponível em: <https://www.sciencedirect.com/science/article/pii/S009457652200621X>. Cited 4 time in pages 2, 3, 46, and 47.

MODI, V. J. *et al.* Librations of gravity-oriented satellites in elliptic orbits through atmosphere. *AIAA Journal*, v. 9, n. 11, p. 2208–2216, 1971. Disponível em: <https://doi.org/10.2514/3.50027>. Cited in pages 2.

NISE, N. S. *Control Systems Engineering*. [S.l.]: Wiley, 2015. Cited 2 time in pages 47 and 51.

NOHMI, M. Development of space tethered autonomous robotic satellite. In: *2007 3rd International Conference on Recent Advances in Space Technologies*. [S.l.: s.n.], 2007. p. 462–467. Cited in pages 2.

NUMPY DEVELOPERS. *NumPy documentation*. [S.l.], 2024. Disponível em: <https://numpy.org/doc/stable/index.html>. Cited in pages 44.

OVCHINNIKOV, M. Y. *et al.* A survey on active magnetic attitude control algorithms for small satellites. *Progress in Aerospace Sciences*, v. 109, p. 100546, 2019. ISSN 0376-0421. Disponível em: <https://www.sciencedirect.com/science/article/pii/S0376042119300569>. Cited in pages 22.

OVCHINNIKOV, M. Y. *et al.* B-dot algorithm steady-state motion performance. *Acta Astronautica*, v. 146, p. 66–72, 2018. ISSN 0094-5765. Disponível em: <https://www.sciencedirect.com/science/article/pii/S0094576517317332>. Cited in pages 22.

PYTHON SOFTWARE FOUNDATION. *pyIGRF 0.3.3: IGRF-13 Model by Python*. [S.l.], 2024. Disponível em: <https://pypi.org/project/pyIGRF/>. Cited in pages 47.

RIANO-RIOS, C. *et al.* Aerodynamic and gravity gradient based attitude control for cubesats in the presence of environmental and spacecraft uncertainties. *Acta Astronautica*, v. 180, p. 439–450, 2021. ISSN 0094-5765. Disponível em: <https://www.sciencedirect.com/science/article/pii/S0094576520307724>. Cited in pages 2.

SáNCHEZ-SANJUáN, S. *et al.* Comparison of the incident solar energy and battery storage in a 3u cubesat satellite for different orientation scenarios. *Journal of Aerospace Technology and Management*, v. 8, p. 91–102, 03 2016. Cited 3 time in pages 4, 24, and 25.

THE SCIPY COMMUNITY. *SciPy documentation*. [S.l.], 2024. Disponível em: <https://docs.scipy.org/doc/scipy/index.html>. Cited 2 time in pages 46 and 53.

VADALI, S. R. *et al.* Space station attitude control and momentum management - a nonlinearlook. *Journal of Guidance, Control, and Dynamics*, v. 15, n. 3, p. 577–586, 1992. Disponível em: <https://doi.org/10.2514/3.20878>. Cited in pages 2.

WANG, B. *et al.* Fine attitude control by reaction wheels using variable-structure controller. *Acta Astronautica*, v. 52, n. 8, p. 613–618, 2003. ISSN 0094-5765. Disponível em: <https://www.sciencedirect.com/science/article/pii/S0094576502001339>. Cited in pages 23.

WEINBERG, S. *Gravitation and Cosmology: Principles and Applications of the General Theory of Relativity*. Chichester: Wiley, 1972. Cited in pages 14.

WERTZ, J. R. *Spacecraft Attitude Determination and Control*. [S.l.]: Kluwer Academic Publishers,, 1973. Cited 7 time in pages iv, 1, 8, 9, 10, 15, and 20.

WIśNIEWSKI, R. *et al.* Fully magnetic attitude control for spacecraft subject to gravity gradient. *Automatica*, v. 35, n. 7, p. 1201–1214, 1999. ISSN 0005-1098. Cited 2 time in pages 3 and 22.

YOST, B. *et al. State-of-the-Art Small Spacecraft Technology*. Ames Research Center, 2023. Disponível em: <https://www.nasa.gov/smallsat-institute/sst-soa/>. Cited 3 time in pages 3, 4, and 24.

ZAHRAN, M. *et al.* Assessment of earth remote sensing microsatellite power subsystem capability during detumbling and nominal modes. *Journal of Power Electronics*, v. 6, p. 18–28, 01 2006. Cited in pages 4.

ZHANG, X. *et al.* Optimal path planning-based finite-time control for agile cubesat attitude maneuver. *IEEE Access*, v. 7, p. 102186–102198, 2019. Cited in pages 22.